核理研研究報告　第34巻　2001年

ISSN 0385-2105

TOHOKU

RESEARCH REPORT OF LABORATORY OF NUCLEAR SCIENCE

Vol.34 2001

TOHOKU UNIVERSITY

Editors

TAMAE, Tadaaki

OHTSUKI, Tsutomu

HAMA, Hiroyuki

Laboratory of Nuclear Science

Tohoku University

1-2-1 Mikamine, Taihaku, Sendai 982-0826

Japan

Pone: +81, 22-743-3400

Fax: +81, 22-743-3401

Web site: http://www.lns.tohoku.ac.jp/

982-0826 仙台市太白区三神峯1-2-1

東北大学大学院理学研究科

附属原子核理学研究施設

電話 022-743-3400

Fax 022-743-3401

Preface

This issue of Research Report of Laboratory of Nuclear Science reports research activities of the LNS performed in the 2000 academic/fiscal year (April 2000 - March 2001). Major research activities are based on the electron accelerator complex consisting of the 300-MeV LINAC and the 1.2-GeV STB ring installed in 1997. The accelerators have altogether provided a beam time of about 2400 hours for various experiments through the year.

For a particular importance of this year, we have observed much progress on 1.2 GeV electron beam operation of the STB ring, although the available beam time was not enough. The beam intensity of 1.2 GeV circulating electrons has reached to 20 mA after a major difficulty was removed, and there is still more room for improvement to get much intense beam. Furthermore, the STB Tagger, which provides tagged GeV photons, has been installed in the ring and has worked well for experiments with GeV photons; new data of (γ, η) reactions on nuclei have been obtained and are now being analyzed.

We hope that the Report will serve as a quick overview of the present LNS activities over a variety of nuclear science research fields.

Jirohta KASAGI
Director

Research Report of Laboratory of Nuclear Science
Volume 34, 2001

Contents

Ⅱ. Radiochemistry

Ⅲ. Accelerator, Synchrotron Radiation, and Instrumentation

Ⅳ. 2000 Status Report on the Accelerator

核理研研究報告　第34巻　目　次

Ⅰ．原子核物理

Ⅱ．放射化学

I . Nuclear Physics

Excitation of Double Giant Resonance in ^{40}Ca by (γ , n) reaction

Y. Terasaki[1], K. Hirose[2], H. Kanda[2], K. Maeda[2], T. Terasawa[1] and M. Tsuruta[1]

[1]*Laboratory of Nuclear Science, Tohoku University, Sendai 982-0826*
[2]*Department of Physics, Graduate School of Science, Tohoku University, Sendai 980-8578*

Recently excitation of the Double Giant Resonance (DGR) with Coulomb excitation by heavy ions and double charge exchange reactions such as (π^+, π^-) reaction were reported frequently. For example, a DGR which is composed of a GDR on a GDR in ^{136}Xe was excited by ^{136}Xe + Pb at SIS at GSI, Darmstadt [1]. Its peak energy was about twice of that of a GDR as expected but the cross section was double of the expectation. The DGR is excited from the ground state by mainly 2-step excitations.
The probability for n-step excitation is

$$P_n = \frac{1}{n!} F^n \exp(-F)$$

where F is the probability for 1 phonon excitation $\sim(\alpha Z)^2$
In the case of coulomb excitation by heavy ion with $Z=80$,

$$P_2/P_1 \sim 0.3$$

but for real photon reaction ($Z=1$)

$$P_2/P_1 \sim 10^{-4}$$

Then 2-step excitation is almost impossible for real photons.

However we know that the MEC is important for photo-nuclear reactions. Since the MEC is a two-body operator, we can excite a two-phonon state at once.

Suzuki of Fukui University calculated [2] the excitation probabilities of DGR by the MEC. For ^{40}Ca, a DGR composed of a GDR (E = 19.9 MeV) and an IVGQR (E = 30 MeV) is expected at E_γ = 50 MeV. He calculated the ratio of the total photon absorption cross section for this DGR and for the one-phonon GDR. He got the ratio of about 20% for the DGR. We can see similar fractions of cross sections at $E_\gamma \sim 50$ MeV in a figure given by Ahrens *et al.* [3]. We thought this strength is measurable.

We measured (γ ,n) reaction instead of a total photon absorption cross section. The electron energy was set at 150 MeV. The energies of photons were $30 < E_\gamma < 120$ MeV, and energy resolution was 1.5 MeV. A natural calcium of 7 cm long was used as the target. We used 12 neutron detectors, each has 30 cm long cylinder with 10 cm radius, filled with NE213 liquid scintillators and placed around the target. Flight length of neutron from the target to the neutron detector was 2 m.

The beam time given were 10 shifts .

Neutrons were selected by both PSD and charge comparison method. We chose events of ground state transition correspond to (γ , n_0), and transition to the giant dipole resonance of ^{39}Ca. The neutron spectra of the ground state transition, as the function of γ -ray energies, were shown in Fig.1.

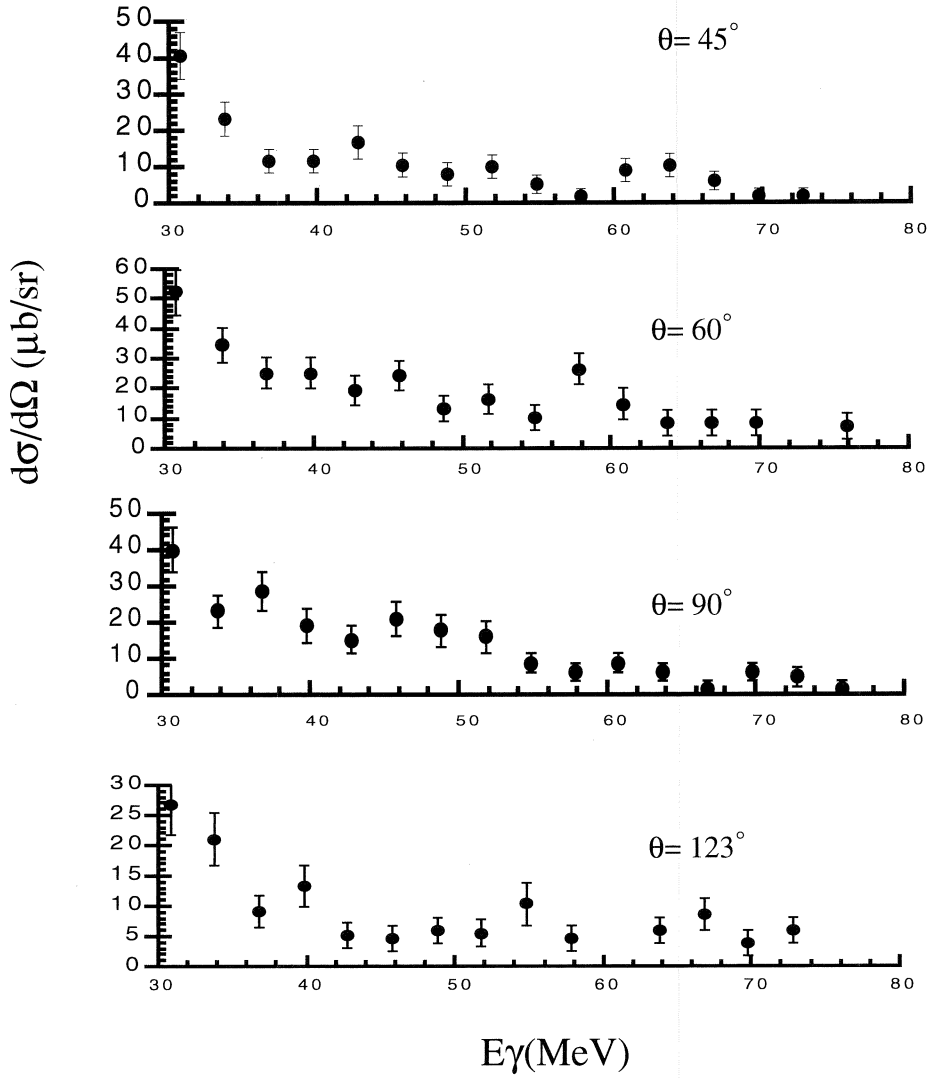

Fig.1. (γ, n) cross sections for $-5 < E_m < 5$ MeV.

There is another mechanism that a DGR can be excited. That is ground state correlation. ^{40}Ca has a large probability for ground state correlation. Thus the ground state of ^{40}Ca is a mixture of 2p-2h and 4p-4h states adding to 0p-0h state. Then one can excite the DGR, which has mainly 2p-2h, by changing the coupling of two one p-h pair. One can excite the DGR composed of an ISGQR (E = 17.9 MeV) and an IVGDR (E = 19.9 MeV) through the ground state correlation, on the other hand the two one-phonon states have different iso-spins, and can not be excited by the MEC. A peak at E_γ = 35 MeV in ^{40}Ca(γ, n_0) cross section which was found by LUND [4] might be an example.

There are some peaks in the (γ, n_0) cross sections in Fig.1, however because they show no correlation among scattering angles, we must say that these peaks are statistical fluctuations.

When the DGR is composed of a GDR and an IVGQR, we expect the decay would go by way of the GDR or the IVGQR in neighboring nucleus. We show the (γ,n) cross sections for 15 MeV $< E_m <$ 25 MeV, in Fig.2. The width of the DGR will be a sum of that of the GDR and the IVGQR, about 18 MeV. The

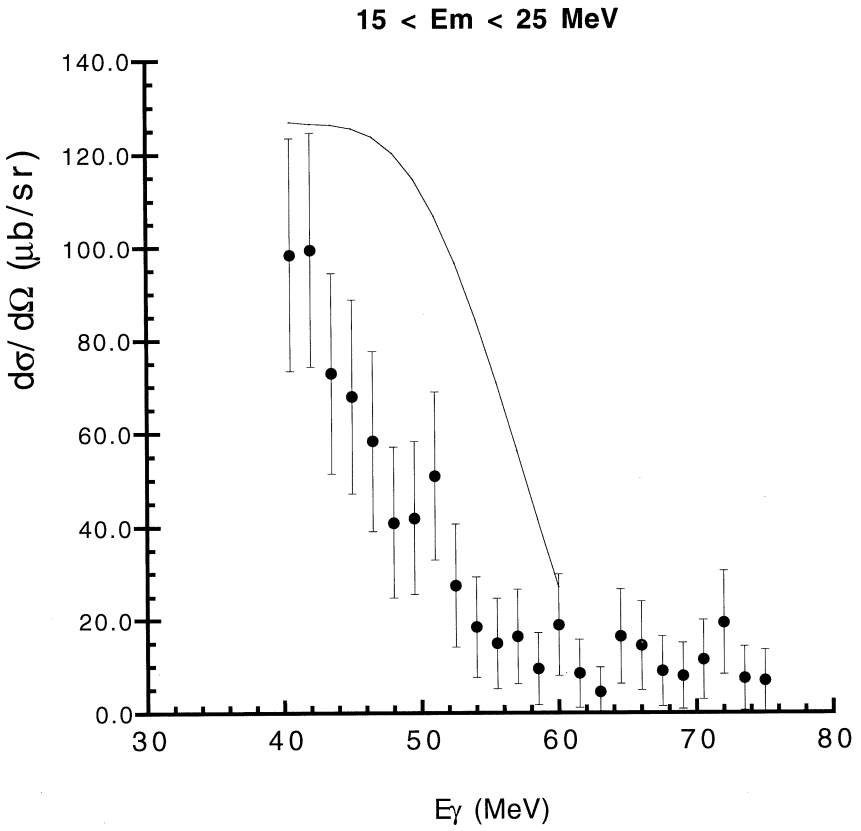

Fig.2. (γ , n) cross section for $15 < E_m < 25$ MeV. A curve is an expectation [2] that a DGR is excited at $E_\gamma =$ 50 MeV with width of 18 MeV and strength of 23.4% of one phonon GDR.

(γ ,n) spectrum in Fig.2. shows a tail of the one-phonon giant dipole resonance. From the total photon absorption cross section the area of the tail at the interval of 40 MeV $< E_\gamma <$ 60 MeV is about 20% of the total GDR. We assume the tail of the GDR as a straight line going through the experimental value at E_γ = 40 MeV down to zero at E_γ = 60 MeV. According to Suzuki, a DGR will be excited by the MEC at E_γ = 50 MeV with a strength of 23.4% of GDR. An estimate that 23.4% of GDR centered at $E_\gamma =$ 50MeV and on the straight background is also shown. We can say that 23.4% is clearly over estimate.

The DGR excited by the MEC is a state that a proton hole-neutron particle coupled as 2^+ state multiplied by a neutron hole-proton particle coupled as 1^- state. We expected a maximum overlap of the 1^- state with the GDR of ^{39}Ca. However, we cannot observe a peak of the DGR at corresponding position, although statistics was poor. One reason might be the assumption of maximum overlap between 1^- states having a neutron hole-proton particle and a proton hole-proton particle is poor. To avoid these difficulties, we should measure (γ , pn) reaction or total photon absorption cross sections.

References

[1] R. Schmidt *et al.* : Phys. Rev. Lett. **70** (1993) 1767.

[2] T. Suzuki : *private communication*.

[3] J. Ahrens *et al.* : Nucl. Phys. **A251** (1975) 479.

[4] D. Sims *et al.* : Phys. Rev. **C55** (1997) 1288.

Study of (e,e′ α) Reaction on ^{9}Be

Y. Asano[1], T. Tamae[1], R. Kimura[2], O. Konno[1]*, K. Hirota[1], K. Maeda[2], H. Miyase[2], I. Nishikawa, T. Terasawa[1], H. Tsubota[2] and H. Yamazaki[1]

[1]*Laboratory of Nuclear Science, Tohoku University, Mikamine, Taihaku-ku,Sendai 982-0826*
[2]*Physics Department, Graduate School of Science, Tohoku University, Aramaki, Aoba-ku,Sendai 980-0845*

The (e,e′ α) cross section has been measured at energy transfers from 10.0 to 28.4 MeV and a momentum transfer of 99 MeV/c, using a 197 MeV continuous electron beam. The cross section rapidly increases with decreasing energy at angles smaller than 25°, while it appears flat at larger angles. The forward-peaked angular distribution was observed below 18 MeV, and the forward peak shrinks at higher energies. An amount of α particles from decay of ^{5}He is estimated.

§ 1. Introduction

There has been a growing interest in the study of neutron-halo and neutron-skin structure. Very recently, the RI Beam Factory project has started at RIKEN to explore this subject. The nucleus ^{11}Be is known as a neutron-halo nucleus [1], and there are several microscopic and macroscopic attempts at describing Be isotopes in a unified framework of two α particles and extra neutrons. The ^{9}Be nucleus is the simplest isotope, which has one extra neutron, and is known to have a typical $\alpha+\alpha+$n cluster structure. Therefore the nucleus has already been investigated in various models.

The photo-disintegration of ^{9}Be is categorized in three separate mechanisms: (1) threshold to 5 MeV, where sharp resonances correspond to direct excitations of the unpaired neutron; (2) 5-18 MeV, where weak coupling of the unbound neutron to ^{8}Be dominates; (3) above 18 MeV, where a core is excited. The photo-nuclear reaction has been investigated in the (γ, n) [2-5], (γ, p) [6], (γ, d) [6], (γ, t) [6] and (γ, ^{3}He) [6] channels. However, no (γ, α) cross section has been measured, presumably because the decayed α particles of ^{5}He that partly overlap on the spectrum make the analysis difficult. The threshold of the (γ, α) reaction is 2.53 MeV; this is the only charged-particle emission channel below 16 MeV. The cross section is expected to be large enough for measurement.

The residual nucleus ^{5}He of the ^{9}Be (e,e′ α) reaction is same as the ^{6}Li (e,e′p) reaction, which we investigated several years ago [7]. However, the missing energy spectra of both reactions may be different from each other, because they reflect their reaction mechanisms. We measured ^{9}Be (e,e′ α) cross section at eleven angles at transferred energies between 10.0 and 28.4 MeV as a test experiment.

§ 2. Experimental procedure

The experiment was performed using a 197 MeV continuous electron beam from a stretcher-

*Department of Electrical Engineering, Ichinoseki National College of Technology, Hagiso, Ichinoseki 021-8511

booster ring (STB). Electrons scattered with a 1.8 mg/cm^2 thick natural beryllium foil were analyzed with a magnetic spectrometer (LDM) at 30°. Missing energies were set at two energies: phase 1 (10.0 ~ 21.0 MeV), phase 2 (17.6 ~ 28.4 MeV). Corresponding momentum transfers are 98.60 MeV/c for phase 1 and 99.10 MeV/c for phase 2. Ejected α particles were measured with eleven SSD counter telescopes composed of two surface-barrier type SSD's (one 50 μm SSD + one 1 mm SSD at eight angles, and two 1 mm SSD's at three angles), out-of the scattering plane ($\phi_\alpha = 90°$). The solid angle of the telescopes is 4.8 msr. Due to insufficient machine time, no measurement between 90° and 180° was made in this run.

§ 3. Results and Discussion

Figure 1 shows missing energy spectra at the momentum transfer direction; a peak at 2.5 MeV corresponds to α particle emission leaving the residual nucleus at the ground state of ^{5}He. A tail toward higher missing energies is observed in the spectrum for the lower energy transfer region; more structures can be seen in the spectrum for the higher energy transfer region. Considering a resolution of the experiment, events below $E_m = 7$ MeV were treated as α_0 events.

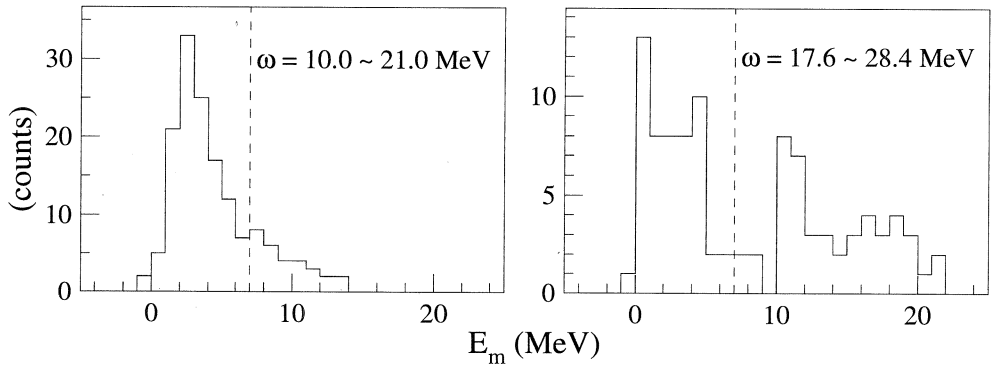

Fig.1. Missing energy spectra at 0°. A peak at 2.5 MeV corresponds to (e,e′ α_0) reaction.

A transferred energy dependence of the differential (e,e′ α_0) cross sections is shown in Fig.2. At forward angles, the cross section becomes larger as the energy decreases; while no such rise can be seen at backward angles. angular dependence of the differential cross section is shown in Fig.3. At low energies, a strong forward peaking is observed; data at backward angles are lacking because energies of the α particles are lower than the threshold energy of the detectors there.

In the (e,e′ α) ^{5}He reaction, the residual nucleus ^{5}He decays into n + α; this α particles partly overlap on the α particles of the (e,e′ α) ^{5}He reaction. Simulated missing energy spectra of both α particles are demonstrated in Fig.4. In this calculation several assumptions were made:

(1) The angular distribution of the ^{9}Be (e,e′ α) ^{5}He reaction has a forward-backward symmetry in the center of mass system; Legendre parameters has been obtained by fitting the measured angular

distributions with even-order Legendre functions up to $l = 4$.

(2) The angular distribution of the α particle due to $\alpha+\alpha+$n decay of ^{5}He is isotropic in the center of mass system.

The lowest peak in Fig.4 corresponds to α particles from the ^{9}Be (e,e′ α) ^{5}He reaction; the higher missing-energy part of two-peaked structure corresponds to decay products of ^{5}He. Alpha-particles emitted toward the detector direction make the lower peak, while those to the opposite direction do the higher peak. The structure changes slowly at other angles. The two-peaked structure shifts toward higher missing-energies as the transferred energy ω increases. The missing energy spectra folded in the regime of the measurements are shown in Fig.5, where the structure is smeared in resolution (1 MeV FWHM). A tail in higher energy part for $\omega = 10 \sim 21$ MeV in Fig.1 is reproduced in this

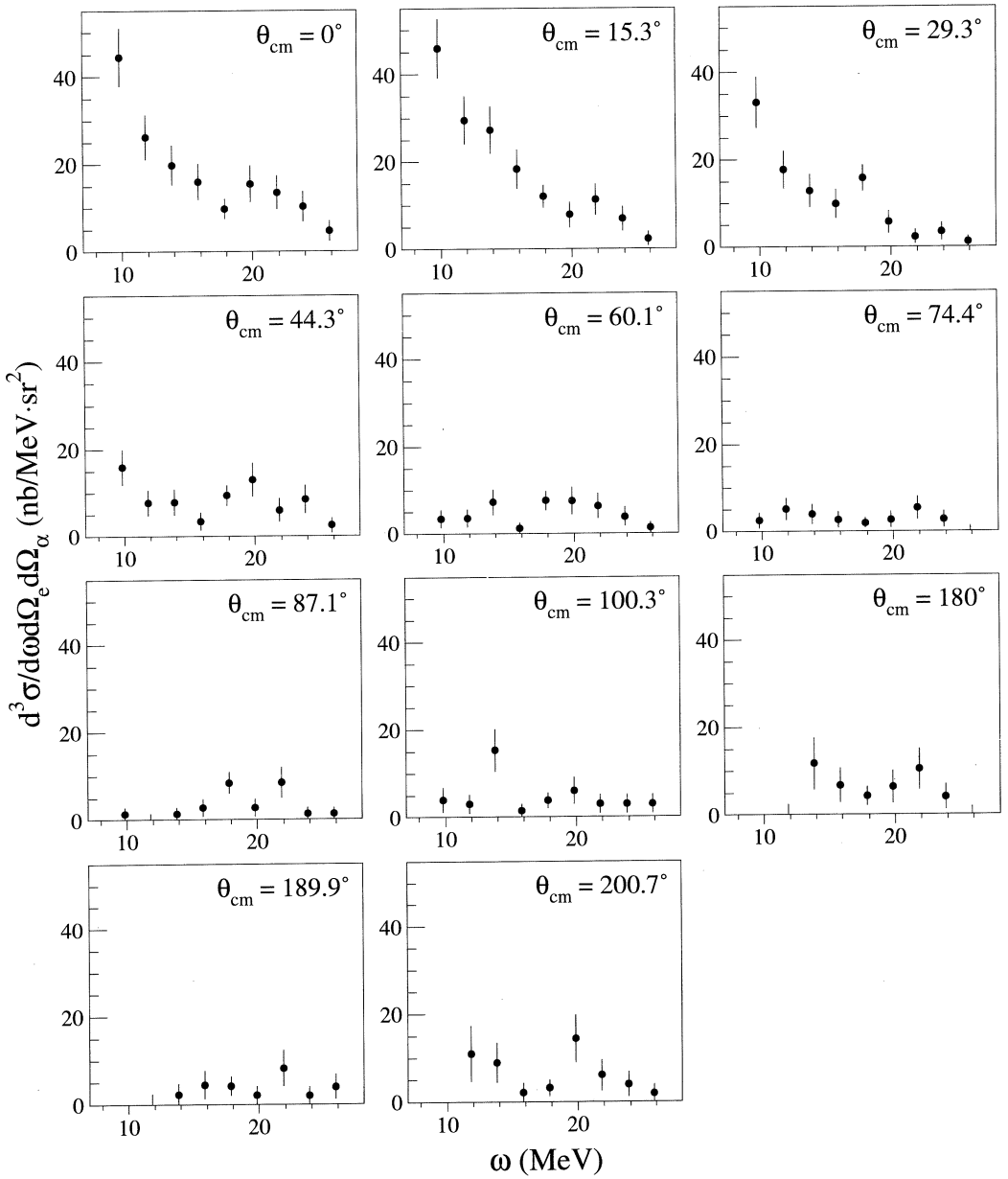

Fig.2. The ^{9}Be (e, e′ α_0) differential cross sections.

simulation. In case $\omega = 17.6 \sim 28.4$ MeV, the part $E_m > 10$ MeV cannot be reproduced in the simulation although the measured spectrum has large statistical errors. It may be a contribution of α particles from the ^{9}Be (e,e′n) ^{8}Be (16.6 MeV) $\rightarrow 2\ \alpha$.

We wish to thank the accelerator group and the computer group for their assistance during the measurements.

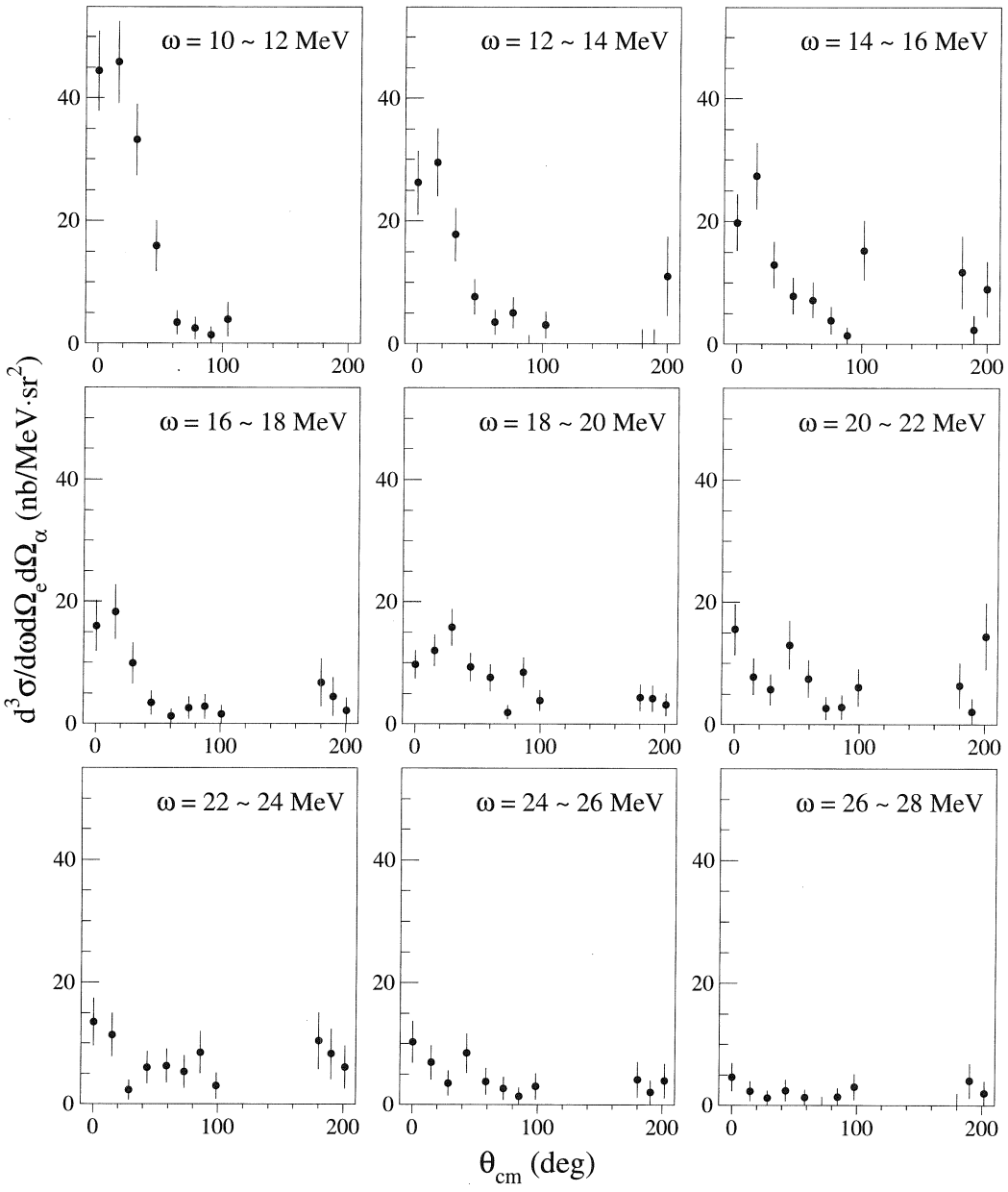

Fig.3. Angular distributions of the ^{9}Be (e, e′ α_0) reaction.

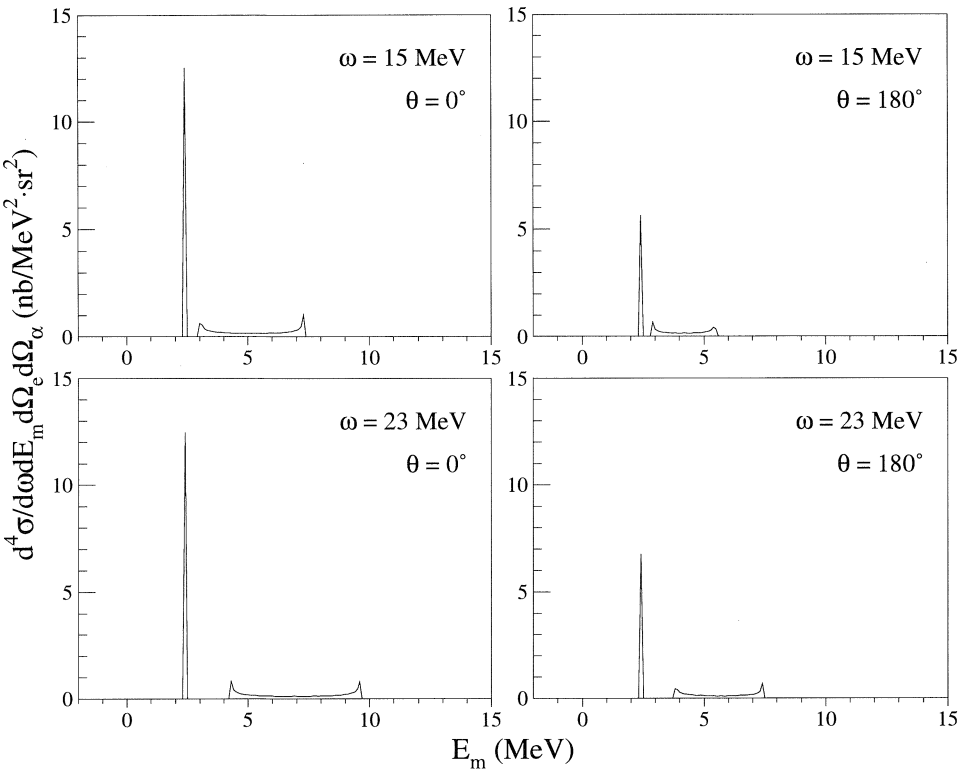

Fig.4. Simulated missing energy spectra of the ^{9}Be (e, e' α_0) reaction (a peak at E_m = 2.5 MeV) and the α emission from ^{5}He (two-peaked part at higher missing energies).

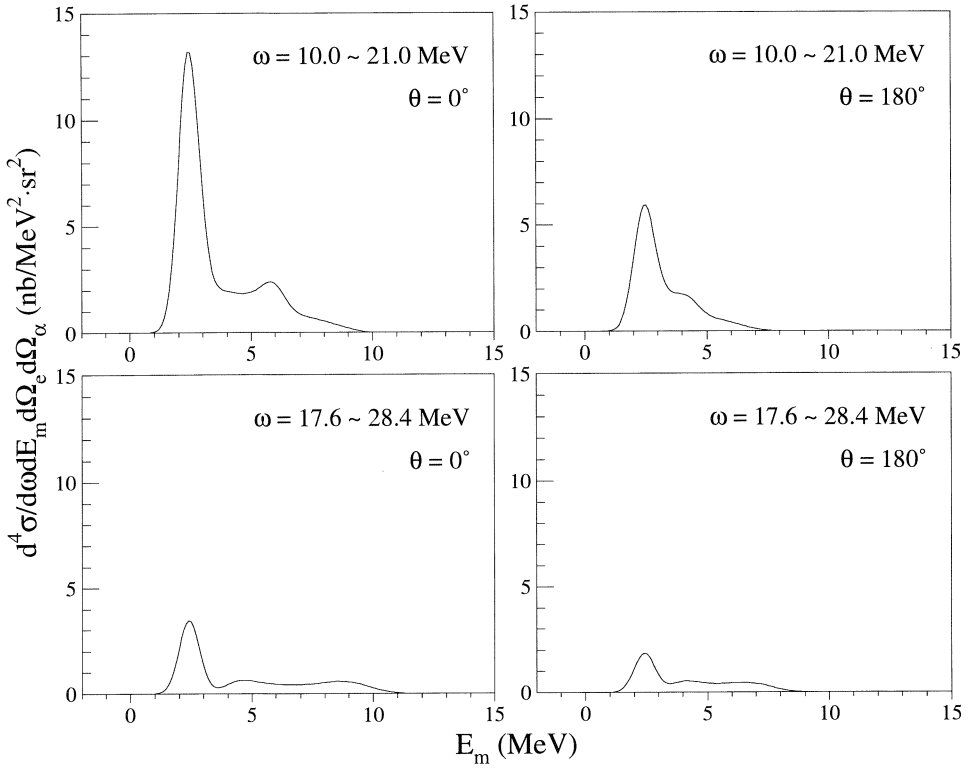

Fig.5. Simulated missing energy spectra folded in the regime of the measurements, which are smeared with a resolution of 1 MeV FWHM.

References

[1] Tanihata *et al.* : Phys. Rep. B **206** (1988) 592.

[2] R. J. Hughes, R. H. Sambell, E. G. Muirhead, and R. M. Spicer : Nucl. Phys. **A238** (1975) 189.

[3] U. Kneissl, G. Kuhl, K.-H. Leister, and A. Weller : Nucl. Phys. **A247** (1975) 91.

[4] A. Buchnea, R. G. Johnson, and K. G. McNeill : Can. J. Phys. **55** (1977) 364.

[5] H. Utsunomiya *et al.* : Phys. Rev. **C63** (2000) 018801.

[6] K. Shoda and T. Tanaka : Phys. Rev. **C59** (1999) 239.

[7] T. Hotta *et al.* : Nucl. Phys. **A645** (1999) 492.

Observation of S_{11} (1535) in Nuclei via (γ, η) with STB Tagger

T. Kinoshita[1], H. Yamazaki[1], K. Hirota[1]*, T. Katsuyama[1], A. Kato[1], K. Kino[1], T. Nakabayashi[1], T. Terasawa[1], J. Kasagi[1], T. Takahashi[2], H. Kanda[2], K. Maeda[2], H.Yoshida[3], Y.Tajima[3], Y. Itoh[3], H. Fujinoya[3], A. Iijima[3], T. Noma[3], Y. Aruga[3] H.Shimizu[3], T. Yorita[4] and O. Konno[5]

[1]*Laboratory of Nuclear Science, Tohoku University, Mikamine, Taihaku, Sendai 982-0826*
[2]*Department of Physics, Graduate School of Science, Tohoku University, Sendai 980-8578*
[3]*Department of Physics, Yamagata University, Yamagata 990-8560*
[4]*Research Center for Nuclear Physics, Osaka University, Ibaraki, Osaka 567-0047*
[5]*Ichinoseki National College of Technology, Ichinoseki, Iwate 021-8511*

Chiral symmetry and its spontaneous breaking are very important for understanding the properties of hadrons at low energies. Change of QCD vacuum at finite temperature and/or at finite density affects the nature of hadron. Then, investigating the nature of hadron under several environment, e.g., in nuclear medium, is best way to understand the properties of chiral symmetry and its spontaneous breaking. S_{11}(1535) resonance is one of the candidates of the chiral partner of the nucleon. Thus, it is very important to investigate the property of S_{11}(1535) in nuclear medium to explore the chiral property of the nucleon.

Since η mesons are produced mainly through the S_{11}(1535) resonance in H (γ, η) reaction for $E_\gamma <$ 1.1 GeV, the η photoproduction reaction is a nice tool to investigate the S_{11}(1535) resonance in nuclei. We performed the experiment on the C (γ, η) reaction at KEK-Tanashi and the result was published in ref. [1]; the data so far obtained suggest that the resonance width might be changed in nuclei. We have extended the (γ, η) measurements to obtain much better data not only with high statistics but also with various nuclei.

A new series of the experiments have been carried out by using tagged photon beams from STB tagger at the Laboratory of Nuclear Science at Tohoku University [2]. The energy range of the tagged photons which was used at this experiment was from 0.63 to 1.1 GeV.

The tagged photon beam bombarded the nuclear targets and produced η mesons. Two γ-decay of η meson was detected by a calorimeter system called SCISSORS (Sendai CsI Scintillator System On Radiation Search), which was newly constructed [3]. It consists of the 206 individual pure CsI crystal detectors. Bombarded were C, Al, Cu targets of 30, 10, 5 mm in thickness, respectively. The invariant mass for the two- γ event was calculated by using the photon energy and the angle between two γ rays. Figure 1 shows such a spectrum obtained in the present work. A prominent peak corresponding

*Present address: SPring-8, JASRI, Sayo-Gun, Hyogo 679-5198.

to the η meson is clearly seen at around 550 MeV/c^2, as well as a peak of π^0 meson, although they are superimposed on continuous background events which are mainly due to 4-photon events from $2\pi^0$. The mass resolution is 5% for η meson mass. The yield of detected η meson in each spectrum was deduced by subtracting background events in the η-mass region estimated with an exponential function fitted to the continuum.

Figure 2 shows the total cross section of the C (γ, η) reaction. Closed circles are data from the present experiment and open circles from the previous experiment. It is compared with the model calculation based on the Quantum Molecular Dynamics. Various medium effects, such as Fermi motion of the nucleon, Pauli blocking, η absorption in nuclei, nucleon-S_{11} collisions and so on, are incorporated in the calculations. These are preliminary data and a detailed analysis is underway. Then we cannot say much yet. However, the quality of data in the present experiment is much improved than our previous experiment, enough to understand the nature of $S_{11}(1535)$ resonance in nuclei.

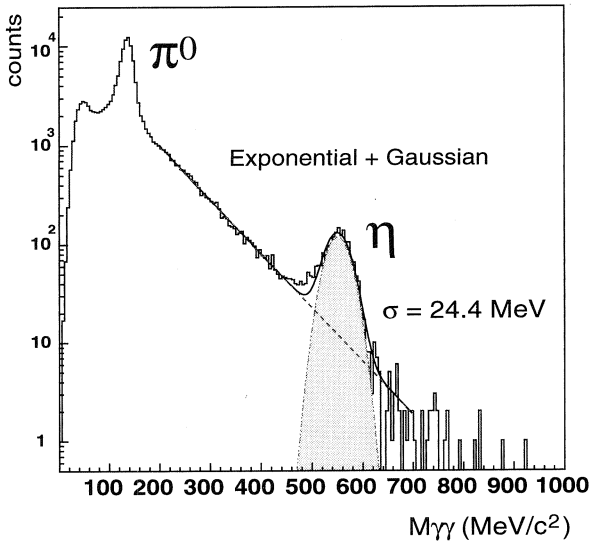

Fig.1. Invariant mass distribution for the two-γ events. A prominent peak corresponding to the η meson is clearly seen at around 550 MeV/c^2, as well as a peak of π^0 meson.

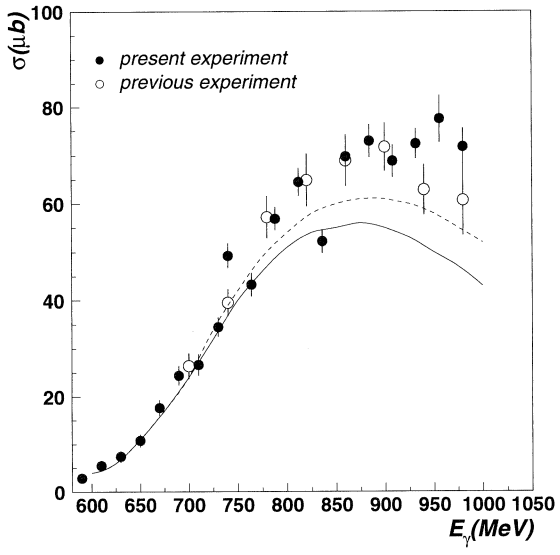

Fig.2. Total photo- η production cross section on C. Closed circles are data from the present experiment, open circles from the previous experiment. The results of the QMD calculations are also shown; the solid line corresponds to the resonance width of 154 MeV and the dashed line to 212 MeV. These are preliminary data and a detailed analysis is underway.

References

[1] T. Yorita *et al.* : Phys. Lett. B**476** (2000) 226.

[2] H. Yamazaki *et al.* : Research Report of LNS, Vol. 33 (2001) 30.

[3] K. Hirota *et al.* : Research Report of LNS, Vol. 33 (2000) 35.

Development of Parallel Plate Avalanche Counter for (e, e'f) Reaction

H. Matsui, T. Ohtsuki, A. Miyamoto, M. Tsuruta, Y. Terasaki and T. Terasawa

Laboratory of Nuclear Science, Tohoku University, Mikamine, Sendai 982-0826

A pair of parallel plate avalanche counter (PPAC) was made for the purpose of detecting fission fragments from (e, e'f) reaction. The performance of the PPAC was tested with use of both ^{252}Cf radio active source and ^{232}Th(e, f) experiment. We could clearly observe mass difference of fragments in the ^{232}Th(e, f) experiment.

§ 1. Introduction

Recently a strange phenomenon was observed in Mainz in an experiment of ^{235,238}U(e, e'f) at giant resonance [1]. The symmetric to asymmetric mass distribution of the fission fragments ($\Gamma s/\Gamma_A$) differs for the multipolarity of the excitation. It will be difficult to understand since a fission proceeds via a long time so that the information of the excitation can not be held after the fission. The shape of the mass distribution of the fission fragment is different for different nuclei. Fission of ^{235,238}U is most frequently studied, however the symmetric to asymmetric mass distribution of fission fragments of these nuclei is not well separated. On the other hand, ^{232}Th has more clear separation of symmetric to asymmetric fission fragments. We decided to make the ^{232}Th(e, e'f) experiments and to confirm the Mainz results.

We will use a set of PPAC (parallel-plate avalanche counter) for the detection of fission fragment. PPAC is a gas counter. A hydrocarbon gas (we use isobutane) of several torr is filled between a pair of electrodes and impressed several hundreds volt. A passing fragment ionizes the gas and generated electrons cause an electron avalanche. Characteristics of the PPAC is as follows:

1) Good time resolution (several of 10 ps～100 ps)
2) High count rates (several of 10^6 cps)
3) Can make as position sensitive
4) Not sensitive to gamma ray or light charged particles

This report describes the properties of PPAC's and gas handling system which we have made and results of ^{232}Th(e, e'f) test experiment which is performed at 2nd experimental hall of the Laboratory.

§ 2. PPAC

We have made two pairs of PPAC's, each pair consists of 2 anodes and 2 cathodes; each of them measures X and Y directions of a fragment. The two pairs measure two fragments of a fission and a mass difference is measured by a time of flight difference. The structure of a PPAC is shown in Fig.1. A PPAC consists of 50 anode wires and a cathode plate. The space of the wires is 2mm with an accuracy of

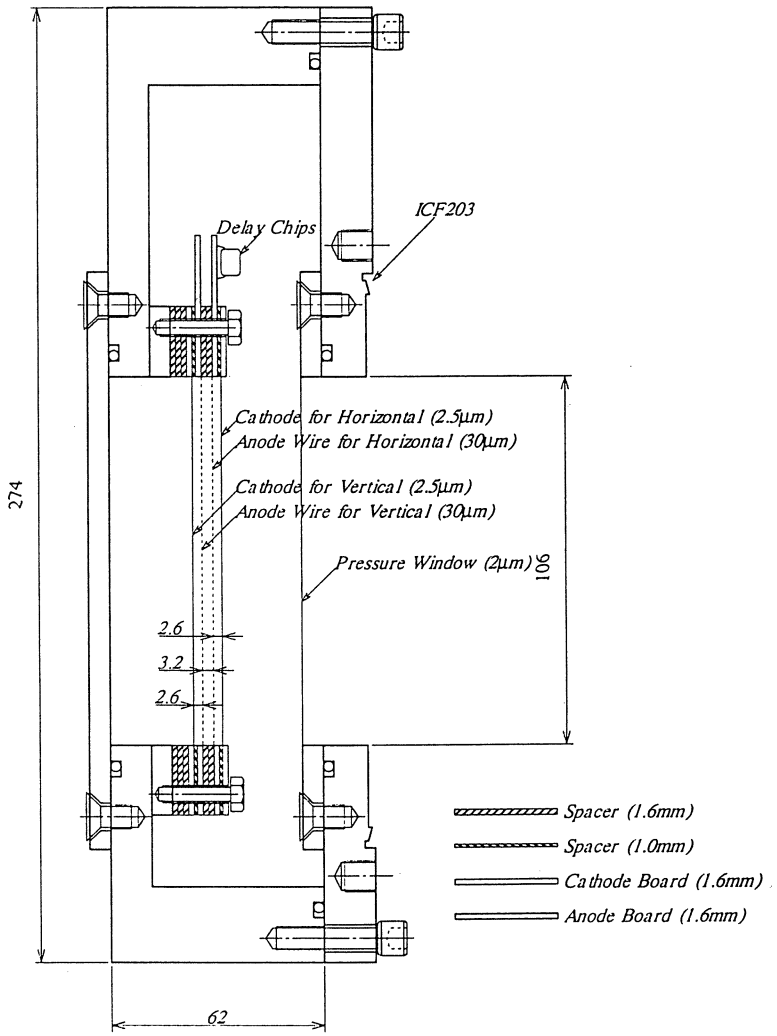

Fig.1. Sectioned drawing of a PPAC.

0.1 mm.

Each two adjacent wires are connected by a 3ns delay chip in order to find the wire that produces a signal. The cathode is a 2.5 μm thick Aluminized Mylar stretched on a 10.5 cm $\times$ 10.5 cm opening base of 2.6 mm thickness. Then, the space between anode and cathode is 2.6 mm. An isobutane gas of 3 Torr circulates the electrodes. The pressure is maintained by a gas handling system. We show the structure of the system schematically in Fig.2. Also shown is a vacuum chamber in which two PPAC's are set face to face. The center of the chamber is a fission target and a fright length of the fragment is 30 cm. A PPAC and high vacuum side is partitioned by a polyethylene film of 2 μm thickness.

§ 3. A test of the PPAC using a ^{252}Cf radioactive source

The fundamental performance of our self-made PPAC is examined by using a ^{252}Cf radioactive source. The experimental arrangement is shown in Fig.3. A half side of the vacuum chamber is used. First we evacuate both a PPAC and high vacuum part of the chamber. Then, isobutane gas of 2$\sim$5 Torr is supplied from the gas handling system. The fluctuation of the pressure was less than 0.1 Torr. Then, we impress the negative voltage to cathode. The signals of the PPAC are observed from both anode wire

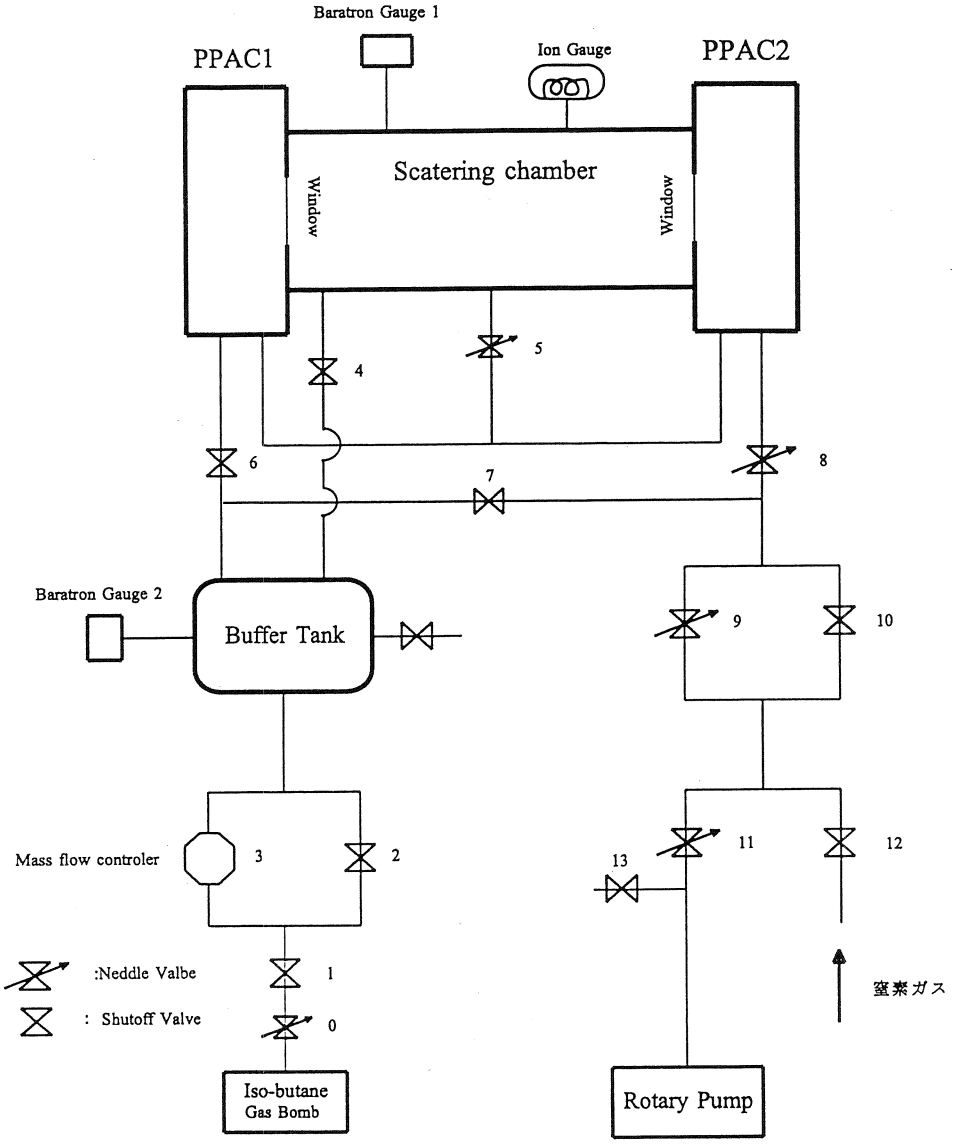

Fig.2. Gas handling system.

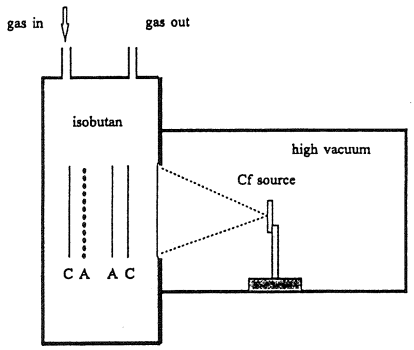

Fig.3. Set up for ^{252}Cf source test.

and cathode. If we increase the voltage, the signal starts to appear at about −360 volts. A signal after a fast timing amplifier and a PM amplifier (2000 amplification) connected to an anode wire is shown in Fig.4. A pulse height of −100 mV and a rise time of about 8ns are obtained. Next we try to get the spatial resolution of the PPAC. TDC spectrum of anode wire is shown in Fig.5. The spectrum shows 50

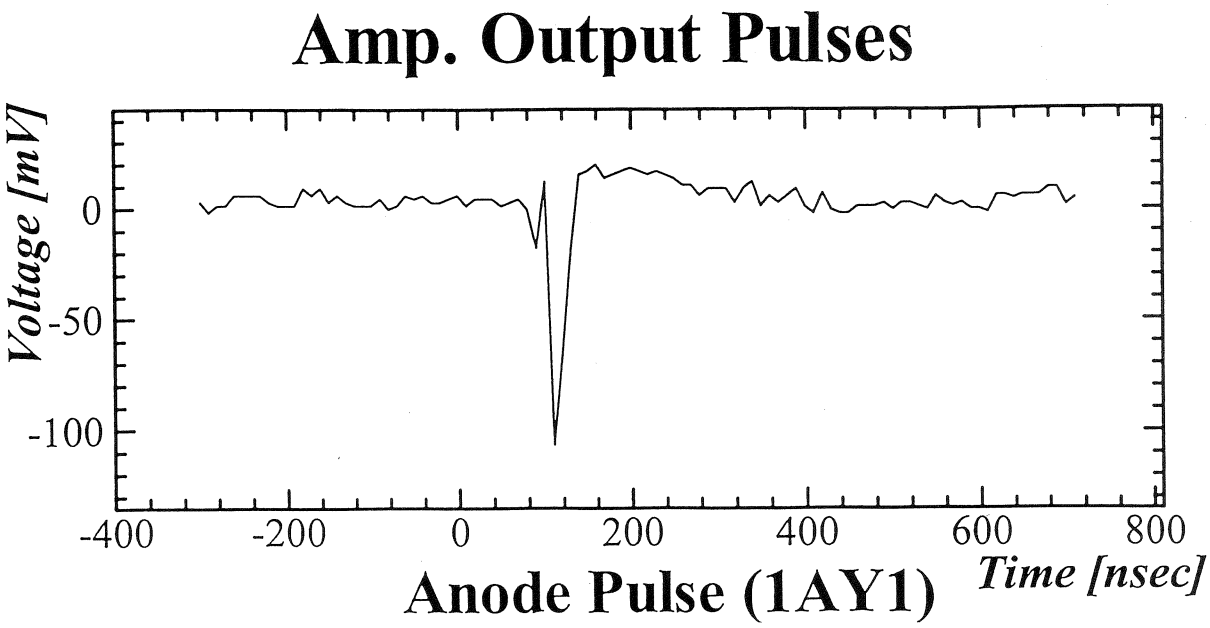

Fig.4. Output signal of PM amplifier. A rise time is 8 ns.

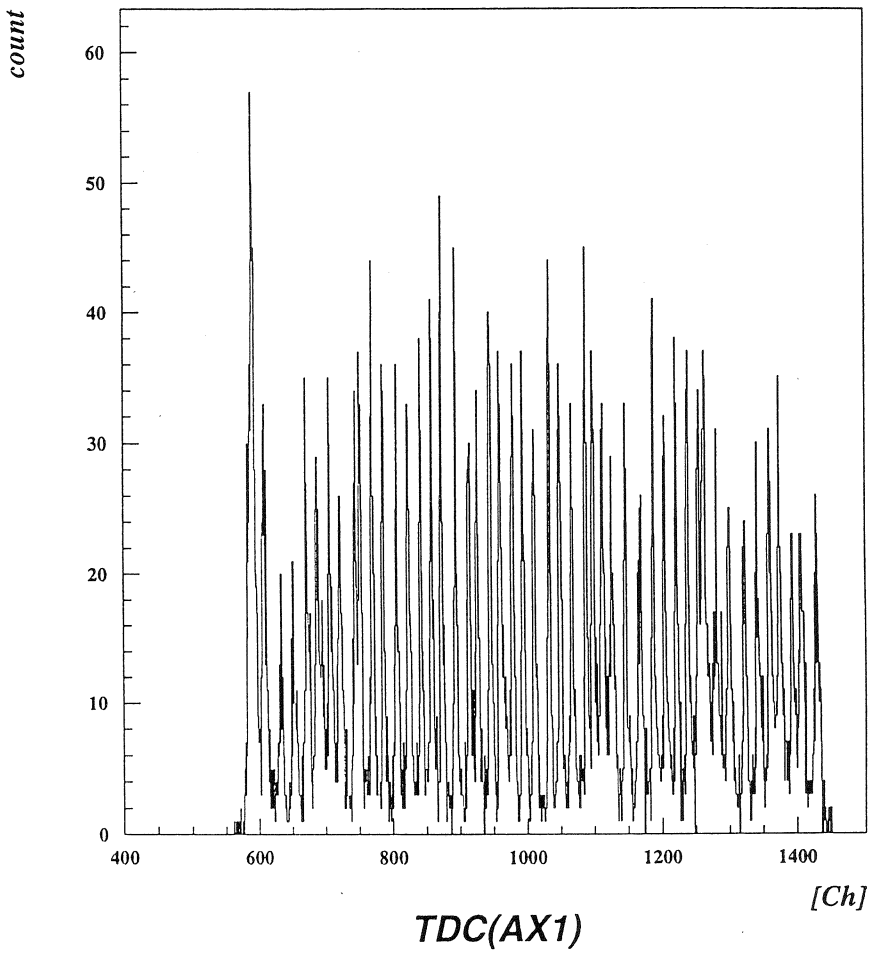

Fig.5. TDC spectrum between an anode and cathode.

structures corresponding to 50 wires. One can understand that the spatial resolution of the PPAC is satisfactory.

§ 4. ^{232}Th(e, f) experiment

In order to get an electrofission cross section for ^{232}Th we used an electron beam from the Stretcher Booster ring (STB ring) of Laboratory of Nuclear Science of Tohoku University. Because the intensity of the electron beam was rather weak (about 300 nA) we concentrate don the measurement of the integrated cross section, ^{232}Th(e, f).

4.1 Experimental Arrangement

The experiment was done at the LDM experimental area of the 2nd experimental hall of the laboratory. The pulsed beam from the linac was stretched by the STB ring up to about 90% duty cycles. The beam hit the target located in the vacuum chamber. The fission fragments ring the PPAC's at both ends of the vacuum chamber partitioned by thin (2 mm) polyethylene films. The beam current after the target was monitored by a secondary emission monitor in front of the beam dump. The experimental arrangement is shown in Fig.6.

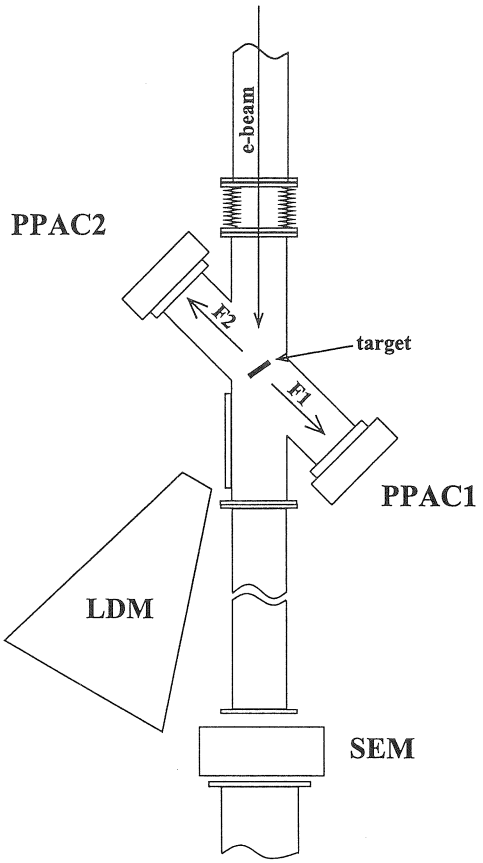

Fig.6. Experimental set up.

4.2 Target

A ^{232}Th target was made by evaporation on a Carbon film of 30 mg/cm^2 thickness. The thickness of the target was 40 μg/cm^2.

4.3 Electronics

We use two PPAC's at both ends of the TOF chamber. Each PPAC consists of two anodes and two cathodes corresponding X and Y directions of the fragment. The arrangement of the electrodes is CAAC for one PPAC, C means a cathode and A means an anode. We use two signals for both ends of an anode: AX1, AX2 (AY1, AY2). Then we deal with altogether 6 signals for one PPAC. The main trigger of the system is an OR of 4 cathodes. The position of the fragment is known by X and Y directions of the anode wire, the TDC between main trigger and the anode wire tells us which wire was hit. The results are important for the corrections of the TOF. The TDC between cathode pulses of PPAC1 and PPAC2 give us the mass difference of the fragments, TOFD.

§ 5. Results and Discussions

5.1 Anode TDC, the positions of the fragments

The TDC spectrum of the anodes for PPAC1 is shown in Fig.7. The start signal of the TDC comes from a cathode (CX or CY) and a stop signal comes from both ends of the delay line (AX1,AX2, AY1, AY2) of the anode wires. TDC of the X-wire is not normal. One reason we found after the experiment is that the cathode for X-wire, CX was damaged by discharge. The contact between cathode cable and cathode surface is easily damaged by this discharge of electricity. When compared with the TDC spectrum in ^{252}Cf measurements (Fig.5), the existence of beam gives a bad influence on the discharge of

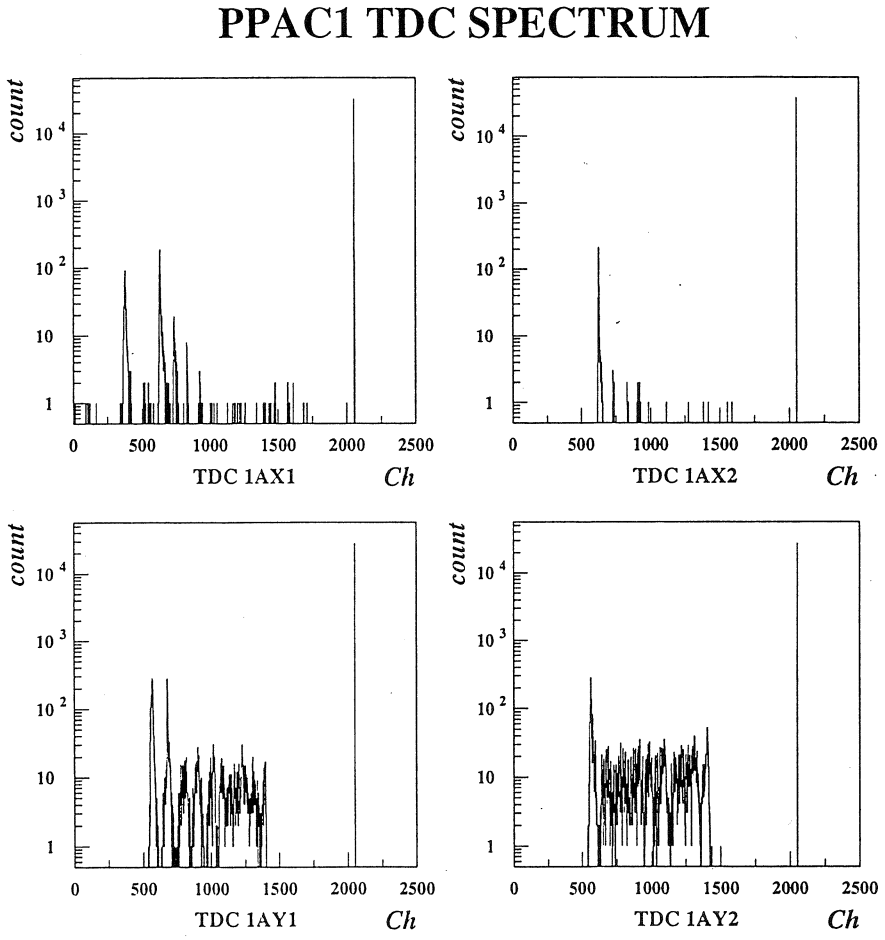

Fig.7. TDC spectra for PPAC1.

electricity of cathode.

5.2 TOFD spectrum

The TDC spectrum between cathodes of both PPAC's is shown in Fig.8. This TDC shows the difference of velocities of fragments getting to the PPAC's. This difference is proportional to the mass difference of the fragments. We can measure the mass difference quite satisfactorily as seen in Fig.8. Since we don't measure scattered electrons, all the excitation energies up to the incident electron energy, 198 MeV, contribute to the spectrum in Fig.8. An (e, f) cross section is obtained by the equation:

$$\sigma(\mathrm{e,\ f}) = N/(Q \times N_t \times DW \times h) \tag{5.1}$$

where

N : number of counts,

Q : number of incident electrons,

N_t : number of target,

DW : solid angle of the PPAC,

h : efficiency of the PPAC,

We assume the efficiency of the PPAC is 100%, we obtain the cross section as,

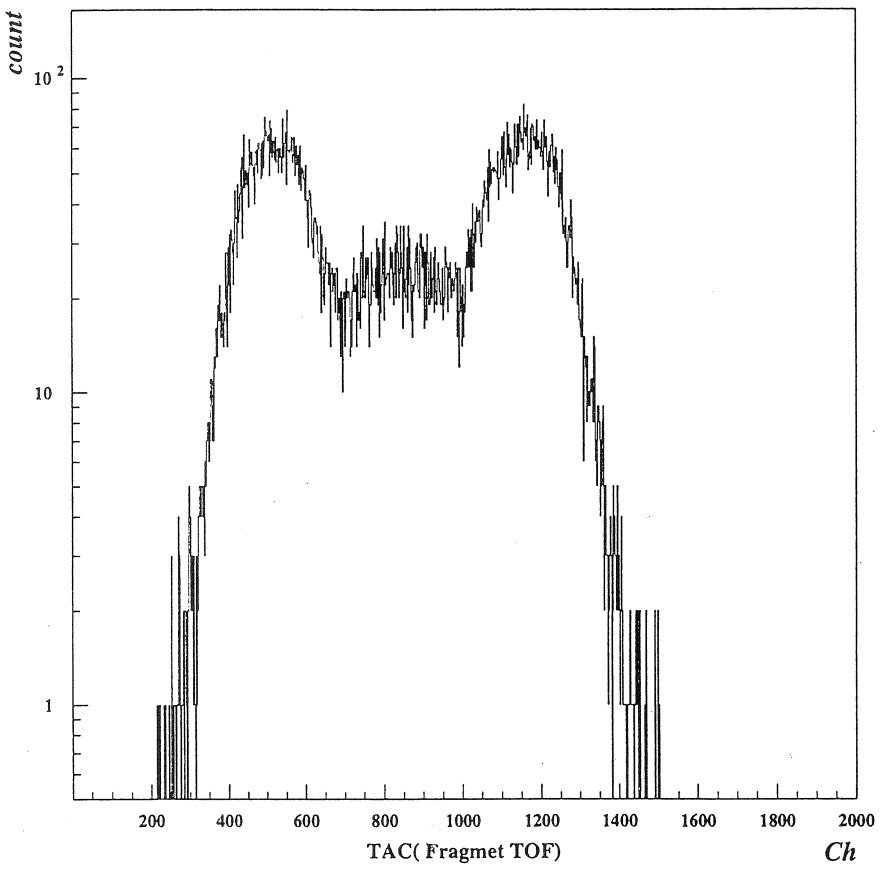

Fig.8. TOFD spectrum.

$$\sigma(\mathrm{e, f}) = 3.4 \pm 0.025 \text{ mb} \quad \text{at } E_e = 198 \text{ MeV}$$

This value is about twice larger than $\sigma(\mathrm{e, f}) = 1.6$ mb which is expected from the $^{232}\mathrm{Th}(\gamma, \mathrm{f})$ value obtained by Shotter *et al.*[2], and using the virtual photon spectrum. The discrepancy may come from the theoretical uncertainty of the virtual photon spectrum.

§ 6. Conclusions

We have made two PPAC's for the purpose of measuring the asymmetric to symmetric fission ratio for actinide nuclei. There is a story that this ratio depends on the multipolarities of the excitations. We choose Thorium as a target, and tested how we can measure the fission fragments using the PPAC's.

The results are,

1) The position resolution of 2 mm is obtained by the test using ^{252}Cd radioactive source.
2) When we used PPAC's in an electron beam, anode TDC sometimes showed strange responses and we can not fully understand the reason.
3) Mass difference of the fragments is clearly obtained as the TOFD spectrum. We can easily estimate the ratio of asymmetric to symmetric fission in case of $^{232}\mathrm{Th}(\mathrm{e, e'f})$.
4) We can estimate the $^{232}\mathrm{Th}(\mathrm{e, f})$ cross section as 3.4 ± 0.025 mb.

References

[1] Th. Weber *et al.* : Phys. Rev. Lett. **62** (1989) 129.

[2] A.C.Shotter *et al.* : Nucl. Phys. **A290** (1977) 55.

Photon Tagging System for 1.2 GeV STB Ring (STB Tagger)

H. Yamazaki, T. Kinoshita, K. Hirota, T. Nakabayashi,
A. Katoh, T. Katsuyama, T. Itoh and J. Kasagi

Laboratory of Nuclear Science, Tohoku University, Mikamine, Taihaku-ku, Sendai 982-0826

The construction of the STB ring at LNS, Tohoku University has been completed in 1997. We have developed the STB tagger in these years and quasi monochromatic photon beams with energies up to 1.1 GeV are ready to use for nuclear physics experiments. The outline of this tagging system was reported in ref. [1] and the internal radiator system in ref. [2]. In this report, we describe a performance of the tagged photon beam.

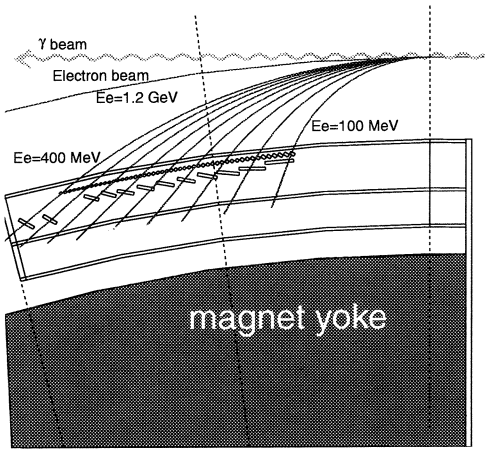

Fig.1. Electron orbits in the bending magnet.

The STB ring is an electron synchrotron, which can provide an internal electron beam with energies up to 1.2 GeV. The STB Tagger consists of a movable carbon fiber radiator, compact tagging counters and a bending magnet of the STB ring, which is used as the tagging spectrometer. The injected electrons with 200 MeV of energy are accelerated up to 1.2 GeV in about 1 second. After the acceleration the photon production radiator is inserted into the electron beam orbit and produces bremsstrahlung photons. An energy of photon is deduced from the difference between an incident energy and a recoil electron one. ASTB bending magnet, BM4, which is used to analyze momenta of recoil electrons, is a C-shaped dipole magnet [3]. The total deflection of the main beam in a magnet is 45° with a bending radius of 3 m. The field strength is 1.33 T at the maximum energy. The orbits of the 1.2 GeV electron beam and recoil electrons are shown in Fig.1. The position sensitive tagging counter is installed in the bending magnet so as to detect the recoil electrons with energies from 100 MeV to 400 MeV. The tagging counter consists of 50 ch position counters and twelve backup counters. Thus the energy range of the

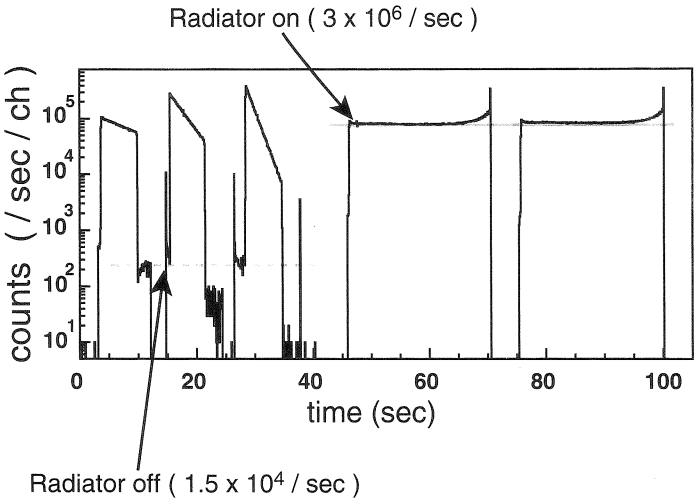

Fig.2. Time evolution of the tagged photon intensity.

tagged photon is from 0.8 GeV to 1.1 GeV, and the energy bin is 6 MeV, when the energy of electron is 1.2 GeV.

The beam intensity is considered to be distributed according to the normal distribution with $\sigma =$ 1.0 mm. Since the probability of emitting photons is proportional to the electron beam, the intensity of the tagged photon beam reduces exponentially with the fixed radiator position. The constant photon flux can be obtained by moving the radiator so as to compensate the reduction of the beam intensity. In Fig.2, the typical examples of the time evolution of the tagged photon flux are shown. The left three parts correspond to tagged photon intensities measured with the radiator positioned at 3.5σ, 3.0σ and 2.5σ from the beam center, respectively. The right two parts show the constant tagged photon intensities measured by moving the radiator. As expected, the photon intensity can be successfully fixed during about 25 s. The tagged photon intensity is about 3×10^6 / s, and the counting rate of the tagging counters without a radiator is about 1.5×10^4 / s, as shown by thin solid and doted lines, respectively. The radiator off/on ratio is less than 0.5%. The duty factor of 85% can be obtained.

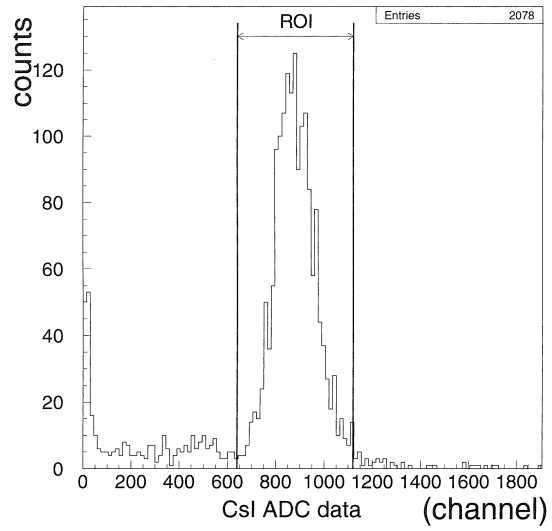

Fig.3. Pulse height spectrum of the CsI detector.

The tagging efficiency (ε), which is defined as the ratio of the real photon numbers to the electron counts of the tagging counter, was directly measured with a CsI crystal detector. The size of the CsI crystal was 50 × 50 × 250 mm, being large enough to cover the tagged photon beam profile. The pulse height information of the CsI detector output was accumulated when a tagging counter was fired. The measured pulse height spectrum of the CsI detector is shown in Fig.3, where events with correct tagged photon energies are shown by ROI. The tagging efficiency can be calculated as the ratio of the integral of ROI to total integral; $\varepsilon = 78\% \pm 2\%$.

The 1.2 GeV STB Tagger installed in the STB ring is now ready to be used for varios expeninents with the maximum intensity of the tagged photon beam of about 10^7 / s and with its energy range from 0.8 to 1.1 GeV. The study of the N* in nuclei is one of the projects to be done by using the STB Tagger.

References

[1] H. Yamazaki *et al.* : Research Report of LNS **33** (2000) 30.

[2] K. Hirota *et al.* : Research Report of LNS **33** (2000) 33.

[3] B. Feng *et al.* : Research Report of LNS **30** (1997) 95.

Design and Construction of Tagging Counters for STB Tagger

T. Kinoshita, T. Itoh, H. Yamazaki, K. Hirota*,
T. Nakabayashi and J. Kasagi

Laboratory of Nuclear Science, Tohoku University, Mikamine, Taihaku, Sendai 982-0826

The STB ring at our laboratory, completed in 1997, is ready for nuclear physics experiments with GeV electrons and photons. We have developed a 1.2 GeV photon tagging system (STB Tagger) which is one of the main project of the STB ring. The design of the whole system is reported in ref. [1]. and that of a movable radiator system is reported in ref. [2]. Here, we report on the development of tagging counters.

In the STB Tagger, one of the dipole magnet (BM4) of the STB ring also serves as a momentum analyzer of recoil electrons, and the position detectors should be placed in a small room between the pole piece and the return yoke, as shown in Fig.1, where a cross section view of BM4 is drawn. Basic requirements for the tagging counters are, thus, (1) not to use any electric conductor as parts of the counter in the small room, and (2) to make the system as small as possible so as to fit itself in the room and to insert and remove it easily, in addition to the general requirements such as energy (ΔE = 3 MeV for a goal) and time resolution (ΔT = 500 ps).

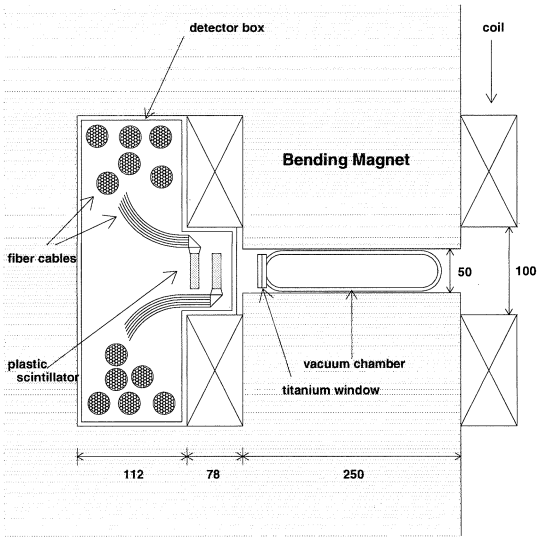

Fig.1. Cross section view of BM4. The position detectors should be placed in a small room between the pole piece and the return yoke.

*Present address: SPring-8, JASRI, Sayo-Gun, Hyogo 679-5198

We have employed a plastic scintillator coupled with a bundle of 3 m long optical fiber, through which scintillation lights are transmitted to a phot-omultiplier (PMT; Hamamatsu H6524-01) placed at outside of BM4, because a plastic scintillator can be easily processed in any form, gives a good time resolution and is less expensive. The plastic scintillator is in a shape of a rectangular prism with a base 5 × 5 mm and a height of 20 mm; the 5 mm width corresponds to an energy span of 6 MeV at 1 GeV. Fifty scintillators are aligned at the front surface of a detector box so that photons with energies from 800 MeV to 1.1 GeV can be tagged simultaneously for 1.2 GeV circulating electrons in the STB ring. Behind the position detectors placed are 12 plastic scintillators serving for backup counters. Optical fibers are quite useful to transport the light through a path in flexible, winding and long. Employed is a optical fiber of 1.0 mm in diameter manufactured by Mitsubishi Rayon Co., Eska CK-40. Sixty eight fibers are tied up in a bundle. Both ends of the bundle are closely packed and tightly hardened; they show circular cross sections of 9.0 mm in diameter fitting to the PMT.

It is inevitable for the present system to lose the intensity of the light during the transmission from the scintillator to the PMT, mainly due to a difficulty of light transmission from the scintillator to the optical fiber. Moreover, the scintillation light produced by a high-energy electron punching through the plastic scintillator is not intensive enough at all; the ionization energy loss is only 1.0 MeV for 5 mm thickness of plastic. Thus, in order to obtain electron events clearly separated from thermal noises of the PMT, a method in which the loss of the light is a very tiny amount or zero should be developed.

We have devised a light guide connecting the scintillator and the optical fibers. The optical fiber used has a critical angle of 30°. This means that the light which goes with an angle to the axis of the fiber larger than 30° cannot penetrates into the fiber; in naive consideration, 87% of the intensity of the incident light is lost. Figure 2 shows a view of the light guide with a scintillator designed for the present tagging detectors. As shown, the light guide is in a shape combined with two geometrical parts; a trapezoidal square prism and a triangular prism. The former increases the intensity of light accepted by the fiber cable, since a reflection of the wall always makes the light to be more parallel to the axis of the fiber cable. The latter just serves as an optical prism to change the direction of the light. Thus, the light transmittal efficiency is expected to depend mainly on the angle α and the length h shown in Fig.2. Various geometries of the light guide under the realistic constraint for the tagging counters were tested experimentally as well as with simulations by a code GUIDEIT [3]. We have found that the light guide should be in a shape of a circular cone or a pyramid without a top; the height must be larger than 8 mm for the upper side 5 mm and the lower side 10 mm.

Usefulness of the light guide is demonstrated in Fig.3, where energy spectra of electrons emitted from ^{90}Sr are shown. Fig.3 (1) shows a spectrum measured with the PMT directly coupled to the scintillator; a peak at around 660 ch corresponds to electrons punching through the scintillator. When the scintillation light is simply transported through the optical fibers, i.e., the scintillator couples with the optical fibers, the spectrum changes as shown in Fig.3 (2). As expected, only 35% of the light can reach to the PMT. However, the light guide drastically improves the situation as shown in Fig.3 (3), where the spectrum measured with the light guide between the scintillator and the optical fiber is

shown. The pulse height of the electron recovers to about 70% of the initial one.

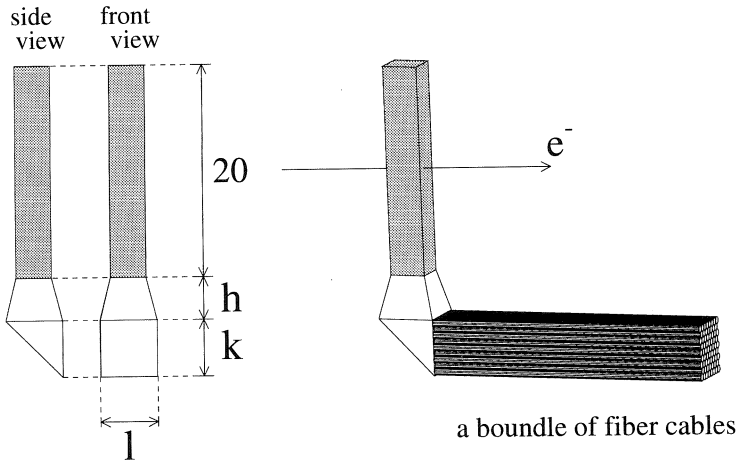

Fig.2. Views of a light guide and a plastic scintillator with optical fiber cables designed for the STB Tagger.

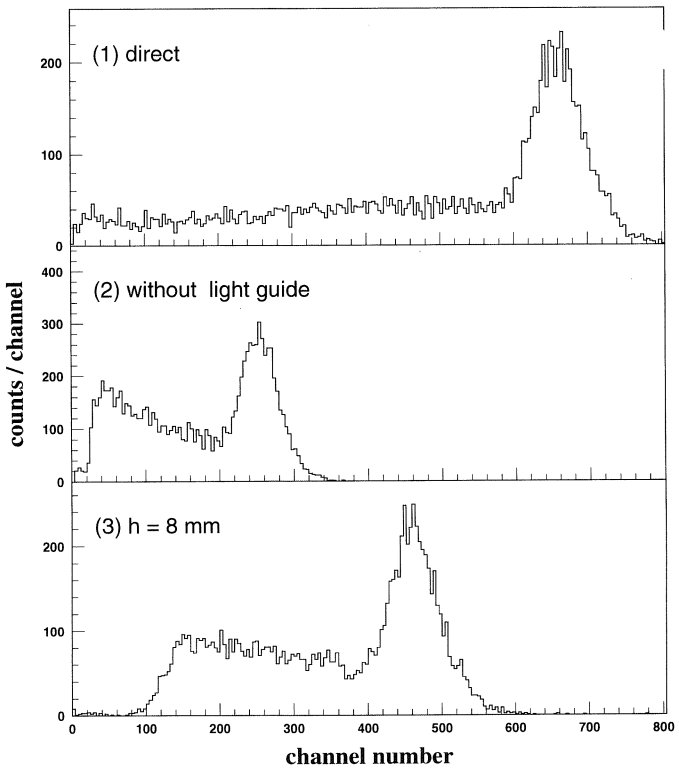

Fig.3. Pulse height spectra from the PMT; (1) the scintillator glued directly to the PMT, (2) the scintillator glued to the fiber cables without a light guide, (3) light guide with $h = k = l = 8$ mm.

The detector system of the final geometry was tested in an actual condition. The detector box in which five detectors were installed was placed at the right place in the bending magnet of the STB ring. In Fig.4, the measured pulse height spectrum of the tagging detector is shown. The peak at around 335 ch corresponds to the electron events. They are clearly separated from electrical noises, which are

supposed to appear just below 40 ch but suppressed by a discriminator. The arrow at around 530 ch indicates the pulse height simply predicted from the measurements mentioned in the previous section (measured with 10 cm long fiber cables). This reduction of the light intensity seems to be inevitable because of the absorption in the fiber cables. Nevertheless, the light intensity of about 65% can be obtained by using 3 m long fiber cables, in the present case.

In summary, the contrived light guide inserted between the plastic scintillator and the fiber cables has improved the light transmittal efficiency significantly: the light of 45% of its initial amount at the plastic scintillator can arrive at the PMT placed at 3 m from the scintillator (30% loss at the entrance of the fiber cables and 35% absorption for the 3 m long cables). It should be noticed that the light intensity would be further reduced down to about 20% unless the light guide is in use. Moreover, the suppression of the loss of light intensity during transmission has realized time resolution of 0.53 ns, which is another important feature required for the tagging detector. Therefore, the tagging counter system of the STB Tagger is expected to work well in the future nuclear physics experiments.

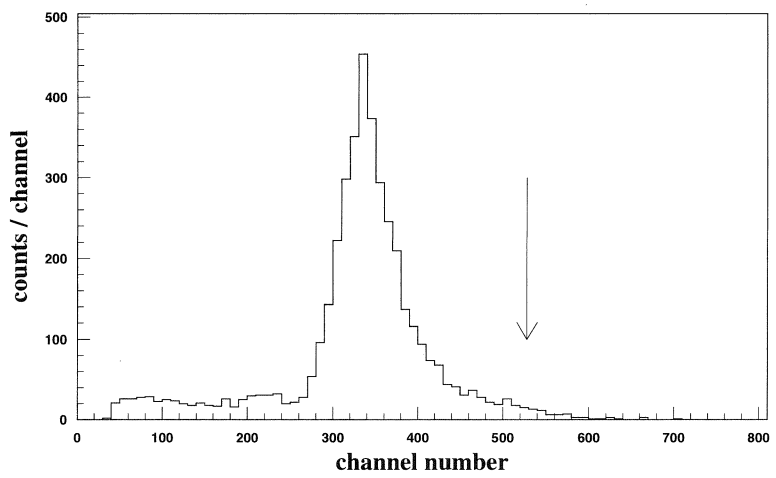

Fig.4. Pulse height spectrum of a tagging detector measured with a 1.2 GeV electron beam in an operative condition. The arrow indicates the pulse height position simply expected from the measurement with 10-cm long fiber cables.

References

[1] H. Yamazaki *et al.* : Research Report of Laboratory of Nuclear Science **33** (2000) 30.

[2] K. Hirota *et al.* : Research Report of Laboratory of Nuclear Science **33** (2000) 35.

[3] D. A. Simon : GUIDEIT V1.1 User Manual, October 1993.

Solid Hydrogen Target for GeV Photon Experiments

T. Nakabayashi, A. Katoh, H. Yamazaki, K. Hirota and J. Kasagi

Laboratory of Nuclear Science, Tohoku University, Mikamine taihaku, Sendai 982-0826

We have developed a solid hydrogen target system for GeV photon experiments at LNS, especially for the H(γ, η) and D(γ, η) experiments. A GeV tagged photon beam produced by the STB Tagger collides with a target which is placed at a distance of 7.5 m from the radiator inside the STB ring [1,2]. The maximum intensity of the tagged photon, which is limited by the chance coincidence yields, is about 10^7 photons/sec, and the size of the beam at the target position is about 2 cm in diameter. Thus, in order to proceed the experiments effectively, we need a target having a large volume, at least larger than 3cm×3cm×2cm (height×width×length).

Since the energy deposit of the photon beam in the target is very small, we have designed a solid hydrogen target system with a commercially available 4K-GM cryocooler [3], the cooling power of which is not so large. The GM-cryocooler has two cold stages, which are called the 1st and the 2nd stage, and are 12 and 6.4 cm in diameter, respectively. The cooling power is 20 W for the 1st stage at 30K and 1 W for the 2nd stage at 4K. The 2nd stage can be cooled down to 4K within about an hour by setting a 30K radiation shield on the 1st stage.

In Fig.1, we show a vacuum chamber combined with the cryocooler, which was designed on trial as a solid hydrogen target surrounded by a multi-detector system SCISSORS [4]. A cylinder of 17 cm in outer diameter and 50 cm in height contains the GM-cryocooler. The inside of the chamber is evacuated to about 10^{-5} Pa with a turbo molecular pump and to 10^{-8} Pa with the cryocooler. The solid hydrogen is generated on the 2nd stage just below the beam line. The 30 K radiation shield made of copper (not drawn in Fig.1) has two holes for the photon beam, and the flanges on the beam line have mylar windows, through which one can directly watch how the solid hydrogen grows up.

Since the triple point of hydrogen is 13.8 K, it is possible to convert a hydrogen gas directly to a solid phase; this is the method employed presently. As shown in Fig.2, an airtight room is provided on the 2nd stage of the cryocooler. It is surrounded with acrylic walls and ceiling on which a Teflon inlet is connected. The gas inlet is used not only to supply the hydrogen gas into the room but also to lift and lower the whole acrylic cover of the solid hydrogen. The airtight condition can be realized by pressing the walls against to the copper floor, because a thin indium sheet is attached at the bottom surface of the walls and makes inside of the walls be pressurized in the vacuum chamber.

We have established a method to produce a large volume of solid hydrogen after many trials. The essential points are to keep the temperature of the airtight room as low as possible and to keep the

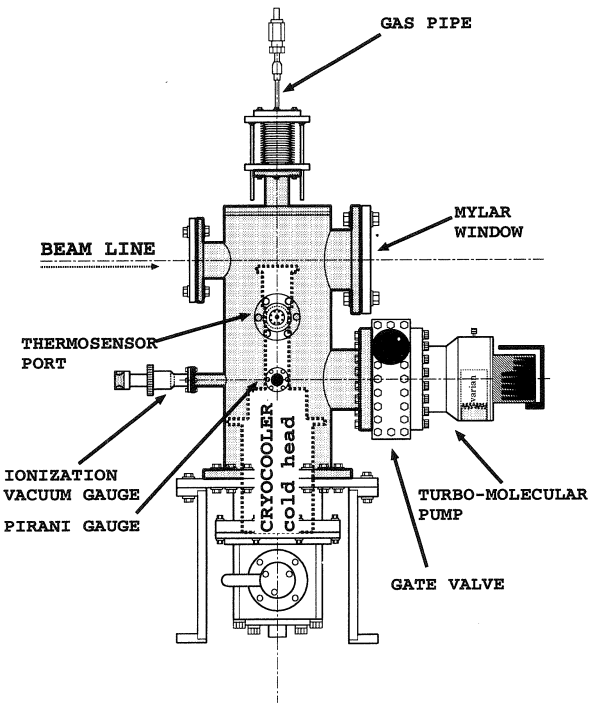

Fig.1 : Solid hydrogen target chamber.

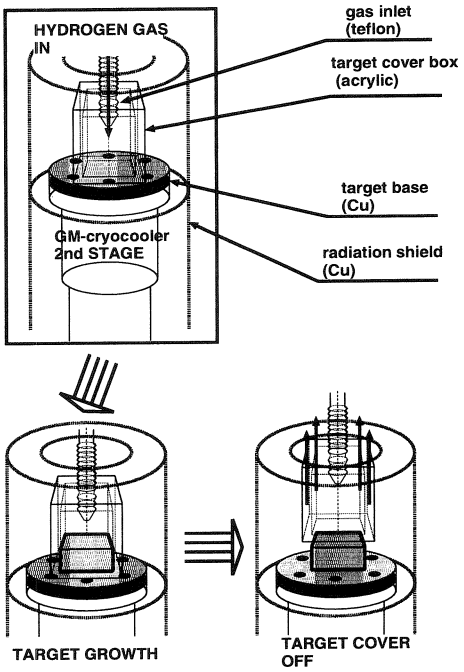

Fig.2 : The setup inside the target chamber.

pressure as high as possible. It was found that about two hours are required with a constant gas flow of 2 cc/sec to make a solid hydrogen of 3.6 cm × 3 cm × 2 cm in a shape of rectangular prism. It needs at least another hour before the acrylic cover is removed, since the upper surface of the solid hydrogen may not be frozen hardly just after the gas flow stops. The solid hydrogen made in the present method can last very long and the H (γ , η) measurement has been successfully carried out for about 4 days without any loss of the target. During the GeV photon bombardment, the vacuum inside the chamber was about 10^{-4} Pa, which is the vapor pressure of hydrogen at 4 K.

Reference

[1] H. Yamazaki *et al.* : Research Report of LNS, Tohoku Univ. **33** (2000) 30.

[2] K. Hirota *et al.* : Research Report of LNS, Tohoku Univ. **33** (2000) 33.

[3] M. Kojima : Master's Thesis, TIT. (1999).

[4] K. Hirota *et al.* : Research Report of LNS, Tohoku Univ. **33** (2000) 35.

A Test of the Gamma Ray Detector for the GDH-Experiment at SPring-8

I. Daito[1], M.Geso[2], S.Hasegawa[3], N. Horikawa[1], H.Ichihara[3], T. Iwata[3], K. Kondo[3], D.Menze[1,4]*, Y. Miyachi[1†], H.Nakayama[3††], S.Tanoshima[3] and A.Wakai[3§]

[1] *CIRSE, Nagoya University, Furo-cho, Chikusa-ku, Nagoya, 464-8602*
[2] *Department of medical radiations science, Royal Melbourne Institute of Technology, PO Box 71, Bundoora, Vic 3083, Australia*
[3] *Department of Physics, Nagoya University, Furo-cho, Chikusa-ku, Nagoya, 464-8602*
[4] *Physikalisches Institut, Universität Bonn, D-53115 Bonn, Germany*

A prototype gamma ray detector for the detection of π^0 in the proposed experiment at SPring-8 to study the GDH sum rule (GDH experiment) has been built and tested. The detector is fabricated with lead-scintillator tiles and wave length shifter (WLS) fiber readout. High detection efficiency (above 85 %) for the gamma rays is the most important requirement for this detector. It has been tested with the tagged photon beam at LNS of Tohoku University. The results of the test alongside some Monte Carlo simulation are presented. The evaluated efficiency ranging in energy above 50 MeV is higher than 90%.

§ 1. Introduction

The proposed experiment [1] at SPring-8 facility aims at measuring the helicity dependent total photoabsorption cross-sections of the proton at photon energies ranging from 1.5 to 2.9 GeV. The results will be employed alongside other proposed measurements at other parts of the world to test the validity of the Gerasimov & Drell-Hearn(GDH) sum rule [2]. The polarized photon beam from the LEP beam line at SPring-8 which is currently operational [3] will be used as a source for circularly polarized photons. Essential feature of the experiment is a complete detection of hadronic final states using a 4π detector setup as displayed in Fig.1. Some detectors will be encompassed inside the bore of the superconducting solenoid magnet of the polarized target.

The gamma ray detector to be installed around the target is required to have a satisfactory efficiency and a large geometrical coverage for gamma rays of energies higher than 70 MeV which mostly originate from π^0. This requirement becomes even harder to fulfill due to (1) limited space (about 60 cm) inside the magnet bore where the detector will be placed and (2) the influence of the high magnetic field (2.5 T) of the superconducting magnet of the polarized target. A sampling calorimeter

*Present address: Physikalisches Institut, Universitat Bonn, D-53115 Bonn, Germany.
†Present address: Physics Department, Tokyo Institute of Technology, 2-12-1, Oh-okayama, Meguro, Tokyo 152-8551.
††Present address: Department of Physics, Chiba University, 1-33, Yayoi, Inage-ku, Chiba, 263-8522.
§Present address: Akita Industry Promotion Foundation(AIPF), 3-1-1, Sanno, Akita-city, Akita, 010-8572.

type detector consisting of lead and plastic scintillator tiles with WLS fibers for readout would be a possible solution. The WLS fiber couples into a long light guiding fiber which transmits the secondary emitted light to a photomultiplier tube (PMT). This PMT is placed away from the superconducting magnet to avoid the influence of the magnetic field.

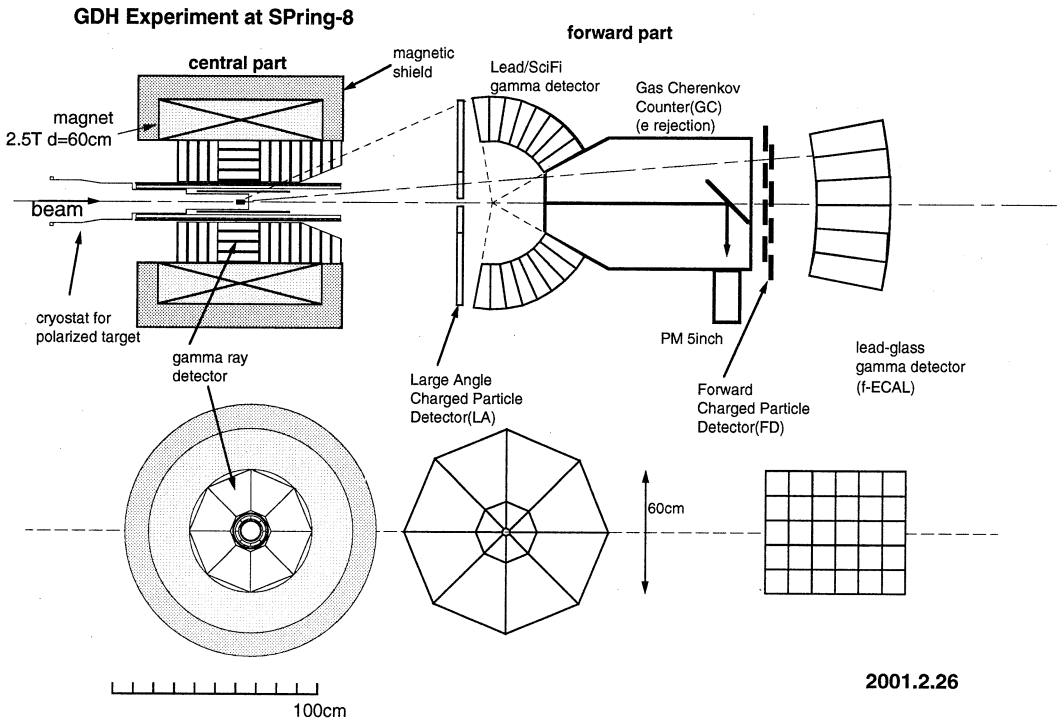

Fig.1. The setup of the GDH experiment at SPring-8.

§ 2. Design of the detector

The design of this detector is based on the following requirements to make suitable for the proposed experimental setup: (1) thickness of the detector along the gamma rays is required to be less than 20 cm; (2) detector's efficiency must exceed 85% for gamma rays of higher energy than 70 MeV; (3) the dead space should be as narrow as possible; and (4) the PMT is to be placed at about 3 meters away from the magnet. One of the major hurdles faced is the requirement for high detection efficiency with such small thickness compared to that of conventional calorimeters. Accordingly, the number of sampling layers and the thickness of the scintillator and lead tiles are appropriately determined.

The number of the sampling layers and the tiles thickness appropriate to obtain high detection efficiency are determined by using GEANT simulation [4]. The efficiency was based on the fraction of the events which are results of an energy deposit higher than the threshold energy of 10 MeV. Then the detection efficiency under the condition of detector's total thickness to be less than 170 mm was obtained as shown in Fig.2 as a function of the number of the sampling layers (n_s) and the ratio of the thickness of the scintillator and lead tiles ($R=t(\text{scin.})/t(\text{lead})$), where the thickness is measured in a unit of mm. The detection efficiency first increases according to n_s and then saturates. On the contrary, regarding R; it seems that there is a nominal R value which gives maximum efficiency.

Our simulation results show that efficiencies above 85% are obtainable with n_s value more than 17 and the ratio R ranging between 3 to 5. Accordingly, n_s value of 18 and the R ratio of 5 were selected for this detector's design. These results lead to the following detector's configuration: t(scin.) = 8.0 mm, t(lead) =1.6 mm and the total detector's thickness of $5.4X_0$ (where X_0 is a radiation length).

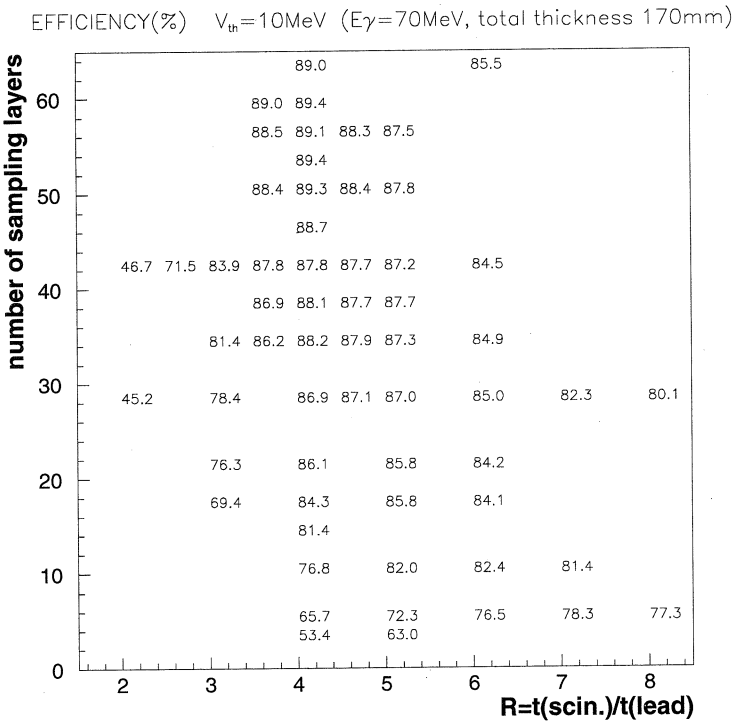

Fig.2. Efficiencies (in %) as a function of number of sampling layers and the ratio R.

§ 3. Description of the detector

This detector has a trapezoidal cross section and covers a 1/8 section ($\Delta\phi = 45^\circ$) in the azimuthal angle as shown in Fig.3. It consists of 18 sampling layers of different areas, the smallest at the top and the largest at the bottom. The smallest layer is No.1 and its area is 75 × 200 mm^2 and the largest is No.18 and it is 210 × 200 mm^2 in area. Each layer consists of a lead tile of 1.6 mm thickness and a scintillator tile of 8 mm thickness. The scintillator tiles are cut from a BC412 Bicron scintillator plate. Grooves were etched on the surface of the scintillator tiles by a round edge cutter. Two different shaped grooves are formed; race-track and S type. The first type is adopted for the large area tiles i.e. from No. 6 to 18. The groove depth around 2.6 mm allows two turns of the WLS fiber to be installed in the tile. The diameter of the groove circles is made as large as possible in order improve the light collection. The second type, S type, allows only a single trace through the S-shaped groove of 1.6 mm in depth. This type is adopted for the first five tiles from No.1 to 5. WLS fiber Y-7(100) of 1 mm diameter from Kuraray is used in all the tiles. A small disc made of an aluminized Mylar sheet is glued on one end of the WLS fiber to form a light reflector. The other end of the WLS fiber is glued to the light guiding fiber 3m long. The other end of the light guiding fiber is directly attached to the PMT (Hamamatsu H1161). The four sides of the scintillator plate are painted with Bicron BC-650 white paint and the top and the bottom sides are covered with aluminized Mylar sheets.

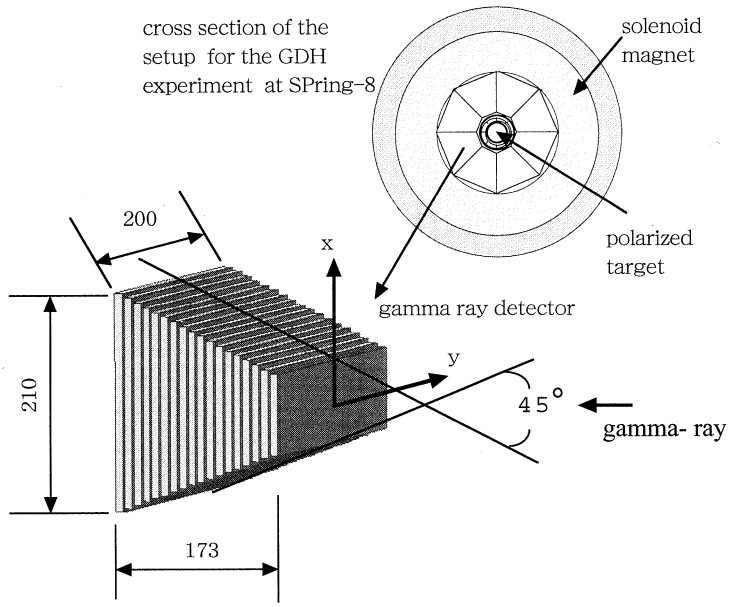

Fig.3. The schematic view of the prototype for the gamma ray detector.

§ 4. Gamma ray detection efficiency

Gamma ray detection efficiency is measured using the tagged photon beam delivered by the booster synchrotron at LNS. The beam energy ranges between 600 to 800 MeV and the energy resolution of the tagging system is about 4.7 MeV. The experimental setup is displayed in Fig.4. To veto charged particles in the beam, scintillation counters, T1, T2 and a Gas Cherenkov counter, C1 are used. The prototype gamma ray detector, Ga, is followed by a lead glass calorimeter, LG which allows calibration of the photon flux. An event selection was made, in order to eliminate photons not reaching Ga, requiring that at least one of Ga and LG gives a significant signal.

The pulse height distribution of the prototype gamma ray detector obtained for photons of 630 MeV shows asymmetric shape with a tail in the lower energy region due to leakage of a shower as displayed in Fig.5. It is well reproduced by our simulation using the GEANT4 package [5]. Setting the threshold at 4 photo electron level, the detection efficiency was calculated to be 97.1 $\pm$0.2%. We evaluated it also at different energies using the Monte Carlo simulation. The results are shown along with the experimental value in Fig.6. It was found detection efficiencies were satisfactorily high for the use of the proposed GDH experiment: above 90% at the energies higher than 50 MeV.

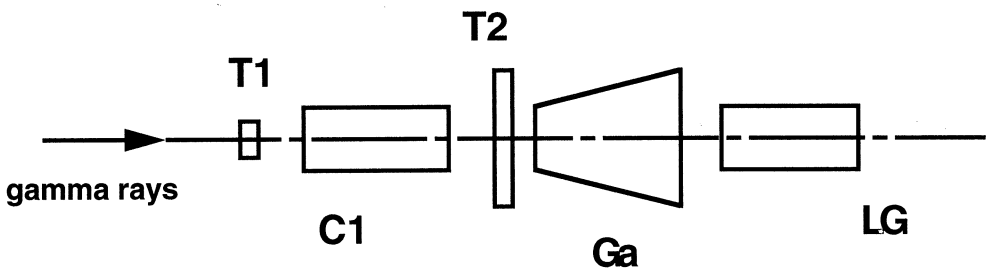

Fig.4. The experimental setup to measure detection efficiencies for gamma rays at LNS of Tohoku University. T1, T2: veto counters, C1: gas Cherenkov counter (veto), Ga: the gamma ray detector on test, LG: lead glass calorimeter.

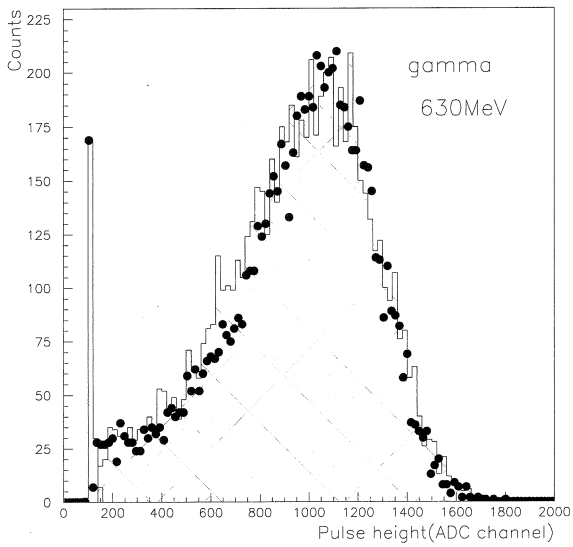

Fig.5. The pulse height distribution for gamma rays at 630 MeV along with the results of the Monte Carlo simulation displayed with the closed circles. The cross hatched area shows the events above the threshold set at 140 channed corresponding to 4 photo electron level. The fraction of the events in the hatched area to the total events gives the detection efficiency, 97.1±0.2%.

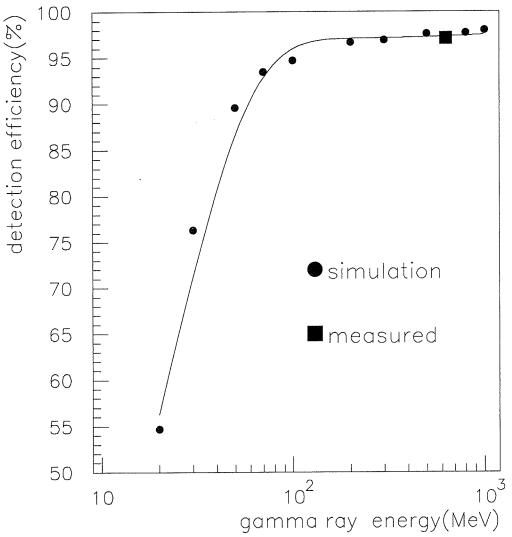

Fig.6. The detection efficiency for gamma rays as a functiion of energy. The closed square is the measured value. The closed circles are obtained in the simulation. The solid line is for an eye guide.

§ 5. Conclusion

The prototype of the gamma ray detector specially designed to be used in the proposed GDH experiment at SPring-8 has been fabricated with lead and scintillator tiles using WLS fiber readout. It has been tested with the tagged photon beam at LNS. The detection efficiency was measured and also evaluated based on the simulation. It was found to be higher than 90% at energies above 50 MeV. This result meets the requirement of the proposed GDH experiment.

Aacknowledgement

We would like to express our gratitude to the accelerator crews of LNS of Tohoku University for their effort to maintain the beam condition. We would like to thank Dr. H. Yamazaki of LNS-Tohoku University for his effort in arrangement of our experiment.

References

[1] T.Iwata : *Symposium on The Gerrasimov-Drell-Hearn Sum Rule and the Nucleon Spin Structure in the Resonance Region, Johannes Gutenberg-Universitaet, Mainz, June 14-17, 2000.*

[2] S.B.Gerasimov : Yad. Fiz. 2 (1965) 598, Sov.J. Nuci.Phys. **2** (1996) 430.

[3] S.D.Drell and A.C.Hearn : Phys. Rev. Lett. **16** (1966) 908.

[4] J.K.Ahn *et al.* : *12th Symposium on Acceierator Science and Technology*, 141-143, 27 Oct.1999, Wako, Japan,P.141.

[5] R.Brun *et al.* : *GEANT3 Users Guide* CERN/DD/EE/84(1987).

[6] K.Amano *et al.* : Nucl. Instr. and Meth. **A 453** (2000) 455.

Ⅱ. Radiochemistry

A Radiochemical Study for the α-Decay of ^{229m}Th

T. Mitsugashira[1], M. Hara[1], T. Ohtsuki[2], K. Takamiya[3],
Y. Kasamatsu[4], A. Shinohara[4], H. Kikunaga[5] and T. Nakanishi[5]

[1]*The Oarai-branch, Institute for Materials Research, Tohoku University, Oarai-machi, Ibaraki 311-1313*
[2]*Laboratory of Nuclear Science, Tohoku University, Mikamine, Taihaku, Sendai 982-0826*
[3]*Research Reactor Institute, Kyoto University, Kumatori, Osaka 590-0494*
[4]*Graduate School of Science, Osaka University, Toyonaka, Osaka 560-0043*
[5]*Graduate School of Science, Kanazawa University, Kanazawa 920-1192*

The decay of low energy isomeric state of ^{229m}Th was explored applying a novel radiochemical technique to the (γ, xn) reaction products on ^{230}Th target. The decaying α-emitter was observed between 4.687 MeV α-peak of ^{230}Th and the α-peaks of the (γ, 2n) product ^{228}Th. The energy of the decaying component is consistent with the expected energy for the α-particles from ^{229m}Th. The half-life of the decaying component was determined to be 13.9±3 hours. It seems that the present determination of the half-life is the longest value for ^{229m}Th, because fluoride has no valence electrons that undergo electronic bridge interaction with the thorium nucleus.

§ 1. Introduction

The excitation energy of the low energy nuclear isomer ($3/2^+$ [631]) of ^{229}Th (ground state $5/2^+$ [633]) was reported to be less than 5 eV and 3.5 eV in ^{230}Th(d, t) scattering [1] and precise gamma ray spectroscopy [2], respectively. Because the excitation energy is lower than the first ionization potential of thorium and, thus, the emission of an internal conversion electron is prohibited, ^{229m}Th decays through a direct γ transition (nuclear UV emission) and the electronic bridge mechanism (EBM) [3]. This implies that the half-life of ^{229m}Th depends on its chemical state that relates to the probability of EBM. Irwin and Kim [4] reported the detection of nuclear UV emission resulting from the de-excitation of ^{229m}Th that was formed in precursor ^{233}U and, separately, Richardson *et al.* [5] reported a similar result by using a liquid ^{233}U sample. These findings were carefully re-examined by Utter *et al.* [6] and Shaw *et al.* [7] applying a much more sophisticated photon detection system. They claimed that the photons observed in the previous two studies seemed to be caused by α-particle induced fluorescence of N_2. According to the recent compilation of the decay scheme of ^{233}U [8], only less than 0.6% of the α-decay of ^{233}U leads to the formation of ^{229m}Th. The difficulty of the direct observation of nuclear UV-rays from ^{229m}Th results from this low probability. Our research group also has interest in ^{229m}Th. But, we selected a different approach to investigate the decay of ^{229m}Th.

Table 1. Levels of ^{225}Ra and the α-transition from ^{229}Th.

Orbit	Excitation Energy/keV	α-branch from ^{229}Th (%)	E_α/MeV
[631] $1/2^+$	0	weak	5.079
$3/2^+$	42.77	0.24	5.036
$5/2^+$	25.41	6.6	5.053
$7/2^+$	111.60	5.97	4.968
$9/2^+$	100.5	3.17	4.978
[631] $3/2^+$	149.96	0.16	4.930
$5/2^+$	179.75	10.2	4.901
$7/2^+$	243.6	5.0	4.836
[633] $5/2^+$	236.3	56.2	4.845
$7/2^+$	267.9	9.3	4.815
$9/2^+$	321.8	1.9	4.761

Our strategy is the direct observation of α-decay of ^{229m}Th to determine its half-life. The most favored α-transition from the ground state of ^{229}Th feeds the $5/2^+$ [633] state at 235.6 keV level of ^{225}Ra and its rotational band, and only rather weak α-transitions are observed with higher energies, as are shown in Table 1. The transition to the 149.96 keV $3/2^+$ [631] level of ^{225}Ra (E_α = 4.930 MeV) that is expected to be the most favored α-transition from ^{229m}Th has a branching ratio of only 0.16% from ^{229}Th. In addition, the α-transition to the parity coupled $3/2^+$ state at 42.77 keV that is assigned to the rotational band of the ground state of ^{225}Ra($1/2^+$ [631]) is also expected to be another favored α-transition from ^{229m}Th. As a result, the α-particles from ^{229m}Th have larger energies than those from ^{229}Th. This implies that the partial half-life of the α-transition from ^{229m}Th is considerably shorter than that of ^{229}Th, and that the α-particles might be observable when ^{229m}Th is produced by a suitable reaction. Instead of the α-decay of ^{233}U, we selected the ^{230}Th(γ, n) reaction to produce ^{229m}Th

§ 2. Experimental

About 30 μg of 95% ^{230}Th was molecular-plated on a 5N aluminum plate with a diameter of 10 mm and then enclosed in a quartz tube for bremsstrahlung irradiation. The irradiation was carried out using the Electron Linear Accelerator of Tohoku University. The linac was operated at electron energies of 22 MeV and 30 MeV with the beam pulse width of 3 μs, peak current around 100 mA, and the pulse repetition rate of 300 s^{-1}. The quartz tube containing the ^{230}Th target was placed horizontally along with the central axis of the bremsstrahlung in close contact with the back of a platinum converter of 0.71 radiation length (2 mm) and cooled by running tap water during irradiation for 10 hours.

After the irradiation, the ^{230}Th target was dissolved in 8 M (mol/dm^3) nitric acid solution, and the solution was passed through an anion exchange column to sorb the thorium isotopes. After washing the column with 20 column volumes (60 cm^3) of 8 M nitric acid solution to remove fission products, the remained thorium isotopes were eluted from the column in about 15 cm^3 of 2 M hydrochloric acid solution. The thorium isotopes were then coprecipitated with samarium trifluoride by adding to the effluent 100 μg samarium and hydrofluoric acid solution. The precipitates were filtered on a 0.1 μm PTFE membrane with a diameter of 30 mm. The filter was then pasted on a polyethylene plate and

dried under reduced pressure [9]. The filter was subjected to α-spectroscopy using a 450 mm^2 silicon detector and a 1024 ch PC-PHA system.

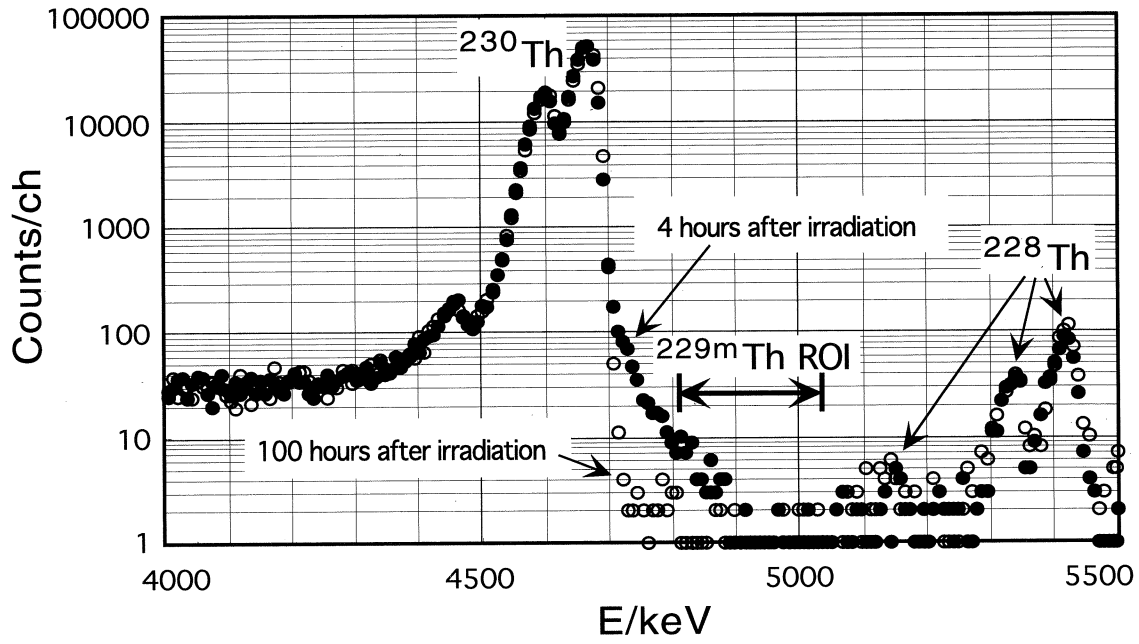

Fig.1. α-spectra of thorium isotopes after 30 MeV bremsstrahlung irradiation on ^{230}Th.

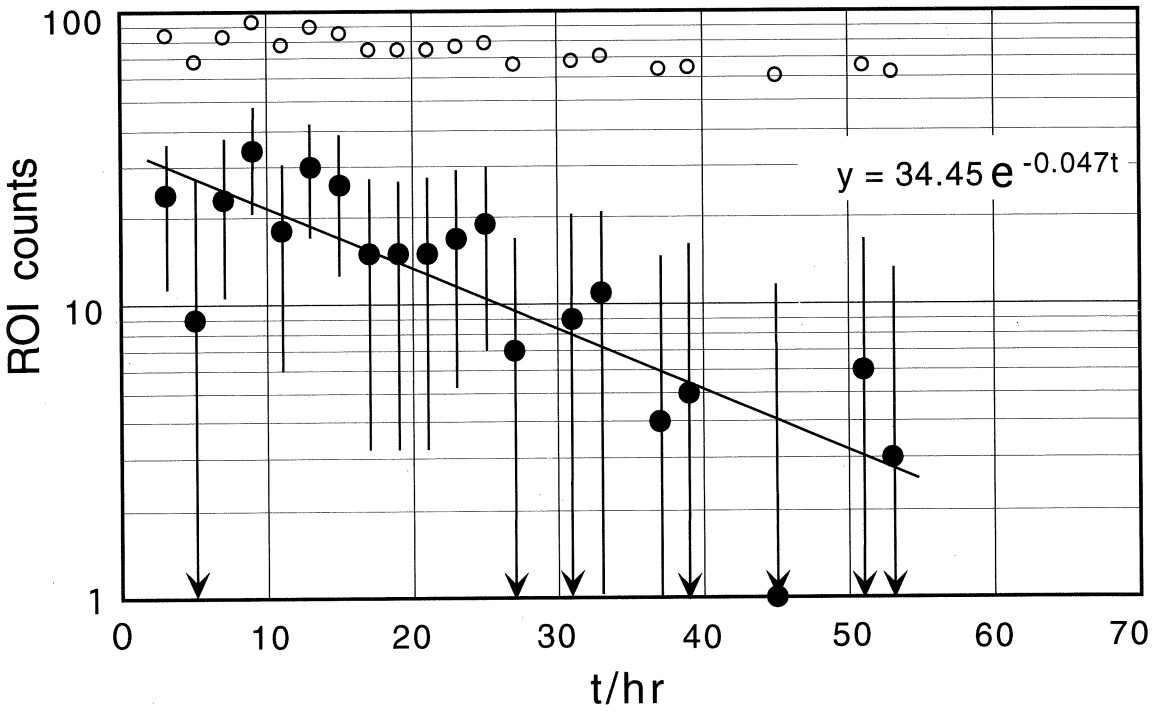

Fig.2. A decay plot of α-counts from 4.83 MeV to 5.03 MeV observed after 22 MeV irradiation.
○ : Total counts, ● : Subtracted plot for a long life component.

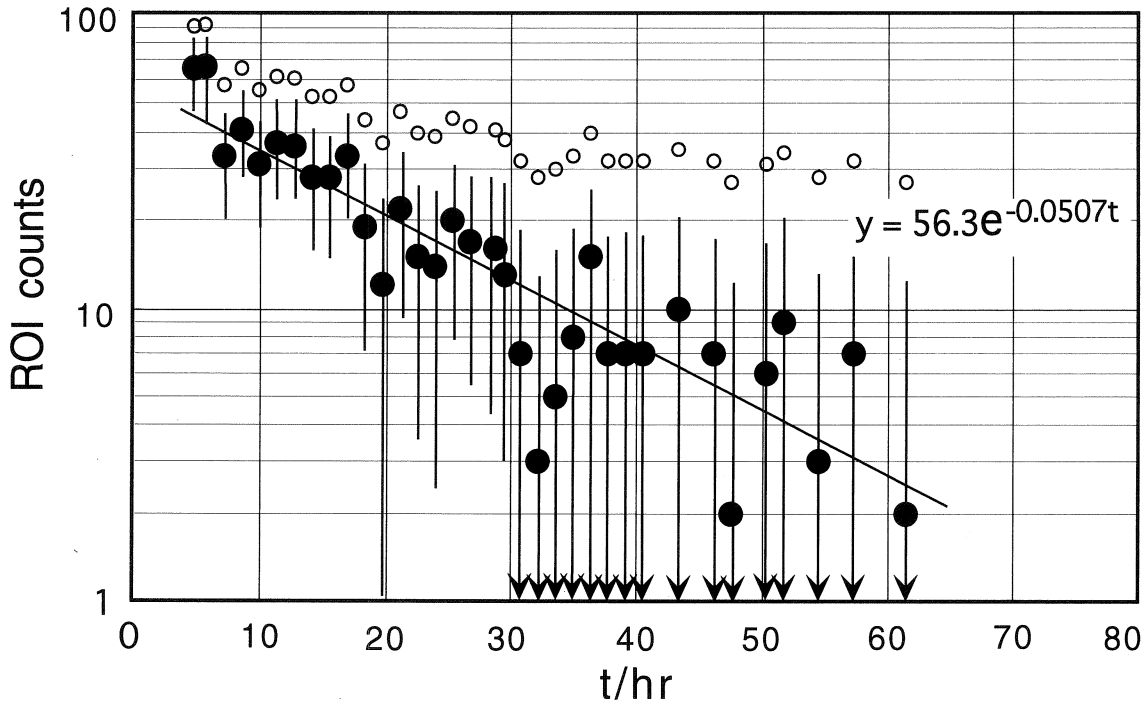

Fig.3. A decay plot of α-counts from 4.83 MeV to 5.03 MeV observed after 30 MeV irradiation.
○ : Total counts, ● : Subtracted plot for a long life component.

§ 3. Results and Discussion

The α-spectrum taken 4 hours after the end of a 30 MeV irradiation was compared to that taken after 100 hours in Fig.1. The decaying α-emitter is observed between the 4.687 MeV peak of ^{230}Th and the α-peaks of the (γ, 2n) product ^{228}Th. The energies of the decaying components are consistent to the expected energy for α-particles from ^{229m}Th, i.e., 4.83 to 5.03 MeV. Some very weak, long lived components were also observed in this same energy region that indicated the production of ground-state ^{229}Th. Because the α-peaks were not clearly defined, probably due to poor counting statistics, a decay plot was made with respect to the total α-counts in the region expected for ^{229m}Th (^{229m}Th ROI counts) as shown in Fig.2 for 22 MeV irradiation and in Fig.3 for 30 MeV irradiation, respectively. As a result, we recognized the production of an α-emitter by its half-life of 16.5 ± 6 hours in the 22 MeV irradiation and that of 13.9 ± 3 hours in the 30 MeV irradiation. At present, we recommend the latter value as the half-life of ^{229m}Th because of better statistics.

Until March 2001, we carried out three times 22 MeV irradiation and twice 30 MeV irradiation and confirmed the reproducibility of these results. We can also make rough estimations of the relative production rates for (γ, n) and (γ, 2n) reactions $\Sigma_{229m}/\Sigma_{228}$ from the observed relative α-activities of ^{229m}Th and ^{228}Th assuming the branching ratio of the α-decay of ^{229m}Th. The results are shown in Table 2. The partial half-life of α-decay of ^{229m}Th was assumed to be 500 y that was consistent to about four α-decay channels with their half-life around 2000 y. The estimated $\Sigma_{229m}/\Sigma_{228}$ values were also consistent to the effective cross sections for (γ, n) and (γ, 2n) reactions multiplied with Shiff-type

spectrum of bremsstrahlung. It should be mentioned that the observed half-life is the longest value for ^{229m}Th, because thorium atoms in trifluoride precipitates are in a 4+ ionic state that has no valence electrons interacting with the thorium nucleus.

Table 2. Relative production rate for ^{229m}Th/^{228}Th from bremsstrahlung irradiation of ^{230}Th.

Irradiating condition	α-activity ratio ^{229m}Th/^{228}Th*	$\Sigma_{229m}/\Sigma_{228}$**
22 MeV, 10 hours	~0.08	~20
30 MeV, 10 hours	0.06	~11

*Ratio at the end of irradiation. **See in text.

Authors are grateful to Profs. Yamana and Ohkubo, Research Reactor Institute of Kyoto University for their helpful discussions.

References

[1] R. G. Burke, P. E. Garrett, Tao Qu, and R. A. Naumann: Phys. Rev. **C42** (1990) R499.

[2] R. G. Helmer and C. W. Reich: Phys. Rev. **C49** (1994) 45.

[3] E. V. Tkalya, A. N. Zherikhin, and V. I. Zhudov: Phys. Rev. **C61** (2000) 064308.

[4] G. M. Irvin and K. H. Kim: Phys. Rev. Lett. **79** (1997) 990.

[5] D. S. Richardson, D. M. Benton, D. E. Evans, J. A. R. Grifithm, and G. Tungate: Phys. Rev. Lett. **80** (1998) 3206.

[6] S. B. Utter, P. Beiersdorfer, A. Barnesw, R. W. Lougheed, J. R. Crespo Lopez-Urrutia, J. A. Becker, and M. S. Weiss: Phys. Rev. Lett. **82** (1999) 505.

[7] R. W. Shaw, J. P. Young, S. P. Cooper, and O. F. Webb: Phys. Rev. Lett. **82** (1999) 1109.

[8] Table of Isotopes 8th edition, edited by R. B. Firestone and V.S. Shirley, (John Wiley & Sons, Inc., New York, 1996), Vol. 2, p 2711.

[9] T. Mitsugashira, M. Hara, Y. Suzuki, M. Watanabe, S. Hirai, Y. Okada and A. Mori: J. Radioanal. Nucl. Chem. **239** (1999) 345.

Study on Photon Activation Analysis of Carbon in Glasses for Fiber Amplifiers by Using the Flow Method for the Rapid Separation of ^{11}C

K.Shikano[1], T.Ohtsuki[2], K.Masumoto[3], A.Mori[1] and M.Shimizu[1]

[1]*NTT Photonics Laboratories, Nippon Telegraph and Telephone Corporation, Ibaraki, 319-1193*
[2]*Laboratory of Nuclear Science, Tohoku University, Mikamine, Taihaku-ku, Sendai, 982-0826*
[3]*Radiation Science Center, High Energy Accelerator Research Organization, Tsukuba, 305-0801*

We have studied nuclear interference from a matrix produced by (γ, n), (γ, 2n), (γ, p) and (n, γ) reactions and a flow method for ^{11}C separation in order to develop an approach for the photon activation analysis of carbon in InF_3-based fluoride, chalcogenide and tellurite glasses for fiber amplifiers. We found that seventeen radionuclides are produced from these glasses and chemical separation is necessary to determine carbon. For the flow method, which involves the fusion of an irradiated sample with an oxidizer, the conversion of ^{11}C into $^{11}CO_2$ and the absorption of ^{11}C in ethanolamine solution, we used a mixture of Pb_3O_4 and B_2O_3 as the oxidizer. We also found that the reaction between ^{19}F(γ, n) and ^{23}Na(γ, αn) in the ethanolamine solution produced ^{18}F contamination with fluoride and chalcogenide glasses and that this flow method can only be applied to tellurite glasses. We confirmed that the chemical yield of the flow method was close to 100 % when determining carbon in standard steel samples by using lithium carbonate as a standard sample. We determined that the carbon concentrations in two kinds of tellurite glass were 8 to 13 and 21 to 28 ppm, respectively.

§ 1. Introduction

Rare-earth element-doped fluoride, chalcogenide and tellurite glasses are expected to be important materials as host glasses for fiber lasers and optical fiber amplifiers [1,2]. It is important to determine the trace amounts of light elements such as carbon and oxygen in these glasses because impurities affect their optical properties.

Charged particle activation analysis (CPAA) is one of the most sensitive, precise and accurate methods for analyzing light elements such as boron, carbon, nitrogen, and oxygen and we have used this technique to determine the light elements in highly pure materials such as rare metals and semiconductor crystals [3-5]. We have also determined the oxygen concentration in Pr^{3+}-doped InF_3-based fluoride and Ga-Na-S (GNS) glasses by charged particle activation analysis using the ^{18}O(p,n) ^{18}F reaction. As a result, we found that the oxygen concentration in fluoride glasses is reduced when chemically produced strontium fluoride is used as a material. Moreover, GNS glass produced in a conventional process contained about 0.1% - 0.2% of oxygen, whereas the oxygen content decreased to 0.04% - 0.08% when we added magnesium to the glass melt as a deoxidizer and this oxygen was related to the optical properties [6].

However, CPAA has a disadvantage in that it requires standardization to correct the difference in stopping power between test and standard samples for accurate determination.

By contrast, it is well-known that carbon, nitrogen, and fluorine can be determined by photon activation analysis (PAA) and that correction, such as the standardization needed for CPAA, is unnecessary with PAA. Therefore, we believe PAA to be useful for the determination of carbon.

However, we recently proposed a flow method for the rapid separation of ^{11}C produced by such nuclear reactions as $^{12}C(\gamma, n)^{11}C$, $^{12}C(^{3}He, \alpha)^{11}C$, $^{10}B(d,n)^{11}C$ [7]. With this technique an irradiated sample is heated by an oxidizer in an O_2 gas flow and ^{11}C in the sample is oxidized into CO_2 and carried to an absorption column by the O_2 gas flow. In the column, $^{11}CO_2$ is adsorbed in a 750 % ethanolamine solution supplied at a rate of 3 cc/min and transferred to the detection part. Then, the radioactivity of ^{11}C in the solution is measured in the form of a radiochromatogram with a coincidence counting system. However, it is difficult to determine chemical yields for ^{11}C with the proposed method and this flow method has not been used to determine carbon by activation analysis.

This paper describes an analytical method for determining carbon in InF_3-based fluoride, chalcogenide and tellurite glasses by using the $^{12}C(\gamma, n)^{11}C$ reaction and the flow method for the chemical separation of ^{11}C. First, we studied the nuclear interference from the matrix elements. Then, we investigated the chemical separation of ^{11}C using the flow method and we attempted to determine the chemical yield in the separation by using standard steel samples. Finally, we determined the carbon in these glasses by a comparison method using lithium carbonate as a standard sample. We compared the results with results estimated by using radiochromatograms obtained from glass and steel samples.

§ 2. Experimental Procedure

2.1 Reagents

We used InF_3-GaF_3-PbF_2-BaF_2-SrF_2-ZnF_2-LaF_3-YF_3 -LiF-NaF glass [InF_3-based glass], Ga-Na-S glass [GNS glass] and a glass prepared by using highly pure TeO_2 [tellurite glass] as analytical samples. We doped these glasses with 1000 ppm of praseodymium. We fabricated the InF_3-based glasses in the same way as described in refs. [6, 8, 9] and prepared the GNS glasses by a melt-quenching method. We fabricated tellurite glasses in the same way as described in ref.[10]. We also analyzed a standard steel sample (JSS1201-1, certified value of 5 ppm) in this experiment to determine chemical yields. We used a mixture of Pb_3O_4 and B_2O_3 as an oxidizer for fusion and oxidation.

We used lithium carbonate as a standard sample and Cu film 5 mm × 5 mm in size and 30 μm thick as a flux monitor.

2.2 Irradiation

The samples and Cu flux monitors were wrapped in aluminum foil (8 μm thick). Bremsstrahlung irradiation was undertaken with the linear electron accelerator of Tohoku University at less than 30 MeV for 20 min at 100 μA. A graphite block was placed between a converter and the samples, and the samples were cooled in a water bath during irradiation to avoid heating the sample.

To remove contamination from the surface of the irradiated samples, we etched the InF_3-based fluoride with 0.4 M $ZrOCl \cdot 8H_2O$ solution and the other glasses with diluted hydrofluoric acid. We

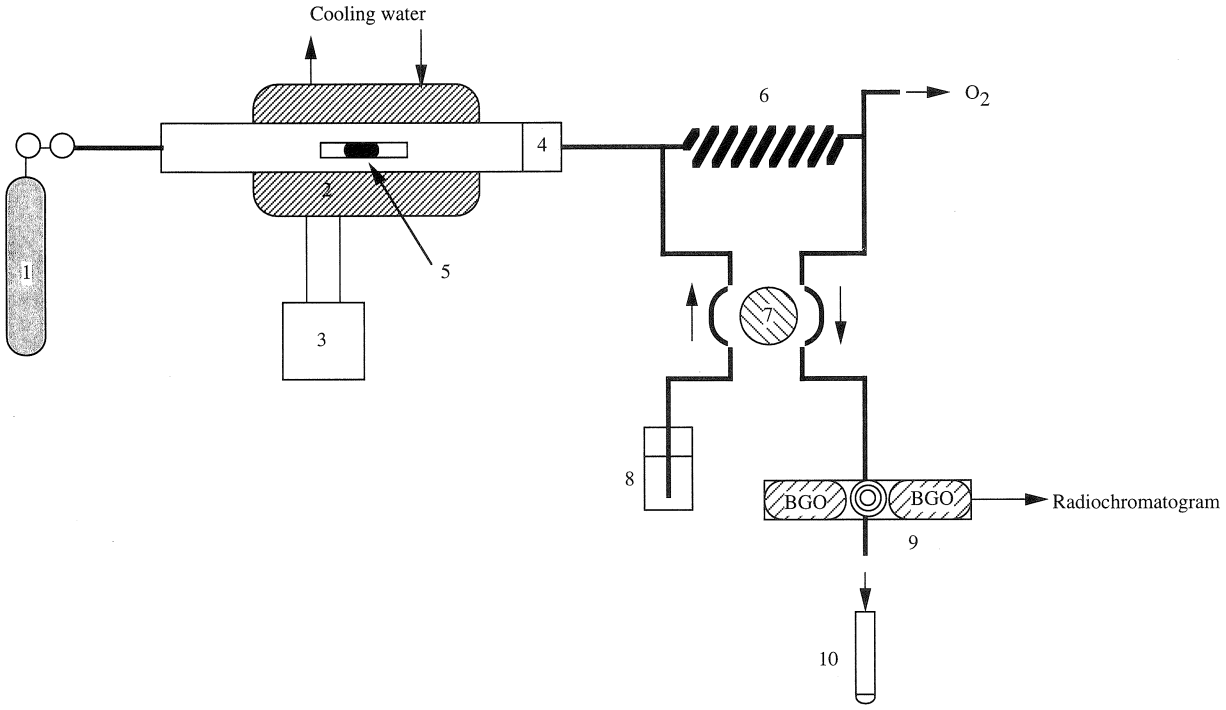

Fig.1. Set-up for separation of ^{11}C and radiochromatography; 1: carrier gas (O_2), 2: infrared heating furnace, 3: controller, 4: quartz wool, 5: sample and oxidizer, 6: adsorption column, 7: pump, 8: 75% ethanolamine solution, 9: coincidence counting system, 10: test tube for collecting ethanolamine.

etched the steel sample with a mixture of hydrofluoric acid and hydrogen peroxide.

2.3 Separation and radioactivity measurement of ^{11}C

Figure 1 shows the flow method set-up for the separation and radiochromatogram measurement of ^{11}C. We mounted the sample in a quartz boat with the oxidizer and then placed the boat in an infrared heating furnace. The sample was heated and fused with an oxidizer in an O_2 gas flow. The ^{11}C in the samples was oxidized to $^{11}CO_2$ in the furnace and transferred to an absorption column with O_2 gas. Then, $^{11}CO_2$ was absorbed in a 75% ethanolamine solution and measured to obtain a radiochromatogram by using a coincidence counting system consisting of a pair of bismuth germanium oxide (BGO) detectors installed downstream of the absorption column. We collected the solution containing the absorbed $^{11}CO_2$ in a test tube and then measured it with the coincidence counting system connected to two NaI(Tl) detectors to obtain decay curves. Irradiated lithium carbonate was dissolved in water and measured in the same way as the ethanolamine collected in the test tube. We analyzed the decay curve with a multiple least-squares computer program.

We also measured the nuclear interference produced from the matrix by the (γ, n) reaction using a Ge detector with a 4096 channel pulse height analyzer. The relative efficiency and FWHM of the Ge detector were 20% and 2.0 keV for a ^{60}Co 1332 keV γ-ray.

2.4 Calculation of carbon concentration

We calculated the carbon concentration (C_x) using Eq.(1).

$$C_x = (A_x/A_s)\,(M_s/W_x)\,k, \qquad (1)$$

where A_x and A_s indicate the radioactivity of ^{11}C at the end of irradiation, M_s is the amount of carbon in

a standard sample, W_x is the weight of the test sample, and k is the relative flux.

§ 3. Results and Discussion

3.1 Nuclear interference

Table 1 shows the nuclear reaction of carbon and radionuclides produced from glasses with photon bombardment. We found that eleven radionuclides (^{63}Zn, ^{68}Ga, ^{70}Ga, ^{85m}Sr, ^{87m}Sr, ^{111}In, ^{112}In, ^{114m}In and ^{116m}In) and four radionuclides (^{67}Ga, ^{68}Ga, ^{70}Ga and ^{72}Ga) were produced by (γ, n), (n, γ) and (γ, 2n) reactions of InF_3-based fluoride and GNS glasses, respectively. ^{127}Te and ^{129}Te were also produced by the (γ, n) reaction of tellurite glasses. Some of these radionuclides were the same positron emitter as ^{11}C produced from carbon. Therefore, we found that the chemical separation of ^{11}C is required for the determination of carbon in these glasses.

Table 1. Nuclear reaction of carbon and nuclear interference produced from the matrix by Bremsstrahlung bombardment.

Nuclear reaction	Half-life	Decay mode	E γ, keV(%)
^{12}C(γ, n) ^{11}C	20.38 m	β^+	511(99.76)
^{64}Zn(γ, n)^{63}Zn	38.1 m	β^+, EC	511(185.6), 669.6(8.4)
^{66}Zn(γ, n)^{65}Zn	244.1 d	EC, β^+	511(2.92), 1115.5(50.8)
^{69}Ga(γ, 2n)^{67}Ga	78.2 h	EC	184.6(22.9)
^{69}Ga(γ, n)^{68}Ga	68.0 m	β^+, EC	511(178.2),1077.4(3.2)
^{71}Ga(γ, n)^{70}Ga	21.1 m	β^-	1039.2(0.7)
^{71}Ga(n, γ)^{72}Ga	14.1 h	β^-	834.0(95.6)
^{86}Sr(γ, n)^{85m}Sr	68.0 m	IT, EC	231.7(85.0)
^{88}Sr(γ, n)^{87m}Sr	2.806 h	IT, EC	388.4(82.3)
^{113}In(γ, 2n)^{111}In	2.83 d	EC	245.4(94.0)
^{113}In(γ, n)^{112}In	14.4 m	$\beta^\pm$, EC	511(42.8), 618.2(5.3)
^{115}In(γ, n)^{114m}In	49.5 d	IT, EC	190.2(18.4)
^{115}In(n, γ)^{116m}In	54.15 m	β^-	1293.5(84.4)
^{122}Te(γ, n)^{121}Te	16.78 d	EC	573.1(80.3)
^{128}Te(γ, n)^{127}Te	9.35 h	β^-	417.9(1.0)
^{130}Te(γ, n)^{129}Te	69.6 m	β^-	459.6(7.4)
^{130}Te(γ, p)^{129}Sb	4.41 h	β^-	812.8(43.5)
^{204}Pb(γ, n)^{203}Sb	52.0 h	EC	279.2(80.1)

3.2 Chemical separation of ^{11}C

To enable us to fuse glass samples rapidly and oxidize ^{11}C to $^{11}CO_2$ completely, we studied the fusion of these glasses using three kinds of oxidizers (a mixture of Pb_3O_4 and B_2O_3, CuO, and NaCl). As a result, we selected the mixture of Pb_3O_4 and B_2O_3 as the oxidizer because the ^{11}C yield in the radiochromatogram was the highest and ethanolamine was uncontaminated by other nuclides. In contrast, ^{63}Zn and ^{68}Ga was detected in the solution because their chlorides became volatile when NaCl was used.

Figure 2 shows radiochromatograms we obtained from InF_3-based fluoride, GNS, and tellurite glasses that were not chemically etched after irradiation. As shown in the figure, we found that the greatest amount of radionuclides such as ^{11}C or other positron emitters were produced by fluoride and the least amount by tellurite. Figure 3 shows the decay curve of a 511 keV γ-ray obtained from the

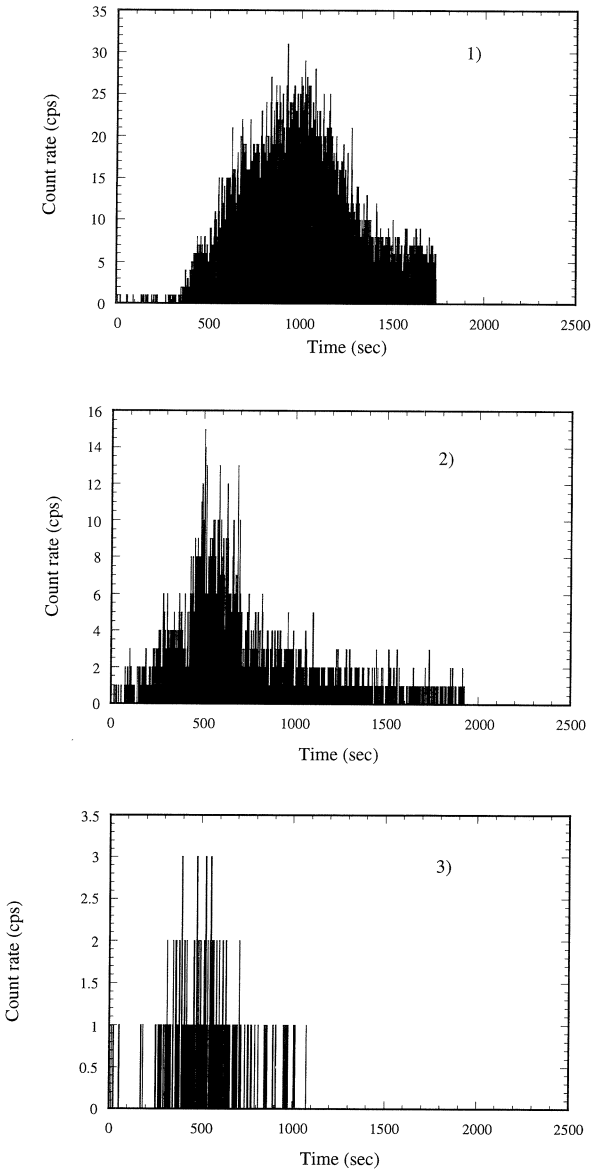

Fig.2. Radiochromatograms obtained from three glasses;
1) InF_3-based fluoride glass, 2) GNS glass, 3) tellurite glass.

absorption solution collected in the test tube. As shown in the figure, we found that there are long half-life nuclides in the decay curves of the InF_3-based and GNS glasses. Our analysis of their half-life showed these nuclides to be ^{18}F. We believe that ^{18}F is produced from the fluoride and GNS glasses by $^{19}F(\gamma, n)^{18}F$ and $^{23}Na(\gamma, \alpha n)^{18}F$ reactions and volatilized. It then contaminates the ethanolamine solution used for absorbing $^{11}CO_2$. Therefore, we concluded that it is difficult to employ the chemical separation of ^{11}C by the flow method for the determination of carbon in fluoride and GNS glasses because of large radioactivity of ^{18}F compared with that of ^{11}C after etching. However, this method can be used to determine carbon in tellurite glasses.

3.3 Determination of chemical yield for ^{11}C

Steel samples were fused in the same way described in ref.[7]. Figure 4 shows the radiochromatogram and decay curve of the steel sample. We found that only ^{11}C can be separated by the flow method from this decay curve. Table 2 shows the analytical results for carbon in steel. As

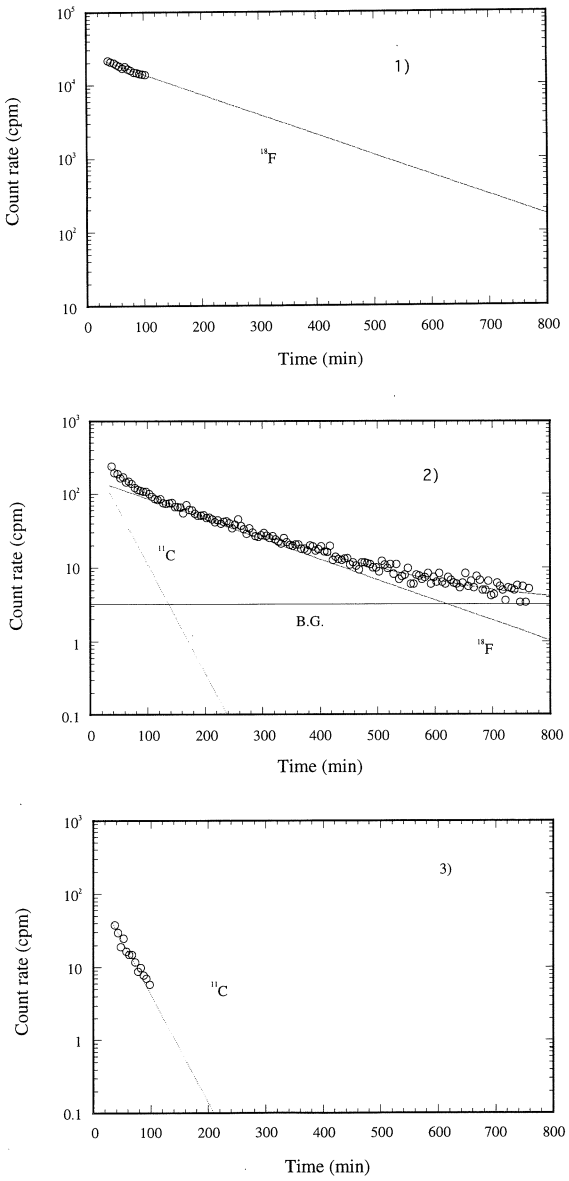

Fig.3. Decay curves of 511 keV γ -ray obtained from three glasses;
1) InF_3-based fluoride glass, 2) GNS glass, 3) tellurite glass.

shown in the table, the carbon concentration is 5.0 $\pm$ 1.0 ppm and in good agreement with the certified value but the relative deviation is large at 20%. It seems that ^{11}C in the steel sample is converted to $^{11}CO_2$ and all the $^{11}CO_2$ is completely absorbed in the ethanolamine solution, although the concentration is widely dispersed. Therefore, we concluded that the chemical yield with the flow method is close to 100%.

3.4 Determination of carbon in tellurite glasses

Table 2 shows analytical results for carbon in two kinds of tellurite glass. As shown in the table, their carbon concentrations were respectively 8 to 13 and 21 to 28 ppm and the relative deviation was 14 to 24% in both samples. Table 2 also shows the carbon concentration in the tellurite glasses calculated by using their radiochromatograms and the certified carbon concentration (5 ppm) in the steel samples. The carbon concentrations were 7 to 14 and 22 to 33 ppm in the two kinds of tellurite glass (Tellurite-1, 2). The concentration in Tellurite-1 is in good agreement with the above values but that in Tellurite-2 is a little larger than earlier values. Therefore, we found that the radioactivity of ^{11}C measured from

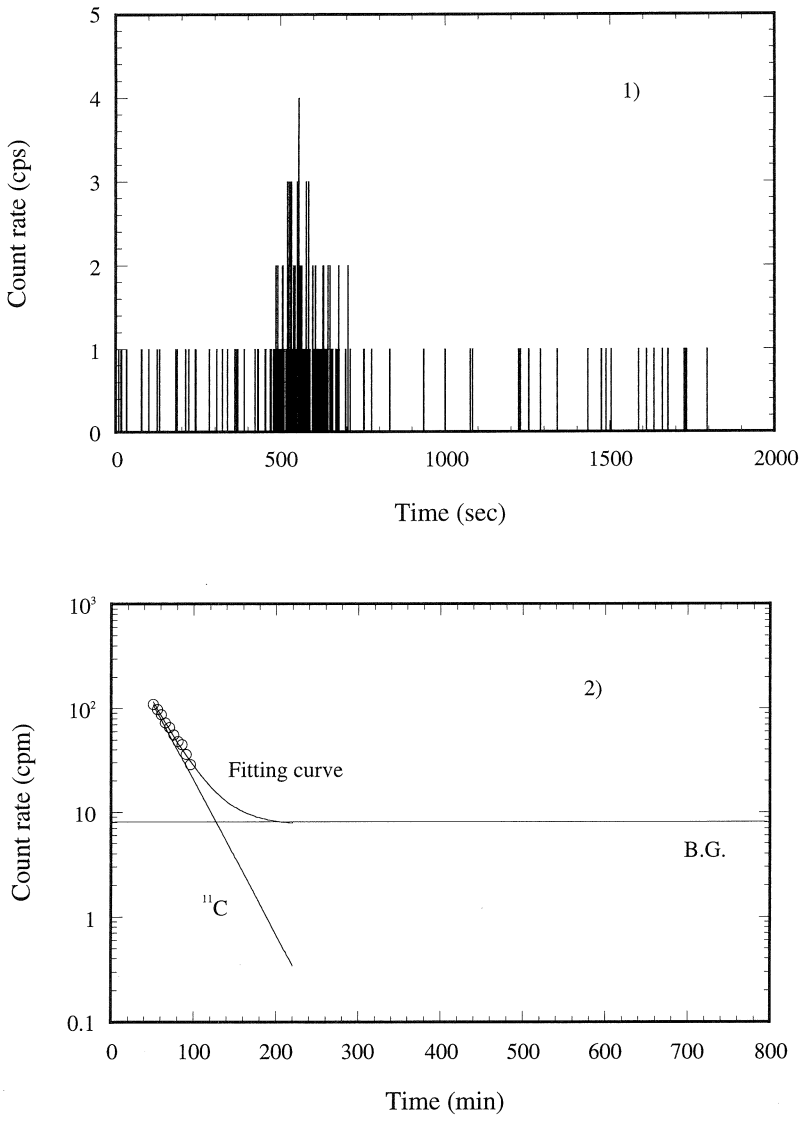

Fig.4. Radiochromatogram 1) and decay curve 2) of steel sample (JSS 1201-1).

Table 2. Analytical results for carbon in steel sample and tellurite glasses.

Sample	Concentration* (ppm)	Concentration** (ppm)
Steel JSS1201-1-1	5	
-2	6	
-3	4	
Average value	5.0±1.0	
Tellurite-1-1	8	7
-2	13	14
Tellurite-2-1	21	22
-2	28	33

* Calculation by using lithium carbonate as a standard sample.
**Calculation by using steel (JSS1201-1) as a standard sample.

radiochromatograms and decay curves can be used for the determination of carbon, and the precision and accuracy of this analytical method can be improved when there is no contamination in the radiochromatogram.

In conclusion, our proposed analytical method is a simple, rapid and accurate way to determine the carbon in these glasses. This is because we can confirm the chemical condition using radiochromatograms and detect any contamination by other positron emitted nuclides such as ^{18}F from the decay curve. Moreover, we can exactly correct the radioactivity of ^{11}C by analyzing the half-life of the decay curve.

References

[1] Y. Nishida, T. Kanamori, T. Sakamoto, Y. Ohishi, S. Sudo : J. Non-Crystalline Solids, **221** (1997) 238.

[2] K. Fujiura, T. Kanamori, S. Sudo : in S. Sudo (Ed.), *Optical fiber amplifiers*, Artec House, Inc., 1997, p.200.

[3] K. Shikano, H. Yonezawa, T. Shigematsu : J. Radioanal Nucl. Chem. **167** (1993) 81.

[4] K. Shikano, H. Yonezawa, T. Shigematsu : J. Radioanal Nucl.Chem. **173** (1993) 409.

[5] T. Shigematsu, K. Shikano, H. Yonezawa : Bunseki Kagaku **48** (1999) 823.

[6] K. Shikano, Y. Nishida, K. Kobayashi, T. Kanamori, M. Shimizu, K. Masumoto, T. Ohtsuki : J.Radioanal Nucl.Chem., to be submitted.

[7] K. Masumoto, T. Ohtsuki, K. Shikano, H. Itoh : J. Nucl. Radiochem. Sci., Vol.**1** Supplement Oct.1999, " *The 43rd Symp. Radiochemistry, Abstract of Paper*", p.82.

[8] T. Kanamori, Y. Terunuma, Y. Nishida, K. Hoshino, K. Nakagawa, Y. Ohishi, S. Sudo : J. Non-Crystalline Solids, **213&214** (1997) 121.

[9] Y. Nishida, Y. Ohishi, T. Kanamori, Y. Terunuma, K. Kobayashi, S. Sudo : *Tech. Dig. of ECOC '93, Montreux, 1993*, TuC3.1

[10] A. Mori, K. Kobayashi, M. Yamada, T. Kanamori, K. Oikawa, Y. Nishida, Y. Ohishi : Electron Lett. **34** (1998) 997.

Specific Recoil Features of Central Metal Atoms of Zinc and Cadmium in the Solid System of Water-Soluble Metalloporphyrin Ion Associates

H. Shoji*

Department of Chemistry, University of Tsukuba, Tsukuba, Ibaraki 305-8571

Water-soluble metalloporphyrin ion associates with central metal atoms of zinc and/or cadmium were subjected to bremsstrahlung and thermal neutron irradiation under cooling. After the bombardment samples were treated in wet chemical separation procedures using ion exchangers. Radionuclides of copper, zinc and cadmium preferentially substituted cadmium central atoms in the Cd-complex side.

§ 1. Introduction

Generally, in the study of recoil chemistry in the solid phase, bi-component systems sometimes show us the hidden predominant factor, especially the contribution of the possible individual elementary reaction process to the over-all result in the form of numerical reaction probability. As a bi-component system isomorphous mixed crystals were used in many cases, where components of isomorphous metal complexes such as metal phthalocyanines, metallocenes, hexahalogenometallates and so on were chemically combined in various mole-ratios. As for these series of mixed crystals with different compositions, it is one of great merits to obtain, by extrapolating, the tendency in the situation of infinite dilution of each component. In these cases, however, almost all isomorphous components used for mixed crystals had very similar crystalline structures to each other. Therefore their X-ray powder diffraction patterns were also much too close to prove that mixed crystals with microscopic homogeneity, "true solid solutions", were really produced. It was extremely difficult to prepare statistically homogeneous genuine mixed crystals even from the microscopic point of view.

So our interest shifted to another bi-component system of "water-soluble metalloporphyrin ion associates", which were obtained by our group rather by chance. This kind of large ion associates was expected to be statistically more homogeneous because of the necessity of electrical neutralization of the component counter ions, though the mole ratio of the component complex ions could not be changed from (1:1). So far our group investigated the recoil features in this kind of systems of various combinations of central metal atoms and ligands, for example [M(TMPyP)] [M′(TCPP)] (M, M′= Cu, Zn), [M(TMPyP)] [M′(TPPS)] (M, M′= Cu, Zn and Co, Cu) where H_2TMPyP = tetrakis (4-N-methylpyridyl) porphine, H_2TCPP = tetra (p-carboxyphenyl) porphine, and H_2TPPS = tetra (p-sulfophenyl) porphine [1-4]. This time our results on specific recoil tendencies of central atoms in the system of [M(TMPyP)] [M′(TPPS)] (M, M′= Zn, Cd) are reported here, on which only the preliminary

*Present address: 3-46-3 Utsukushigaoka, Aoba-ku, Yokohama 225-0002

results were published [3, 5]. On the water-soluble metalloporphyrin ion associate systems investigated, all our previous data showed that the final fate of the recoil was determined in the very late stage of chemical reaction processes after losing its high recoil energy and/or high electric charge. However, some experimental confirmation was thought to be necessary whether the elastic billiard-ball-like dynamical process might give any contribution to the over-all final result or not. So the homologous elements with large mass difference, Zn-Cd were combined as the central metal atom in the system of [M(TMPyP)] [M′(TPPS)].

Figure 1 shows the structural formula of the water-soluble metalloporphyrin ion associate used this time.

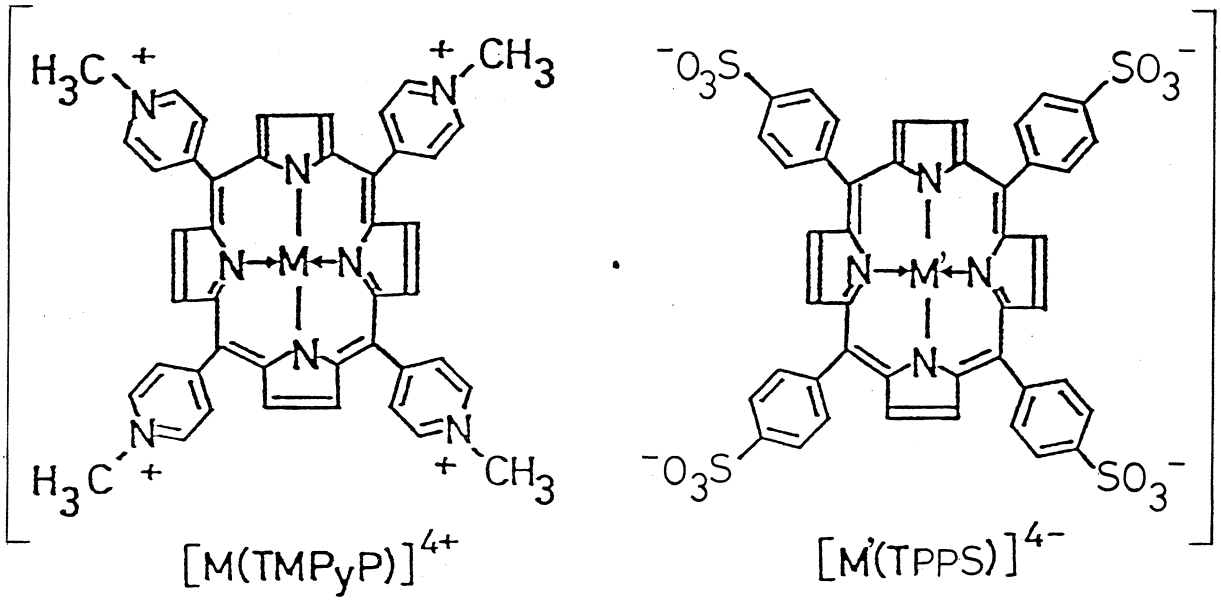

Fig.1. Structural formula of water-soluble metalloporphyrin ion associates used. [M(TMPyP)] [M′(TPPS)] (M, M′= Zn, Cd).

§ 2. Experimental

For the preparation of ion associate samples, first the component complex ions were synthesized, respectively. As a metal-free ligand is now commercially available, which was developed as the highly sensitive reagent for the spectrophotometric determination of trace amount of heavy metal ions, it was mixed with small excess of metal salt corresponding to a central metal in an appropriate solvent and the mixture was refluxed for a few hours or so. The metal porphyrin was obtained in the form of precipitate, which was purified by reprecipitation. Two aqueous solutions of each component complex ion were mixed in (1 : 1) mole ratio and the solution was left aside for overnight or longer. Then the complex ion associate formed as the amorphous or very fine crystalline precipitate. It was purified by repeated precipitation using the same aqueous medium as that in the dissolution of the irradiated sample. The samples were checked by elemental analysis and spectrophotometric measurement.

The purified samples were subjected to two kinds of irradiation. One was bremsstrahlung irradiation and the other was thermal neutron irradiation. The bremsstrahlung irradiation was done in the 300 MeV Electron Linear Accelerator in Tohoku University, Sendai, Japan. The irradiation was

carried out using Pt-converter under the following conditions: max energy of photons; 50 MeV, Current; 100～150 μA, irradiation temp; < −130℃, irradiation time; 8～10 hours. Unconverted electrons were removed by a sweep magnet. The thermal neutron irradiation was done in TRIGA MARK II Reactor of Rikkyo University, Yokosuka, Japan. The samples were irradiated in the in-core tube at −78℃ for 2 hours, where the thermal neutron flux was 1.5×10^{12} n/cm^2・sec.

Figure 2 represents the chemical separation procedures for the irradiated sample.

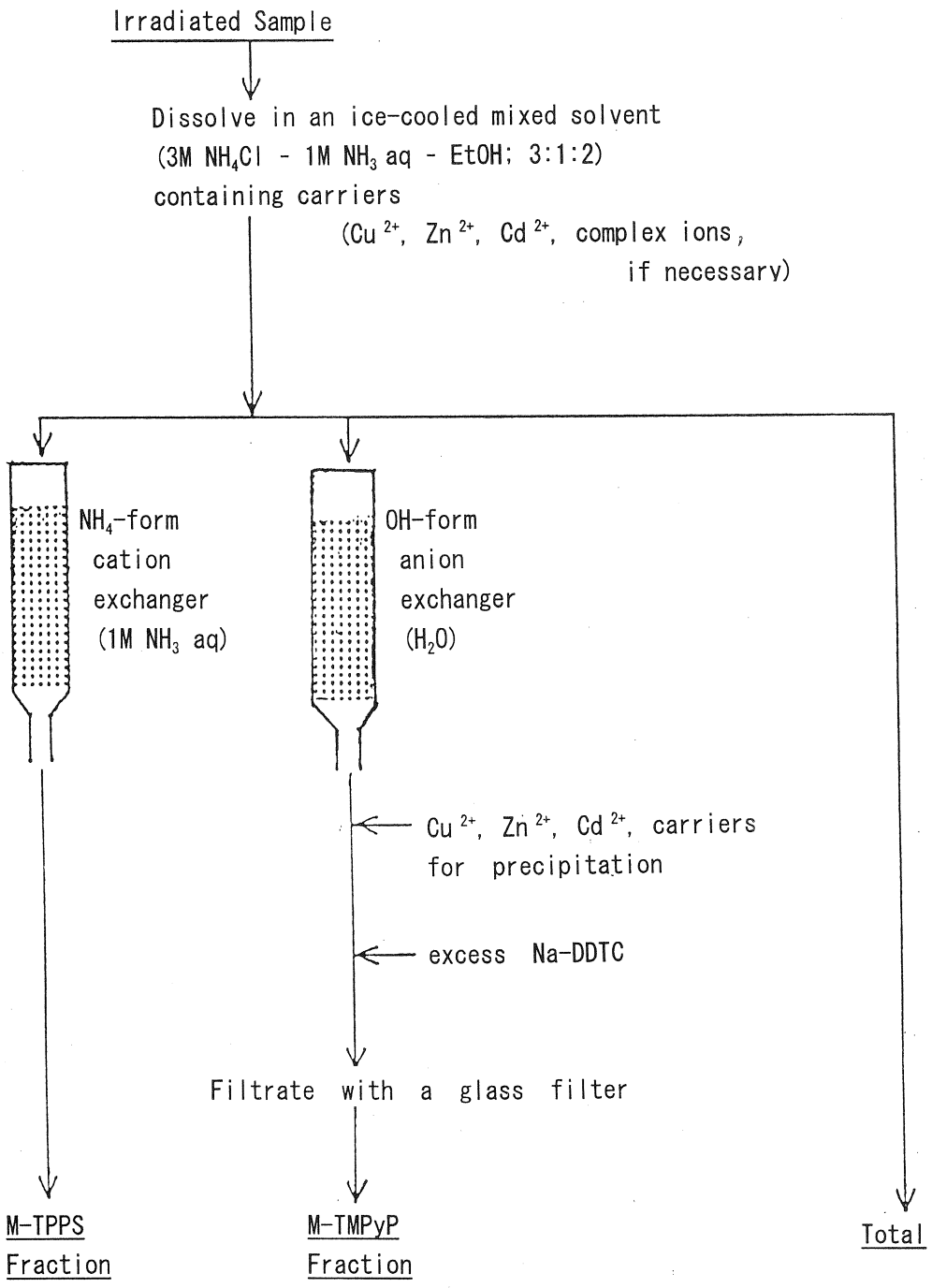

Fig.2. Chemical separation procedures.

Irradiated samples were dissolved in ice-cooled mixed solvents of 3M NH_4Cl, 1M ammonia water and ethanol (the volume ratio, 3:1:2) containing the necessary carriers (Cu^{2+}, Zn^{2+}, Cd^{2+}, Cu-complexes ions, if necessary, and M-complex ions whose central metal atoms were reverse to the target sample in the case of different central metal atoms in the associate). An aliquot of a sample solution was passed through cation and anion exchanger columns. In the effluent from the anion exchanger column, the coexisting bare metal ions were removed in a form of the precipitate of metal carbamates by adding carriers for precipitation and sodium diethyldithiocarbamate. Three counting samples were prepared from one irradiated sample.

The γ-spectra of these samples were measured using a Ge (Li) or HPGe detector and they were analysed by the connected computer system.

§ 3. Results and Discussion

The nuclear reactions concerned in the both irradiation are listed below.

Bremsstrahlung Irradiation Case:

$^{68}Zn(\gamma, p)^{67}Cu$

$^{66}Zn(\gamma, n)^{65}Zn$

$^{70}Zn(\gamma, n)^{69m}Zn$

$^{116}Cd(\gamma, n)^{115}Cd$

Thermal Neutron Irradiation Case:

$^{64}Zn(n, \gamma)^{65}Zn$

$^{68}Zn(n, \gamma)^{69m}Zn$

$^{114}Cd(n, \gamma)^{115}Cd$

In the recoil process in the solid system of water-soluble metalloporphyrin ion associates, which accompanies nuclear reactions such as photonuclear reactions and thermal neutron capture listed above, some part of the radionuclide formed is found to be located at the center of the component complex, making a labelled complex. The complex yield of the nuclide in the complex fraction depends on many factors, such as the combination of central metals and ligands in the complex ion associate, nuclear reactions, irradiation temperatures and so on.

Table 1 represents the complex yields obtained experimentally, where fluctuations mean the statistical standard deviation in the repeated experiments. It shows that all the recoiling nuclides concerned (*M, including ^{115}Cd) were preferentially stabilized in the Cd-complex side, not in the Zn-complex side, in all the cases in the both irradiation, which indicates that cadmium central metal atoms were very easy to be substituted by the recoilling *M because of its lower stability due to its much larger ion radius than those of the other metals. The complex yields of ^{67}Cu and *Zn in the Cd-complex side directly show the substitution reaction probability of cadmium central atoms by the *M, where those of ^{67}Cu were much higher than those of *Zn, which implies the larger difference of stability between the Cu- and Cd-complex than between the Zn- and Cd-complex. All the *Zn complex yields in Cd (TPPS) side showed almost similar numerical values and those in Cd (TMPyP) side had the almost similar tendency with one exception (^{65}Zn complex yield in the Cd (TMPyP) side: as low as 6%), which

Table 1. Complex Yields (%) in [M(TMPyP)] [M'(TPPS)] (M, M' = Zn, Cd)

Sample Fraction	[Zn (TMPyP)] M (TMPyP)	[Cd (TPPS)] M (TPPS)	[Cd (TMPyP)] M (TMPyP)	[Zn (TPPS)] M (TPPS)
^{67}Cu	7±2	80±2	29±5	14±3
	——	——	——	——
^{65}Zn	2.1±1.7	17±3	6±3	2±1
	1.13±0.07	16.8±0.5	20.8±0.9	3.0±0.4
^{69m}Zn	1.9±0.9	22±3	13±2	2.0±1.5
	3.50±0.06	16.8±0.2	21.9±0.3	6.5±0.1
^{115}Cd	0.10±0.04	10.1±0.4	2.5±0.2	0.8±0.1
	0.07±0.01	11.32±0.08	4.13±0.04	0.83±0.02

Sample Fraction	[Zn (TMPyP)] M (TMPyP)	[Zn (TPPS)] M (TPPS)	[Cd (TMPyP)] M (TMPyP)	[Cd (TPPS)] M (TPPS)
^{67}Cu	20±2	37±1	——	——
	——	——	——	——
^{65}Zn	2.0±0.2	3.5±0.8	——	——
	2.4±0.9	6±3	——	——
^{69m}Zn	1.9±0.5	5±1	——	——
	7±2	14±5	——	——
^{115}Cd	——	——	4±2	5±2
	——	——	5±4	9±3

Upper value: Bremsstrahlung irradiation.
Lower value: Thermal neutron irradiation.

also implies that the predominant stage in determining the final fate of *Zn was the very late chemical one and that it was independent of the initial recoil energy or the kind of nuclear reactions. Although the rather high complex yields of ^{67}Cu in the sample of [Zn(TMPyP)] [Zn(TPPS)] are thought to be the combined result through the primary retention (the complex yield of the nuclide concerned without bond rupture and in very prompt recombination to the original site) and the substitution of stable zinc central atoms by ^{67}Cu recoils, numerically they have to express the latter substitution reaction probability, considering the large initial recoil energy (in 100 keV order) in the photonuclear reaction which only leads to ~0% primary retention. The complex yield of ^{67}Cu, as a whole, implies the higher affinity of *Cu with a TPPS ligand than with a TMPyP ligand. All the retention (the complex yield of the nuclide formed in the same chemical form as the initial target complex) is the combined result of the primary retention and the reaction retention (the retention by the substitution of the central atoms of the same metal as M by *M) and each retention value (probability) can be theoretically obtained separately by solving simultaneous equations formed using complex yields in both kinds of associates of the same and the different central metal atoms. However, no meaningful chemically consistent numerical reaction probabilities were obtained from the calculations, probably because the surrounding atmosphere of *M was different in the associate of different central metal atoms and of same central metal atoms. Comparing retention values of *Zn (that is, complex yields of *Zn in Zn-complex sides) in the case of thermal neutron irradiation, the retention of ^{69m}Zn was always higher than that of ^{65}Zn, which indicates the clear effect of the difference of average initial recoil energy between ^{65}Zn and ^{69m}Zn (446 eV and 166 eV, respectively [6]). In this initial recoil energy range of the order of 100

eV primary retention must depend on the initial recoil energy [7], and the higher initial recoil energy is, the less primary retention is.

As the expression of the stability of metalloporphyrins, two criteria were proposed. One is called "stability class" which was based on the necessary strength of the acid for demetallization of the complex [8, 9] and the other is named "stability index" which was derived from the theoretical calculation using the Pauling's electronegativity, the effective ion radius and the charge of the metal ion [10]. Although at a few point these two criteria show inconsistency, they are consistent with each other in almost all the cases. According to the former criterion, the stability order of the metalloporphyrins concerned is as follows; $Cu^{2+} > Zn^{2+} > Cd^{2+}$. The latter "stability index" shows the general stability order of metalloporphyrins whose central metal is divalent one as in the following:

$$Pd > Ni > Cu > Pt > Co > Fe > Zn > Sn > Pb \approx Hg > Mn > Mg > Cd \gg Ca > Sr > Ba$$

where the Cd-complex is located at far weaker position. These stability orders agree with the strong substitution tendency of Cd by *Cu, *Zn and *Cd in Cd-complex side in the system of [M(TMPyP)] [M'(TPPS)] (M, M' = Zn, Cd).

Although the information of the structure of each ion associate is essential for further discussion, unfortunately the degree of crystallization of this kind of ion associates has been very poor in the sample preparation yet. The X-ray powder diffraction pattern of the purified associate sample showed that the majority part of samples was in the amorphous state mixed with very fine crystals.

The elastic dynamical process can be excluded from the important factors for the final result, considering the present data without any mass difference effects.

The author expresses his hearty thanks to Professor Tsutomu Ohtsuki and all the members of LINAC machine group of this Institute for their great efforts in bremsstrahlung irradiation. The author is also very grateful to Professor Tsutomu Sekine of Department of Chemistry, Graduate School of Science, Tohoku University for his very valuable and kind cooperation. The author is also very thankful to Emeritus Professor Kenji Tomura of Rikkyo University and all the members of Institute for Atomic Energy, Rikkyo University for their very kind cooperation in thermal neutron irradiation.

References

[1] K. Ogawa, H. Shoji and N. Ikeda: Res. Rep. of Lab. Nucl. Sci., Tohoku Univ. **19** (1986) 63.

[2] K. Ogawa, H. Shoji and N. Ikeda: *Proc. 13th Int. Hot Atom Chemistry Symp. Mt. Fuji, 1987*, p. 22.

[3] H. Shoji: Res. Rep. of Lab. Nucl. Sci., Tohoku Univ. **29** (1996) 57.

[4] H. Shoji: J. Radioanal. Nucl. Chem. **239** (1999) 191.

[5] H. Shoji: Res. Rep. of Lab. Nucl. Sci., Tohoku Univ. **25** (1992) 59.

[6] Y. Oki: Thesis, Univ. Tsukuba, 1988.

[7] M. H. Yang, H. Kudo and K. Yoshihara: Radiochim. Acta **15** (1971) 17.

[8] J. W. Buchler, L. Puppe, K. Rohbock and H. H. Schneehagee: Ann. N. Y. Acad. Sci. **206** (1973) 116.

[9] J. W. Buchler: *Habilitationsschrift* (Technische Hochshule, Aachen, 1971).

[10] K. M. Smith: *Porphyrins and Metalloporphyrins* (Elsevier Scientific Publishing Co., 1975), p. 196.

水生無セキツイ動物軟体部の光量子放射化分析

福島美智子，玉手英利

石巻専修大学理工学部（986-8580　石巻市南境新水戸１番地）

Photon Activation Analysis of Soft Tissues of Marine Invertebrates

M. Fukushima and H. Tamate

Ishinomaki Senshu University Faculty of Sciences and Engineering
Shinmito 1, Minamisakai, Ishinomaki 986-8580

We have determined levels of elements in soft tissues of 23 species of marine invertebrates by photon activation analysis and atomic absorption spectrometry. Concentration levels of Mg and Rb were almost same for all samples determined. On the contrary, relatively high concentration of elements were observed for Ni in mid-gut gonads of ear shells, As in gills, hepatopancreas, and muscles of several species of Crustaceans.

§１．序

地球環境のひとつの要素である海洋やその底質を金属元素濃度に関して評価する場合に，マクロ成分であるNa, Mg, Cl, Brなどは多くの分析法にとって妨害になり，目的金属元素の分離濃縮を併用する必要がある。また，特に海水中の金属元素濃度は非常に低いため，正確な分析が非常に困難である。一方，海洋に生息する多くの無セキツイ動物はその体内に金属元素を特異的に濃縮することが知られている。さらにそれら元素の濃縮は元素によっては10^5倍のオーダーにもおよぶため，多くの金属元素を正確に定量することが可能である。そこで，本研究では数種類の無セキツイ動物の正常値を得るため，金属元素で汚染されていないと思われる海域で捕獲された試料中の元素濃度を分析した。さらに，それらの正常値が地質学的に異なる環境をもつ湾内の海水や底質の影響をうけるかどうかを知るため，同一種について，異なった海域で捕獲されたものについて分析した。

元素の分析には主に光量子放射化分析法（PAA）を用いた。放射化分析法は，元素の存在化学形に無関係に定量でき，しかも多元素同時定量が可能であるという利点を有する。本研究ではPAAにより生物試料中のAs, Br, Ca, Cr, Cu, Fe, I, Mg, Mn, Mo, Na, Ni, Pb, Rb, Sn, Sr, Znの17元素の濃度を得ることができた。また，数種類の生物試料については，極めて一般的な分析法であるフレーム原子吸光光度法（FAAS）で数種類の元素の分析を行い，得られた結果について放射化分析法の結果と比較した。

§2. 実　　験

2.1 分析試料

分析試料を第1表に示す。( ) 内の数字はこれまで分析値を得た個体数を示す。市場で購入した一部を除き，分析試料には海から捕獲された後に洗浄や殺菌処理などの人工的な処置を施される前に，生きた状態で入手したものを用いた。また，それら分析試料が捕獲された生息地を第1図に示す。これら試料の処理法は以前の報告［1，2］に記述したものと同様であるが，水道水および蒸留水で軽く洗浄後にペーパータオルで余分な水分を除いた。殻を除いて，軟体部全部か，あるいは部位ごとに分類したのちセラミック製のナイフかハサミで細断し，凍結乾燥した。得られた乾燥試料をミルで粉末にしたのちに200 mesh のステンレス製ふるいでふるいわけた。

第1表　分析した生物試料。

生　物　種		生息地	部　　位
＜貝　　類＞	アワビ	瀬棚	中腸腺 (3)
		雄勝	中腸腺 (15)，筋肉 (4)
		相馬	中腸腺 (4)
		佐渡	中腸腺 (5)
		輪島	中腸腺 (5)
	マガキ	厚岸	軟体部 (4)
		雄勝	軟体部 (10)
		広島	軟体部 (4)
	イワガキ	佐渡	軟体部 (4)
	ホタテガイ	雄勝	閉殻筋 (4)
	アオヤギ	雄勝	軟体部 (3)
	アサリ	東名浜	軟体部 (4)
	バカガイ	雄勝	軟体部 (12)
	ムラサキイガイ	雄勝	軟体部 (3)
	ホッキガイ	山元	閉殻筋 (1)，エラ (1)，外套膜 (1)，臓器 (1)
＜棘皮動物＞	ウニ	雄勝	生殖腺 (20)
		女川	生殖腺 (8)
＜原腸動物＞	ホヤ	雄勝	筋肉 (20)
＜頭 足 類＞	スルメイカ	雄勝	墨汁腺 (4)
＜甲 殻 類＞	毛ガニ	網走	頭胸部筋 (3)，エラ (3)
	ガザミ	男鹿	頭胸部筋 (7)，エラ (4)
	ズワイガニ	佐渡	頭胸部筋 (3)，エラ (3)
	シャコエビ	雄勝	頭胸部 (5)，腹部筋 (5)
	イセエビ	鳥羽	腹部筋 (4)，エラ (4)
		奄美	腹部筋 (4)，エラ (4)，肝すい腺 (4)
	モンガニ	奄美	甲羅内皮 (1)，前肢筋 (1)，エラ (1)，肝すい腺 (1)
	セミエビ	奄美	筋表面 (3)，腹部筋 (3)，エラ (3)，肝すい腺 (3)，精巣 (2)
	ゾウリエビ	奄美	筋表面 (2)，腹部筋 (4)，エラ (4)，肝すい腺 (4)，精巣 (2)
	アサヒガニ	奄美	頭胸部筋 (4)，エラ (4)，肝すい腺 (4)，精巣 (1)
	ノコギリガザミ	奄美	頭胸部筋 (1)，エラ (1)，精巣 (1)
	オオカイカムリ	奄美	エラ (2)

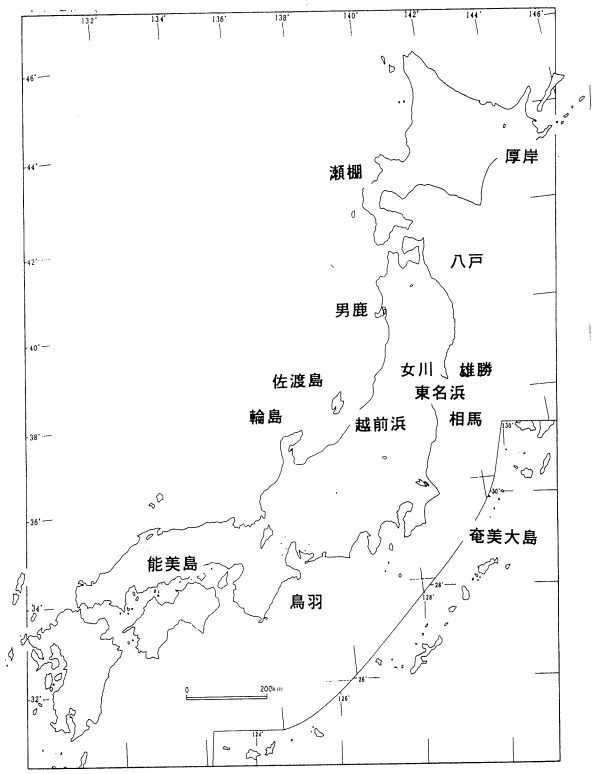

第１図　生物試料の捕獲地点。

2.2　比較標準試料

元素の定量のために市販されている標準物質のなかから NIST SRM-1566a Oyster Tissue, SRM-1577b Bovine Liver（USA）, NRCC TORT-1 Lobster（Canada）の３種類を用いた。また，定量目的元素の既知量を含むアクリルアミドゲルを作成し，凍結乾燥後ミルで粉末にしたものを用いた。アクリルアミドゲルは以下のように作成した。すなわち，200mL 凍結乾燥用容器に30％アクリルアミド水溶液20mL，pH8 の緩衝溶液15mL，0.1 M EDTA 水溶液 5 mL，金属標準溶液適量，N，N，N′，N′-テトラメチレンジアミン３－5mL，25％過硫酸アンモニウム0.5mLを加えて生成したゲルをテフロン製スパーテルで細かく砕き，凍結乾燥した。

2.3　元素の定量法

2.3.1　PAA

上記2.1で作成した粉末試料100-300mg を高純度アルミニウム箔で包み，直径10 mm 厚さ 2－3 mm の円筒形にした。比較標準試料も同様の形状にして石英管に封じたのち，東北大学理学部原子核理学研究施設の電子線型加速器で，30MeV の制動輻射ガンマ線で３時間照射した。照射後に，アルミニウム箔で包みなおしたのち，生成した核種からのガンマ線を高純度ゲルマニウム検出器で測定して，含まれる元素濃度を算出した。定量に用いた同位体の核的性質を第２表に示す。

2.3.2　AAS

生物試料を酸分解により溶液にするために PROLABO 密閉型マイクロウエーブ式湿式分解装置（MCS950）を用いた。2.1で作成した粉末試料0.7g を専用容器にいれ，濃硝酸7mL を加えてマイクロウエーブで加熱分解した。冷却後に得られた溶液を50mL メスフラスコに移し，0.1 M 硝酸で標線をあわせたのち，0.45μm ミリポアフィルターでろ過して試料溶液とした。Na, K, Mg, Ca の定量を行うためには上記のように作成した水溶液を0.1 M 硝酸で適宜希釈して日立偏光ゼーマン原子吸光光度計 Z-6100に直接噴霧し，得ら

第2表　Nuclear data for analyzed elemens。

Element	Target nuclide	Nuclear reaction	Product nuclide	Half-life	Gamma-ray used, keV
As	As-75	(γ, n)	As-74	17.78d	595.9, 634.8
Br	Br-79	(γ, 2n)	Br-77	2.3765d	238.97
Ca	Ca-44	(γ, p)	K-43	22.3h	372.9
Cr	Cr-52	(γ, n)	Cr-51	27.704d	320.1
Cu	Cu-63	(γ, 2n)	Cu-61	3.41h	282.9
Fe	Fe-56	(γ, pn)	Mn-56	2.579h	846.8
I	I-127	(γ, n)	I-128	13.0d	388.6, 666.3
Mg	Mg-25	(γ, p)	Na-24	15.02h	1368.6
Mn	Mn-55	(γ, n)	Mn-54	312.2d	834.8
Mo	Mo-100	(γ, n)	Mo-99	66h	140.5
Na	Na-23	(γ, n)	Na-22	2.602y	1274.6
Ni	Ni-58	(γ, n)	Ni-57	36h	1377.6
Rb	Rb-85	(γ, n)	Rb-84	32.9d	881.6
Sn	Sn-118	(γ, n)	Sn-117m	14.0d	158.6
Sr	Sr-88	(γ, n)	Sr-87m	2.8h	388.4
Zn	Zn-66	(γ, n)	Zn-65	244.1d	1115.5

れた吸光度とあらかじめ求めておいた検量線から濃度を算出した。Fe，Ni，Cu，Zn の定量は以下のように行った。すなわち，100mL 分液ロートに試料溶液40mL をとり，10％ジエチルジチオカルバミン酸ナトリウム（DDTC）水溶液10mL を加え，6M NaOH 水溶液で溶液の pH をほぼ中性に調整後，pH8.6 緩衝溶液5mL を加えて５分間放置した。メチルイソブチルケトン（MIBK）10mL を加えて５分間振とう後，二相を分離した。有機相を AAS で吸光度測定し，水相から再び DDTC と MIBK で抽出後，有機相を AAS で吸光度測定した。あらかじめ既知濃度の金属水溶液から DDTC-MIBK 抽出を行い，求めておいた検量線から試料中の元素濃度を算出した。

§ 3．結果と考察

上記2.2に示した３種類の比較標準物質について得られた分析値を第３表に示す。３種類の比較標準物質の Mn，および Bovine Liver の Ca と Mo を除けば，得られた分析値は与えられた公定値および推奨値と10％の範囲内でよく一致し，PAA および NAA の信頼性が示された。さらに，公定値の与えられていない比較標準物質の元素のうち，Oyster Tissue の Br と Mo，Bovine Liver の Cr，I，Ni，Lobster の Br，I，Rb について分析値を得ることができた。

3.1　サイズの異なる粉末試料間の濃度差

上記3.1に示したように，分析試料を乾燥粉末にしたのち，200mesh のふるいで分別した。生物体の臓器や器官の多くは，臓器や器官内でマクロには均質であっても，繊維質の構成物質は200mesh のふるいを通る微粉末にはなりにくいと考えられる。そこで数種類の生物種や器官について，粉末を200mesh 以下と以上の２種類に分類して分析した結果を比較してみた。第４表に７種類の分析試料について同一個体の粒径別粉末から各々３試料作成して得られた濃度を平均値±標準偏差のかたちで示している。また，それらのうちのシャコエビ腹部筋，バカガイ軟体部，ウニ生殖腺については各々第２図，第３図，第４図に示してある。これらの結果より，アワビ筋の Fe やシャコエビ腹部筋の Mg，Na，Zn などの一部を除けば，十分に満足できるものであった。バカガイ軟体部の Ca，Fe，Mn，Sr の分析値の誤差が非常に大きいが，この理由としては軟体部に含まれている黒色の微粒子が考えられ，これの主成分は Fe，Mn，Ca，Sr であると思われる。第２図および第３図においては，粒径別の濃度差は認められないが，第４図に示すウニ生殖腺ではCa，Cu，Fe，

Mg, Mn, Na, Sr, Zn の8元素に差異が見られた。これは性差に原因があると考え[3]，生殖腺の顕微鏡観察を行ったが，卵や精子を認めるのは困難であった。ウニの性差による元素濃度の差異については今後検討する必要がある。

上に述べたように，いくつかの例外はあったものの，多くの試料については粒径間の差異は認められなかったので，以後の実験では200mesh 以上の粉末を使用することにした。

3.2 PAA と AAS 比較

同一の試料について異なる分析法を用いて定量した場合の結果を第5表に比較してみた。分析した試料はシャコエビの腹部筋とマガキの軟体部で，各々5個体ずつ用いた。比較してみるとほとんどの元素濃度が異なっており，特にシャコエビ腹部筋の Ca 濃度の差は非常に大きい。この原因としては AAS で分析する前に行う酸分解が考えられる。酸分解後に不溶物が残ることがあり，AAS 分析の前にろ過することにより，誤差が生じると考えられる。AAS は非常に簡便な分析法であり，一般的な分析機器であるが，前処理としておこなう試料の分解法については注意する必要があることを示している。

3.3 分析試料の元素濃度

PAA で得られた全試料の元素濃度の平均値を第5図にプロットで示した。これより Mg および Rb の濃度は生物種や部位によらず各々 10^3-10^4，1-10 μg/g DW とほぼ一定値を示していることがわかる。また，As も濃度範囲は狭い。それ以外の元素濃度は2桁から3桁の幅をもっていることがわかる。

3.4 生育地の異なる生物種間の濃度差

生息地の異なる数種類の貝類軟体部について得られた Ni 濃度を第6図に示す。一般的に生物体中の Ni 濃度は低く，乾燥重量にして数 μg/g 以下であるが，第6図より明らかなように，貝類軟体部には Ni 濃度が高く，また生息地が輪島，佐渡島，相馬のアワビの中腸腺には非常に高濃度の Niが検出された。アワビは海底で生息していることが知られており，海底に堆積している底質の差異を反映していると考える。また，鳥羽および奄美のイセエビ各々3個体のエラおよび肝すい腺を分析した結果を平均値で第7図に示す。標準偏

第3表　The concentrations of elements in the Standard Reference Materials. (unit: μg/g dry wt.)。

	NIST SRM-1566a Oyster Tissue			NIST SRM-1577b Bovine Liver			NRCC Lobster		
	Certified Value (mean±SD)	This Work (mean±SD)	n**	Certified Value (mean±SD)	This Work (mean±SD)	n**	Certified Value (mean±SD)	This Work (mean±SD)	n**
As	14±1.2	13.2±1.6	31	0.05*	0.7±1.2	11	24.6±2.2	26.6±2.9	30
Br		49.5±18.5	11	9.7*				232±102	10
Ca	1960±190	2080±140	31	116±4	146±27	11	8950±580	8400±460	26
Cr	1.43±0.46	0.7±1.0	8				2.4±0.6	2.4±2.0	4
Cu	66.3±4.3	70.0±36.7	27	160±8	166±26	11	439±22	420±74	15
Fe	539±15	503±77	23	184±15	208±44	11	186±11	192±86	30
I	4.46±0.42				0.3±0.1	11		21.6±7.1	30
Mg	1180±170	1107±34	27	601±28	608±23	11	2550±250	2930±540	30
Mn	12.3±1.5	16.6±3.6	23	10.5±1.7	10±1.9	11	23.4±1.0	15.4±7.0	26
Na	4170±130	4300±290	27	2420±60	2500±480	11	36700±2000	35700±2500	30
Ni	2.25±0.44	1.9±1.0	4				2.3±0.3	1.8±1.4	12
Rb	3*	3.4±0.6	11	13.7±1.1	12.6±2.1	11		2.8±1.6	30
Sr	11.1±1	12.2±1.1	23	0.136±0.001	0.2±0.1	11	113±5	106±17	30
Zn	830±57	730±148	27	127±16	117±7	11	177±10	193±16	26

*noncertified value
**number of samples detected

第４表　乾燥粉末試料の粒経別元素濃度（単位：μg/g dry wt.）。

	ガザミ（男鹿）頭胸部筋	ホタテガイ（雄勝）閉殻筋	アワビ（雄勝）筋	シャコエビ（雄勝）腹部筋	バカガイ（雄勝）軟体部	アワビ（雄勝）中腸腺	ウニ（雄勝）生殖腺
As	10.5	3.6±0.2	12.8±2.8	29.0±8.2	17.0±4.6	36.6±0.2	11.8±4.4
	29.9±1.7	4.5±1.5	15.1±4.9	53.1±29.3	27.2±23.6	46.8±1.8	9.0±0.5
Br					90.2±18.9		
					88.9±3.7		58.0±4.1
Ca	765±58	384±18	1920±60	1590±610	4690±2060	1670±170	4940±3070
	9200±100	3.9±1.3	2200±60	2700±1570	10500±6900	2990±200	667±19
Cu			35.8±44.8	83.3±17.7	46.8±11.6		42.9±23.4
			58.8±40.0	187±135	25.8±44.7		8.4±5.2
Fe	13.3±18.7	14.9±8.0	112±51	5.3±7.2	1370±2290	573±67	1.3±2.2
	286±20	26.5±25.3	267±194	55.8±23.0	6500±11300	2540±150	36.9±23.3
I	8.4±0.4	0.2±0.1	8.1±0.2	0.9±0.3	2.8±2.5	10.3±0.5	13.1±1.4
	25±0.2	0.4±0.1	9.8±0.5	1.7±1.7	3.5±3.1	15.5±0.4	5.6±0.2
Mg	1600±60	1710±20	5390±90	1400±440	3290±380	3360±30	3540±330
	2960±30	1640±40	5770±90	2550±1400	3750±1250	4010±100	1600±10
Mn	0.1	0.5±0.4	3.0±0.6	3.4±2.3	569±984	6.0±0.4	8.5±9.2
	15.7±0.6	1.4±0.7	0.9±0.8	3.1±2.0	2750±4760	22.9±0.8	1.9±0.2
Mo	1.8±0.3				0.3±0.4	12.7±3.7	
	10.0±1.8				0.7±0.6	21.0±7.4	0.2±0.2
Na	8790	4720±50	34800±300	10800±3600	20100±3300	11400±200	34500±13400
	36400±200	5010±170	37600±400	19100±10200	19300±1700	11800±100	7200±64
Ni			16.2±4.0	2.7±4.7			2.0±0.9
			13.7±1.9	8.8±13.3			0.2
						14.6±3.5	10.0±1.2
Pb	2.9±4.0					18.5±3.1	
	16.8±7.9						
Rb	5.9	4.2±0.2	2.4±0.8	1.9±0.9	4.3±1.3	4.9±0.1	4.6±3.6
	2.7±2.2	4.3±0.2	3.6±1.3	4.2±1.1	5.9±0.7	5.4±0.5	6.1±1.7
Sn		2.4±2.4			6.2±2.9		
		2.3±2.0			13.5±8.9		
Sr	7.8±0.9	4.0±0.1	30.3±0.9	19.8±8.4	49.7±43.4	16.1±0.3	72.5±47.1
	105±3	4.0±0.2	35.7±0.5	33.4±19.6	154±201	33.3±2.1	7.1±0.1
Zn	50.5±0.8	52.7±9.8	61.3±3.4	116±42	60.8±62.9	30.9±0.6	339±153
	113±3	56.4±9.9	62.8±4.6	201±121	205±213	58.0±4.6	120±22

上欄：粒経200mesh 以下，下欄：粒経200mesh 以上

差はエラーバーで示されている。エラについてはAs，Br，Ca，Fe，Rbに濃度の差がみられたが，肝すい腺についてはCa以外には差がみられなかった。エラは生息海域の海水に直接接触しており，また，多くの微生物がエラの表面に生息していることが知られている。このことより，エラの分析値は生息地の環境の違いを反映しやすいと思われる。それに対して，肝すい腺は，生物体が体内に吸収した物質を代謝したのちに蓄積する器官であるから，岩礁に生息するイセエビはアワビの中腸腺ほどは底質の違いを示さないのだと思われるが，これらの点についてはさらに底質や，食物にしている海草類などもあわせて元素の定量を行う必要があると思われる。

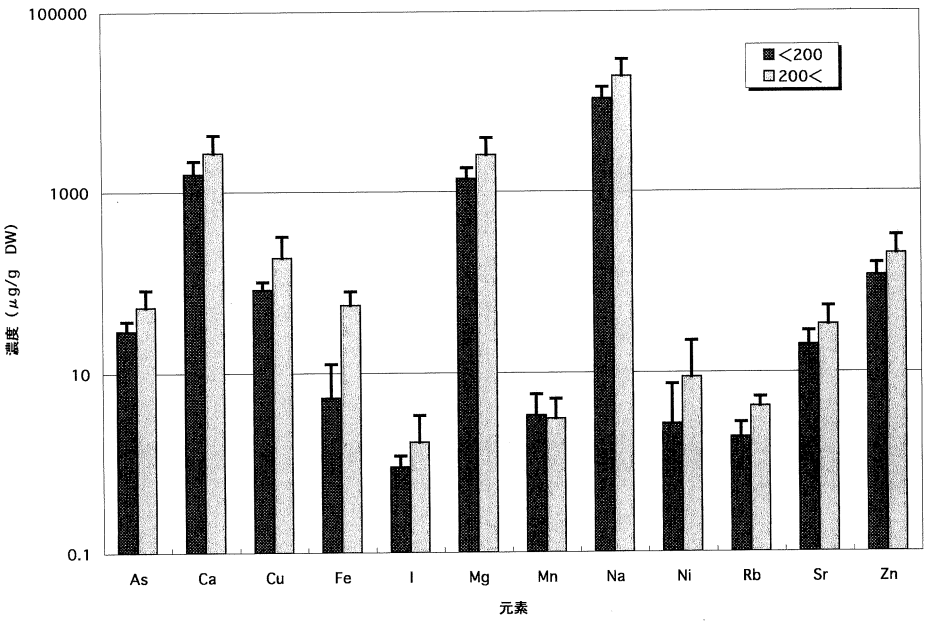

第２図　シャコエビ腹部筋の粒径の異なる粉末の元素濃度。

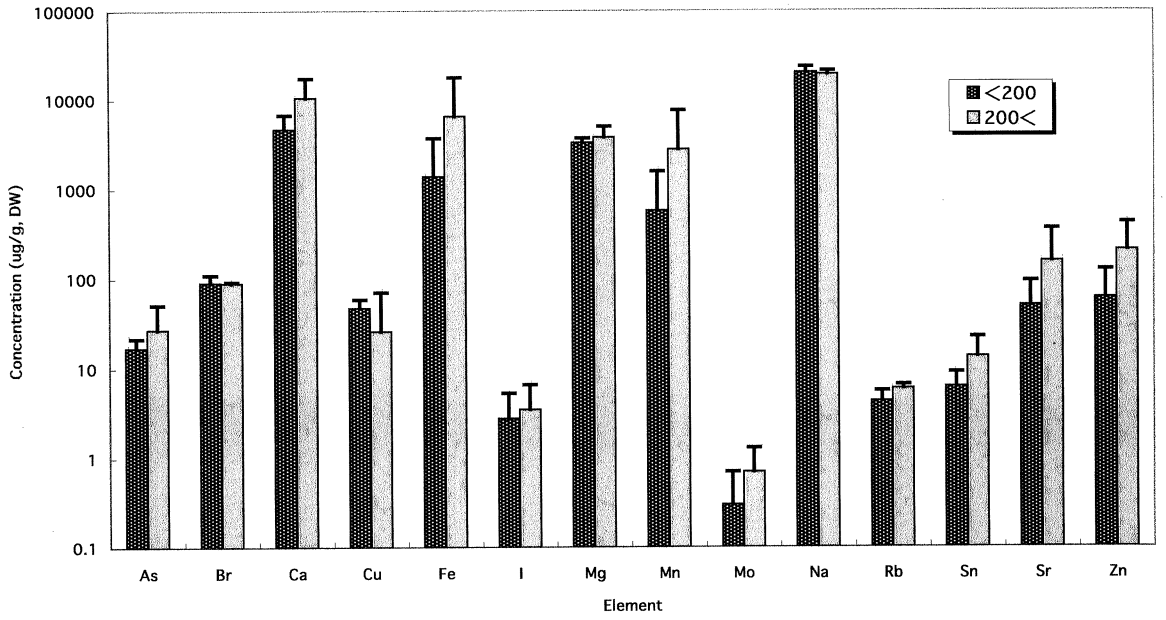

第３図　バカガイ軟体部の粒径の異なる粉末の元素濃度。

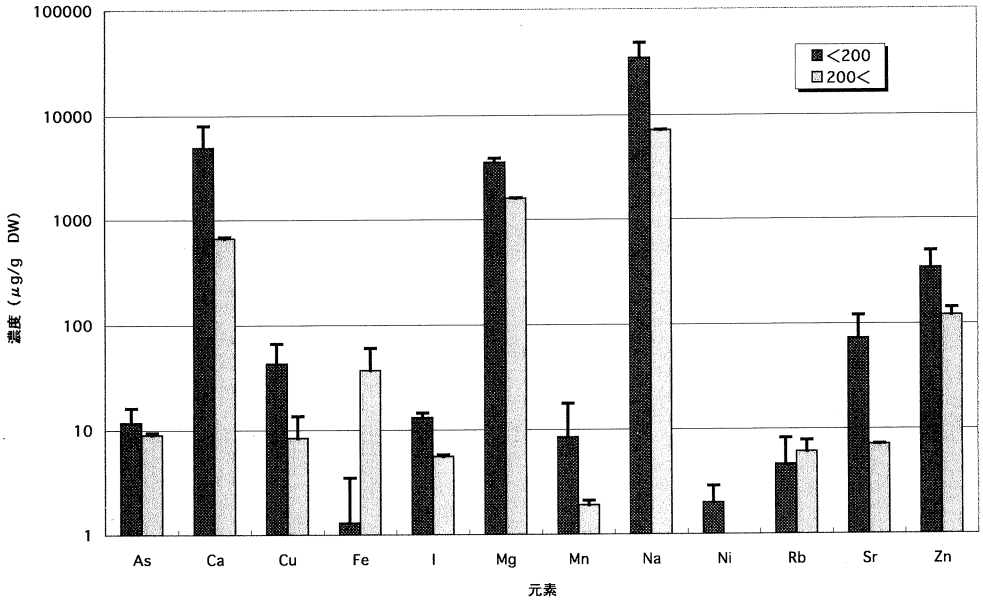

第４図　ウニ生殖腺の粒径の異なる粉末の元素濃度。

第５表　軟体動物の元素濃度の分析法による比較（平均値±標準偏差，単位：μg/g dry wt.）。

元素	シャコエビ腹部筋（雄勝）		マガキ軟体部（雄勝）	
	PAA	AAS	PAA	AAS
Na	11800±4500	15000±5100	28300±7300	27500±7500
Mg	1720±540	2140±840	3990±850	5570±1350
Ca	2110±630	133±54	3440±850	4950±3150
Fe	40.2±10.3	14.9±11.9	252±110	139±64
Ni	8.0±9.8	ND	ND	ND
Cu	101±59	157±75	190±75	175±42
Zn	139±36	57.0±29.8	1290±300	551±285

$n=5$

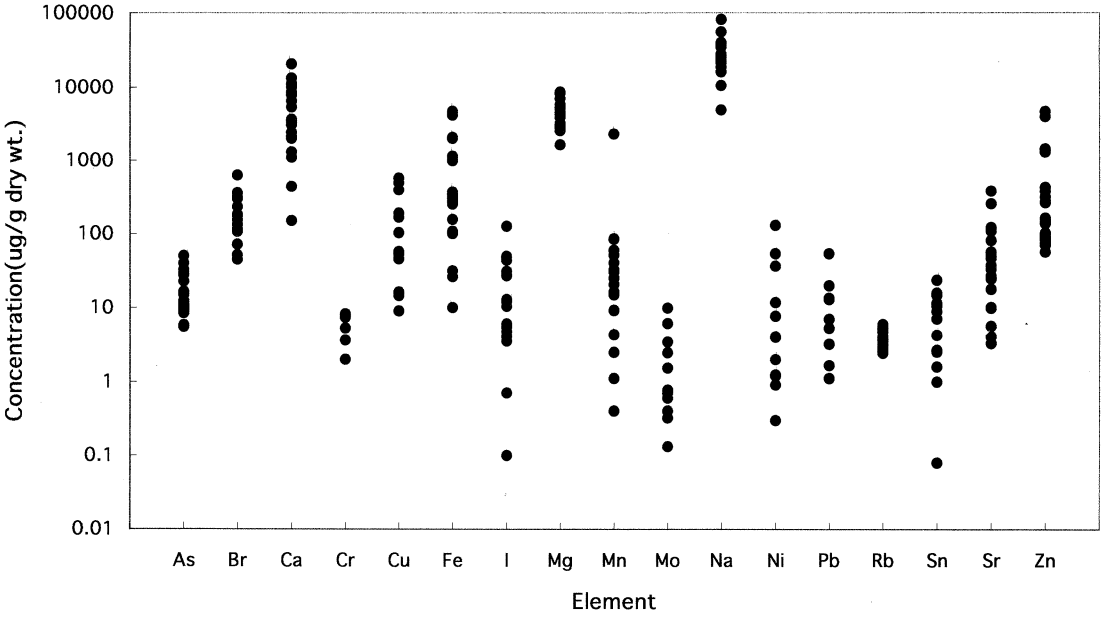

第5図　Concentration levels of elements in the several species of marine invertebrates.

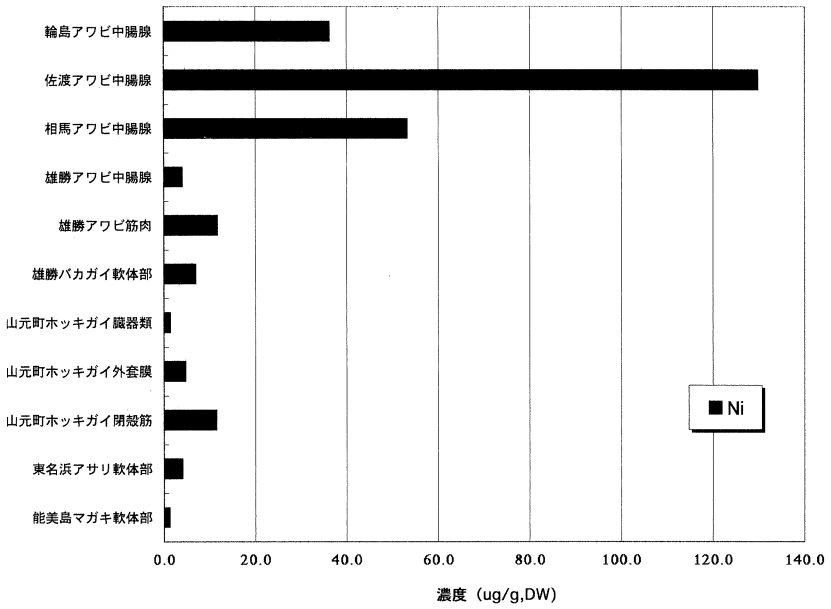

第6図　貝類軟体部中の Ni 濃度度。

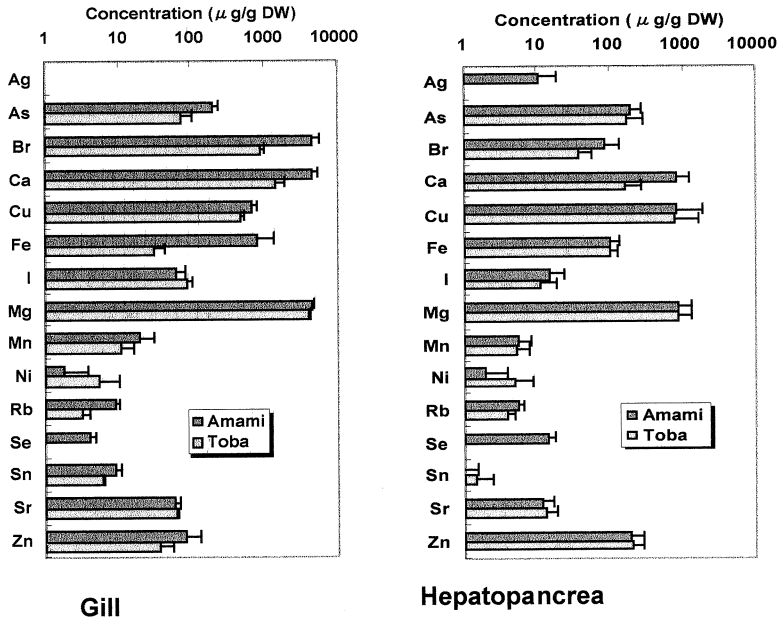

第7図　生息地の異なるイセエビの元素。

§4. まとめ

これまで国内の沿岸で捕獲される海生軟体動物についてPAAおよびNAAの二法で18元素の濃度を得ることができた。それらの結果より，アワビの中腸腺や各生物種のエラの濃度に生息地の環境の違いが表れていると思われる。このようなことを明らかにするために，軟体動物を取り囲む環境を構成している海水，底質，海藻などの食物についてさらに分析値を得る必要があるだろう。

§5. 謝　辞

本研究を行うにあたり光量子放射化分析のための照射や測定でお世話になった東北大学原子核理学研究施設の大槻勤博士ならびにマシングループの方々に感謝いたします。この研究は東北大学原子核理学研究施設の共同利用によって行われました。

また，生息地の明らかな，処理の施していない試料を入手してはじめて，この研究を行うことができました。生物試料を収集するためにご助言，ご協力くださいました㈲宮城県水産研究開発センター：阿部洋士部長，マルハ㈱：木原稔氏，前川水産㈱：前川隆則氏，石巻専修大学：菅原善雄教授，坂田隆教授に深く感謝いたします。

参　考　文　献

[1] 福島美智子，玉手英利：核理研研究報告　31 (1998) 22.

[2] M. Fukushima, H. Tamate, Y. Nakano : J. Radioanal. Nucl. Chem. 244 (2000) 55.

[3] Andre Tessier, David R. Turner (Eds) : *Metal Speciation and Bioavailability in Aquatic Systems* (John Wiley & Sons, 1995)

Se-Atom Incorporation in Fullerene and the MD Simulation

T. Ohtsuki[1], H. Yuki[1], K. Ohno[2], K. Shiga[3], Y. Kawazoe[3],
K. Shikano[5] and K. Masumoto[6]

[1]*Laboratory of Nuclear Science, Tohoku University, Mikamine, Taihaku, Sendai 982-0826*
[2]*Department of Physics, Yokohama National University, Yokohama, 240-8501*
[3]*Institute for Materials Research, Tohoku University, Aoba-ku, Sendai 980-8577*
[4]*NTT Opto-Electronics Laboratories, Tokai, Ibaraki, 319-11*
[5]*Radiation Science Center, KEK, Tanashi, Tokyo 188*

The formation of Se atom-incorporated fullerenes has been investigated by using radionuclides produced by nuclear reactions. From the trace of radioactivities of ^{75}Se after High Performance Liquid Chromatography (HPLC), it was found that the formation of endohedral fullerenes or heterofullerenes is possible by a recoil process following the nuclear reactions. To confirm the produced materials, *ab initio* molecular-dynamics simulations based on an all-electron mixed-basis approach were carried out. We found that the insertion of Se atom into C_{60} cage is much easier than that of As and Ge atoms.

§ 1. Introduction

Fullerenes are the new type of carbon compounds and show very interesting physical and chemical properties. Especially, chemical interaction between C_{60} and a variety of atoms is becoming a very new field of cluster research. So far, numerous experimental studies for endohedrally doped [1-10] or exohedrally doped [11-13] fullerenes with foreign atoms have been undertaken by resorting to arc-desorption or laser-vaporization techniques. On the other hand, it has become possible to synthesize the heterofullerenes, where the foreign atom is incorporated into the carbon cage. Experimentally, heterofullerenes doped with foreign atoms, such as boron (B) [14, 15] nitrogen(N)[16, 17] silicon (Si) [18, 19] have been reported. In our previous studies, we have studied not only the endohedral doping of Be [20], Kr and Xe [21] but also the substitutional doping of ^{11}C [22], ^{13}N [23], ^{69}Ge and ^{72}As [24] by a recoil-implantation process following nuclear reactions. In spite of the intense research, only partial facts for the formation process and the produced materials have been unveiled on the nature of the chemical interaction between a foreign atom and a fullerene cage. Therefore, it is important and intriguing to synthesize new complexes, such as several foreign-atom incorporated fullerenes, and to investigate their properties so that knowledge about how to produce large amount of these complexes is gained.

In this paper, we show evidence of Se atom-incorporated fullerenes on the collision between a C_{60} cage and an Se atom, which was generated from a recoil process following nuclear reactions. We performed *ab initio* molecular-dynamics (MD) simulations: whether the Se atom can be incorporated in the fullerene with the endohedral doping: Se@C_{60}. Furthermore, the chemical nature of the Se atom in a fullerene is compared with that of the Ge and As atoms.

§ 2. Experimental Procedure

In order to produce Se atom-incorporated fullerenes, about 10 mg of C_{60} fullerene powder was mixed homogeneously with 10 mg of As_2S_3 (200 meshes), and used to the target material. Deuteron irradiation with beam energy of 16 MeV was performed at the Cyclotron Radio-Isotope Center (CYRIC), Tohoku University. Radioisotopes of ^{75}Se can be produced by ^{75}As (d, 2n) ^{75}Se reactions. The beam current was typically 5 μA and the irradiation time was about 1 hour. The sample was cooled with He-gas during irradiation. After the irradiation, the samples were left for one day to cool down the several kinds of short-lived radioactivities of byproducts. After the one-day cooling, radioactivities, such as ^{11}C or ^{13}N, e.g., ^{11}C decays to ^{11}B with $T_{1/2}$=20 min, the radioactivities of ^{75}Se could be measured with its characteristic γ-rays. The typical γ-ray and the half-life ($T_{1/2}$) of ^{75}Se are 136 keV (and 265 keV), 120 days, respectively.

The fullerene samples were dissolved in o-dichlorobenzene after being filtrated to remove insoluble materials through a membrane filter (pore size = 0.2 μm). The soluble fraction was injected into a High Performance Liquid Chromatograph (HPLC) equipped with a 5PBB (silica-bonded with the pentabromo benzyl group) column of 10 mm (inner diameter)×250 mm (length), at a flow rate of 3 ml/min. The eluted solution was passed through a UV detector, the wavelength of which was adjusted to 290 nm in order to measure the amount of fullerenes and their derivatives. The fraction was collected at 30 sec intervals, and the γ-ray activities of each fraction were measured with a Ge-detector. Therefore, the existence of ^{75}Se could be confirmed by their characteristic γ-rays.

§ 3. Results and Discussion

The elution curve shown by solid line in Fig. 1 indicates the absorbances monitored continuously by a UV detector for the irradiated samples of $C_{60}+As_2S_3$. The horizontal axis indicates the retention time after injection into the HPLC, and vertical one indicates the absorption intensity of the UV and the γ counting rate of the ^{75}Se radionuclide produced by ^{75}As (d,2n) ^{75}Se reaction. A strong absorption peak

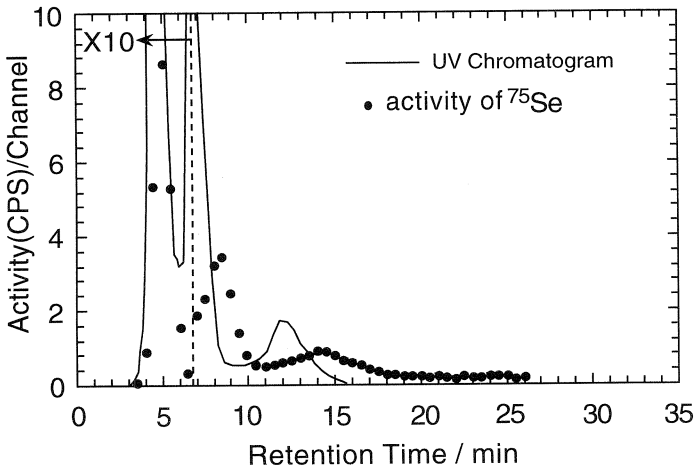

Fig.1. HPLC elution curves of the soluble portion of the crude extracted in the deuteron irradiated sample of C_{60} mixed with As_2S_3. The horizontal axis indicates retention time, while the vertical axis represents the counting rate of the radioactivities of ^{75}Se (solid circles) measured with a Ge-detector and the absorbance of a UV chromatogram of C_{60} (solid line).

was observed at the retention time of 4.2 - 5.2 min in the elution curve (solid line) which was measured by the UV detector. This peak position corresponds to the retention time of C_{60} which was confirmed by the calibration run using the C_{60} sample before the irradiation. Following the first peak, two peaks at around 6.5 - 7.2 min and 10 - 15 min were consecutively observed in the UV chromatogram. This fact indicates that the second and smaller third peaks can be assigned to C_{60} dimers and C_{60} trimers, respectively, with resorting to TOFMAS measurements. These materials can be produced by the interaction between C_{60}'s in coalescence reactions after ionization by the incident or produced charged particles. Three peaks appeared in the curve of the ^{75}Se radioactivities in the radiochromatogram. Aside from a slight delay, the first peak (5.0 min) corresponds to the C_{60} UV absorption peak. The second as well as the relatively broad third peaks were observed at the retention time of 7 - 10 min, and of 11 - 18 min, respectively. Though there is a delay in the elution peaks of the radioactivities against that of the UV absorption peaks, it seems that the elution behavior is similar. This result indicates that the radioactive fullerene monomers and their polymers (dimers and trimers) labeled with ^{75}Se possibly exist in the final fractions.

In order to understand the present experimental results, *ab initio* molecular-dynamics simulations were carried out. The method, which is used here, is based on the all-electron mixed-basis approach [26-28] using both plane waves (PW's) and atomic orbitals (AO's) as a basis set within the framework of the local density approximation (LDA). In the present study, all the core atomic orbitals are determined numerically by a standard atomic calculation based on Herman-Skillman's framework with logarithmic radial meshes. For the present system,we use 313 numerical AO's and 4,169 PW's corresponding to a 7 Ry cutoff energy. For dynamics, we assume the adiabatic approximation where the electronic structure is always in the ground state. We utilize a supercell composed of $64\times64\times64$ meshes, where one mesh corresponds to 0.196 Å. We set the basic time step as $\Delta t = 0.1$ fs and perform five steepest descent (SD) iterations after each updation of atomic positions. We do not impose any velocity control, so that the system is almost microcanonical with a little energy dissipation from the SD algorithm.

First, we show the results of the following simulation; an Se atom with a kinetic energies (K.E.) 40 eV hits vertically the center of a six-membered ring (u-C_6) of C_{60}. From the simulation, we found that an Se atom can penetrate into C_{60} easily when its initial speed is 40 eV, and stop at the inside of the C_{60} cage (see Figure 2). Although, an Se atom goes out again from the opposite side of the cage when its initial speed is greater than 100 eV. For an interaction with the K.E. lower than 40 eV, the Se atom first touches u-C_6, carbon atoms are pushed to open u-C_6, but the u-C_6 soon recovers its initial configuration. Similar simulations were performed for the case of As. In this case, we found that an As atom can penetrate into C_{60} if its K.E. is greater than 70 eV, although, an As atom goes out again from the opposite side of the cage when its initial energy is greater than 160 eV. Comparing Se and As, we found that the formation of Se@C_{60} seems to be easier than that of As@C_{60}, because the energy range of the insertion for Se atom is relatively lower than that for As atom.

Second, we put additionally one Se atom on the radial axis by 1.39 Å inward from the original C position of C_{60}. Then, starting the simulation with zero initial velocity. We found that there is a force acting on the Se atom to accelerate it inward, and finally, the Se atom stops at around the center of C_{60}

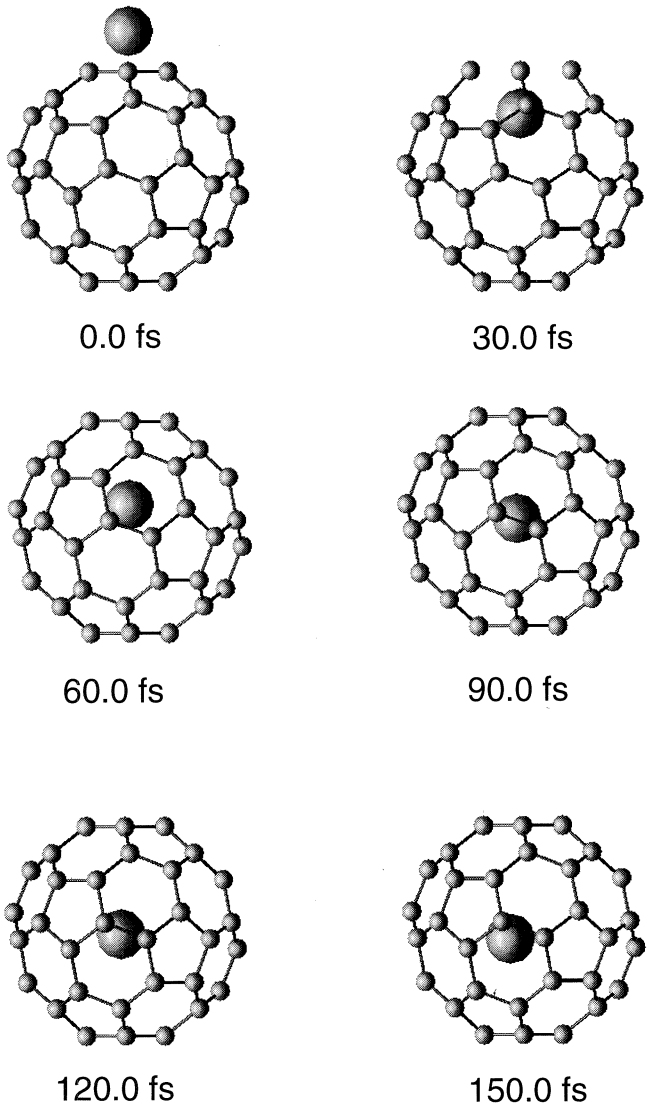

Fig.2. Simulation of Se hitting the center of a six-membered ring (u-C_6) of C_{60} with a kinetic energy of 40 eV. Here, the local skeleton disappears from the figure when the bond length is elongated to more than by 1.5Å.

We also put additionally one As atom on the same radial axis by 1.39 Å inward from the original C position of C_{60}. we found that there is a strong force acting on the As atom to accelerate it outward and, as a result, to repel the outward C atom. Finally, the As atom stops at 0.50 Å from the cage sphere. Thus, it seems that the As atom put inside the cage is relatively unstable and has a strong tendency to repel the closest C atom of C_{60}, and is stabilized slightly outside the cage sphere after the removal of the closest C atom. Therefore, a heterofullerene, such as AsC_{59}, may exist stably under realistic conditions. It should be noted that similar results for the case of a Si atom have been reported by Pellarin *et al* [18, 19] (however, the possibility for endohedral doping, As@C_{60}, can not be completely excluded at present, there seems to be a local stable point inside the cage).

Radiochromatogram of ^{69}Ge, ^{72}As and ^{75}Se are shown in Fig. 3 (a) and 3 (b), respectively. The area ratios, the peak area assigned by "A" and "B" in Figs. 3 (a) and (b), are shown in Fig. 3 (c) for Ge, As and Se atom, respectively. It is interesting and important to note that the area ratio, A/B (monomer/

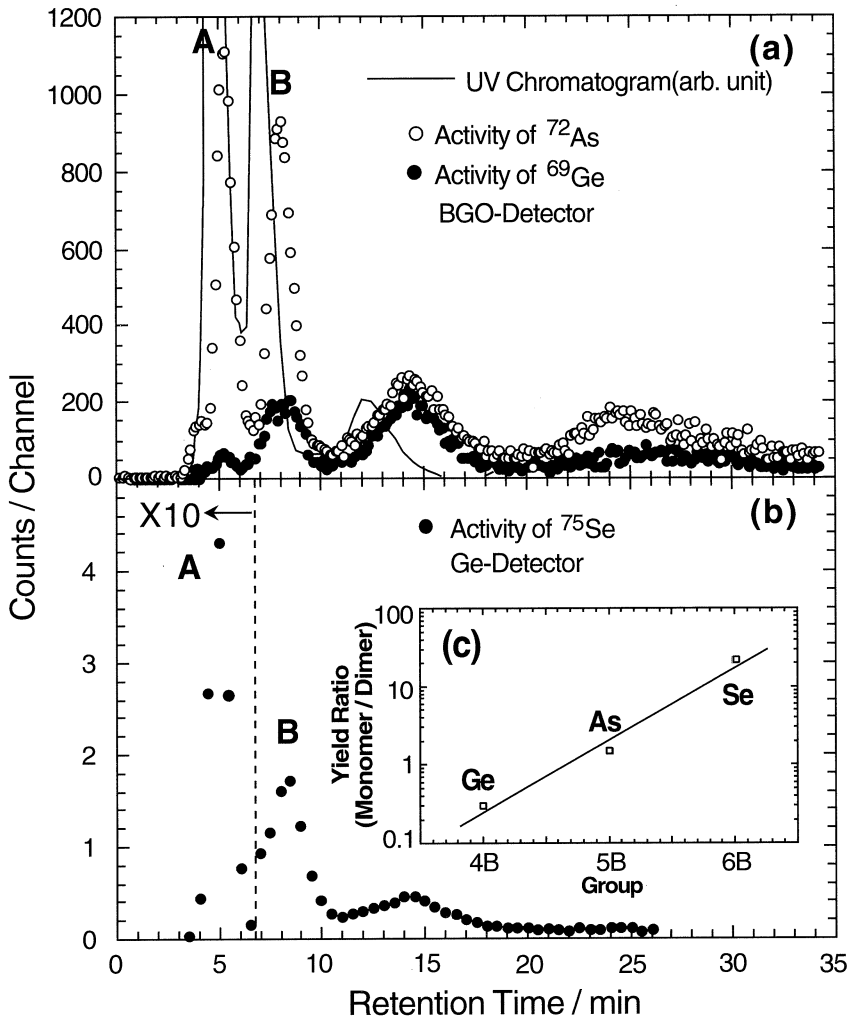

Fig.3. (a) HPLC elution curves of the soluble portion of the crude extracted in the deuteron irradiated sample for the production of ^{69}Ge and ^{72}As taken from ref. [24]. The horizontal and the vertical axes are same as Fig. 1, but for ^{69}Ge and ^{72}As. (b) Same as (a), but for ^{75}Se for comparison with the ^{69}Ge and ^{72}As cases. The difference in vertical scale between (a) and (b) is due to the efficiency of BGO- and Ge-detectors. (c) Area ratio, monomer/dimer indicated by the peaks "A" and "B" in (a) and (b), in the radiochromatogram of 4B～6B (Ge～Se) atoms.

dimer), in the radiochromatogram of ^{75}Se is much larger than that in the radiochromatogram of ^{72}As (and further much larger than that in the radiochromatogram of ^{69}Ge). This trend indicates that the shock caused by collision with higher K.E. (e.g. ～70 eV, for As atom) most probably induced the cage to create dimers with a higher rate. The difference can be due mainly to the nature of the covalent bonding between the C atom and the 4B～6B (Ge～Se) atoms.

§ 4. Conclusion

In this study, the formation of atom-incorporated fullerenes has been investigated by the trace of radioactivities of ^{75}Se produced by nuclear reactions. It was found that 6B element, like Se, remained in the final C_{60} portion after a HPLC process. This fact suggests that the formation of ^{75}Se atom-incorporated fullerenes can be possible by a recoil process following nuclear reactions. Carrying out *ab*

initio molecular-dynamics (MD) simulations on the basis of the all-electron mixed basis approach, we showed possibility of the formation of endohedral fullerene for Se atom. In comparison with 4B～6B (Ge～Se) atoms, we found that the insertion of Se atom into C_{60} cage is much easier than that of As and Ge atoms.

Acknowledgments

The authors are grateful to the staff of the Cyclotron Radio-Isotope Center (CYRIC) for handling the beam, and are grateful to the technical staffs, working at IMR, Tohoku University, for their continuous support, for the supercomputing facilities of HITAC S 3800. This work was supported by the Grants-in-Aid for Co-operative Research No. 12640532 from the Ministry of Education, Science and Culture of Japan.

References

[1] Y. Chai *et al.,* Phys. Chem. **95** (1991) 7564.
[2] R.D. Johnson *et al.,* Nature (London) **355** (1992) 239.
[3] J. H. Weaver *et al.,* Chem. Phys. Lett. **190** (1992) 460.
[4] H. Shinohara *et al.,* Nature (London) **357** (1992) 52.
[5] M. Takata *et al.,* Nature (London) **377** (1995) 46.
[6] W. Sato *et al.,* Phys. Rev. Lett. **80** (1998) 133.
[7] M. Saunders *et al.,* Science **271** (1996) 1693.
[8] T. Braun and H. Rausch, Chem. Phys. Lett. **288** (1998) 179.
[9] T. Braun and H. Rausch, Chem. Phys. Lett. **237** (1995) 443.
[10] G.E. Gadd, *et al.,* J. Am. Chem. Soc. **120** (1998) 10322.
[11] L.M. Roth, *et al.,* J. Am. Chem. Soc. **113** (1991) 6298.
[12] Y. Huang, and B.S. Freiser, J. Am. Chem. Soc. **113** (1991) 9418.
[13] S.W. McElvany, *et al.,* J. Phys. Chem. **96** (1992) 4935.
[14] T. Guo, *et al.,* J. Phys. Chem. **95** (1991) 4948.
[15] H.J. Muhr, *et al.,* Chem. Phys. Lett. **249** (1996) 399.
[16] T. Pradeep, *et al.,* J. Phys. Chem. **95** (1991) 10564.
[17] J.F. Christian, *et al.,* J. Phys. Chem. **96** (1992) 10597.
[18] M. Pellarin, *et al.,* Chem. Phys. Lett. **277** (1997) 96.
[19] C. Ray, *et al.,* Phys. Rev. Lett. **80** (1998) 5365.
[20] T. Ohtsuki, *et al.,* Phys. Rev. Lett. **77** (1996) 3522.
[21] T. Ohtsuki, *et al.,* Phys. Rev. Lett. **81** (1998) 967.
[22] T. Ohtsuki, *et al.,* J. Am. Chem. Soc. **117** (1995) 12869.
[23] T. Ohtsuki, *et al.,* J. Radioanal. Nucl. Chem. **239** (1999) 365.
[24] T. Ohtsuki, *et al.,* Phys. Rev. **B60** (1999) 1531.
[25] R.B. Firestone, *et al.,* Eds. Table of Isotopes, 8th Ed. Vol.I. John Wiley & Sons, Inc. 1996.

[26] K. Ohno, *et al.,* Phys. Rev. Lett. **76** (1996) 3590.

[27] K. Ohno, *et al.,* Phys. Rev. **B56** (1997) 1009.

[28] K. Shiga, *et al.,* Modelling Simul. Mater. Sci. Eng. **7** (1999) 621.

Ⅲ. Accelerator, Synchrotron Radiation, and Instrumentation

Tune Measurements of a 1.2 GeV Booster Electron Synchrotron at LNS

H. Hama, F. Hinode, O. Konno, A. Kurihara, A. Miyamoto, M. Mutoh, M. Nanao, M. Oyamada, Y. Shibasaki, K. Shinto and S. Takahashi

Laboratory of Nuclear Science, Tohoku University, 1-2-1 Mikamine, Taihaku-ku, Sendai 982-0826

A 1.2 GeV booster electron synchrotron (STB ring) with combined use of pulse-beam stretcher at Laboratory of Nuclear Science (LNS) [1], Tohoku University was constructed for study of nuclear physics, which is also supposed to be an injector for a planned future 3rd generation light source. Currently the STB ring is routinely operated with a booster-storage mode to supply high energy γ-rays for nuclear study produced via bremsstrahlung using an internal target wire. Since finite range of a tagging counter array mounted in a bending section, the booster has to be also operated at another flat-top energy lower than 1.2 GeV to extend the γ-ray energy toward lower side. Because characteristics of the STB ring have not been well understood, various beam properties such as betatron tunes and instabilities are not completely controlled at the moment. In order to improve performance of the machine and to study the beam dynamics in a circular accelerator, fundamental properties of the STB ring is now being measured.

§ 1. The STB ring

1.1 Basic parameters

The STB ring constructed as a multipurpose synchrotron was commissioned in these years and has become routinely operational recently. At the moment there are two major tasks, i.e., a pulse-beam stretcher to produce the quasi cw-beam at the lower energy region from 150 to 200 MeV, and the booster-storage ring to supply internal 1.2 GeV beam. In this issue we mainly report on characteristics of the latter operation.

Main parameters and current status of the STB ring is summarized in Table 1. Lattice structure of the ring is the simplest double-bend achromat consisted of 4 cells, which is shown in Fig.1. Three dispersion-free straight sections are occupied by an injection septum, an RF cavity and a wire septum for slow extraction, and an extraction septum, respectively. Remaining one is reserved for future project. Unfortunately there has been no convenient room for nuclear experiments near by, the target wire for bremsstrahlung γ-ray production was obliged to be installed in a dispersive section.

At the moment, the betatron tune has been chosen to be (3.24, 1.21) and the natural chromaticity was measured to be (-5.5, -4.7), which is not compensated yet because sextupoles are not equipped in the dispersive section. Fortunately we have not observed a beam loss due to the head-tail instability within a beam current of 20 mA. We have been considering to install thin sextupoles for future development of the machine with higher beam current operation. Beam lifetime has reached

Table 1. Parameters and status of the STB ring.

Lattice type	Chasman-Green
Superperiodicity	4
Circumference	49.7 m
Maximum energy	1.2 GeV
Injection energy	0.2 GeV (nominal)
Betatron tune	(3.24, 1.21)*)
Chromaticity	(∼−5.5, ∼−4.7)*)
RF frequency	500.14 MHz
RF voltage	140 kV
Harmonics	83
Natural emittance	170 nmrad (@1.2 GeV)
Momentum compaction factor	0.0378
Dispersion	<10 cm*)
x-y coupling coefficient	0.005*)
Beam current	<20 mA*)(@1.2 GeV)
Lifetime	∼10 min (@1.2 GeV)

*) Measured value

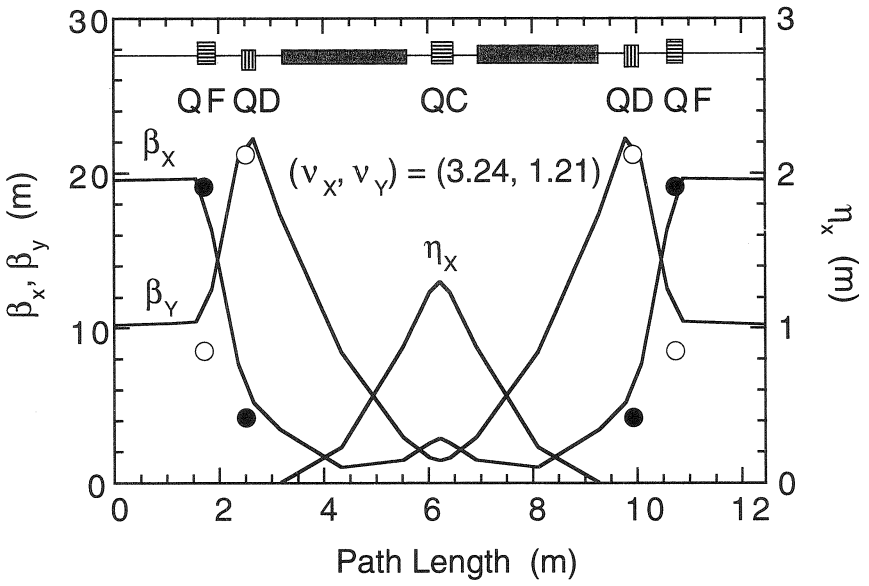

Fig.1. Lattice functions of the STB ring. Closed circle and open circle denote measured averaged horizontal and vertical betatron functions, respectively.

approximately 10 min at ∼10 mA, which is surely dominated by the vacuum pressure and has been slowly getting better.

1.2 Beam injection

The beam current from the linac beam is expected to be ∼100 mA, and the long-pulse width of 1 μs is usually employed for the beam injection into the ring. However, because of the wakefield in the accelerating structure, the energy distribution in one beam-pulse is considerably broad, so that acceptable pulse width for the STB ring is supposed to be ∼200 ns that is almost equivalent to the revolution time of the ring (166 ns). Indeed, the ring current at the injection is momentarily ∼80 mA. Because of finite energy acceptance of the RF bucket (±1.2% for 200MeV) and the multi-bunch linac

beam, the captured beam current is usually 20~30 mA.

Emittance of the linac beam in both planes has been measured to be about 300 nmrad, which seems to be sufficiently small to achieve better injection efficiency. Using 6 quadrupoles in the transport line, Twiss parameters, dispersion function and its slope at the injection point have been matched with those of the ring. Although certainty of the matching is not obvious, at present we have presumed the injection efficiency is governed by the longitudinal dynamics than the transverse one.

1.3 Operation scheme

Temporal sequence of the booster-storage mode operation is shown in Fig.2. Immediately after the beam injection, the energy ramping is started. It takes 1.1 s to accelerate the beam up to 1.2 GeV from 200 MeV, which is the maximum allowable speed of the power supply. Duration of the flat-top is on demand. In the bremsstrahlung γ-ray experiment, the event rate is controlled by the position of the target wire, and it is normally restricted by counting rate of the tagging counter array. Accordingly stable accelerated beam current is crucial for such experiments. The intensity fluctuation of the 1.2 GeV beam has been suppressed within 10% so far, which is certainly affected by operation of the injector linac

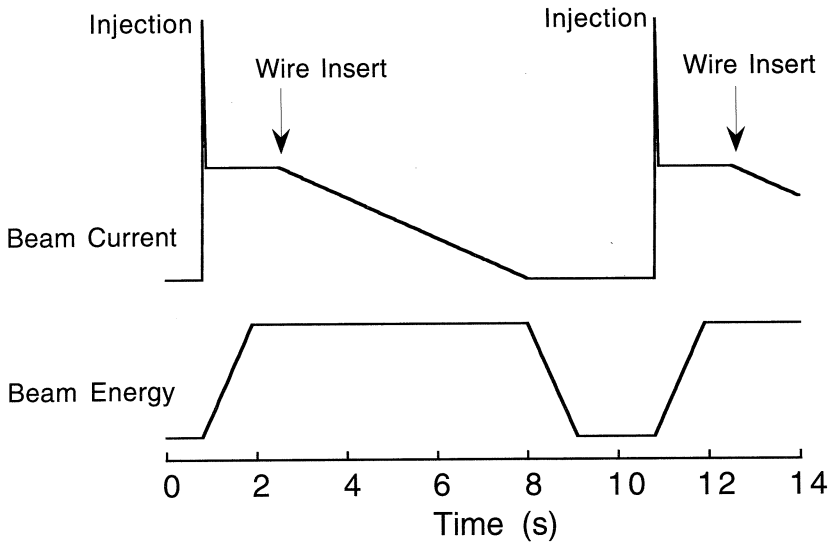

Fig.2. Temporal sequence for the experiment with the booster-storage mode of the STB ring.

§ 2. Tune Measurement by Using A Strip-Line

2.1 Measurement system

A strip-line type electrode installed in a straight section of the STB ring was designed so as to that intrinsic impedance of each strip-line 50Ω. Tune measurements are performed by which two beam signals from strip-lines of diagonal position are fed into a 180° hybrid mixer and analyzed by a real time spectrum analyzer. Betatron oscillations are excited by applying external RF dipole field to another pair of diagonal strip-lines. White noise at a certain frequency range can be used as an RF knock-out field. Accordingly betatron tunes in both plane are able to be measured simultaneously.

2.2 Stability of excitation current

In a preliminary measurement after installing the system we have observed considerable periodic tune fluctuation as shown in Fig.3. Because the chromaticity is not corrected at all, the tune signals contain the synchrotron sidebands including many harmonics. In the measurement of Fig.3, the RF voltage was much reduced to make the betatron sidebands clear. It is obvious that the tunes, particularly the vertical one, beat with 50 Hz repetition rate that corresponds to the electricity line frequency. As the lattice functions shown in Fig.1, among 3 families of quadrupole, QF and QD dominate the horizontal and the vertical betatron functions, respectively, meanwhile QC controls the dispersion function. The vertical tune shift which must be mostly arisen by instability of QD magnetic field implies a current ripple having relative amplitude of $\sim 10^{-3}$. Although the horizontal tune shift seems to be smaller and different pattern from the vertical one, it may also indicates somewhat the current instability for QF. We are going to investigate source of the current ripple in the power supplies, which would be a serious problem to improve the machine performance and precise machine control for the study of the beam physics as well.

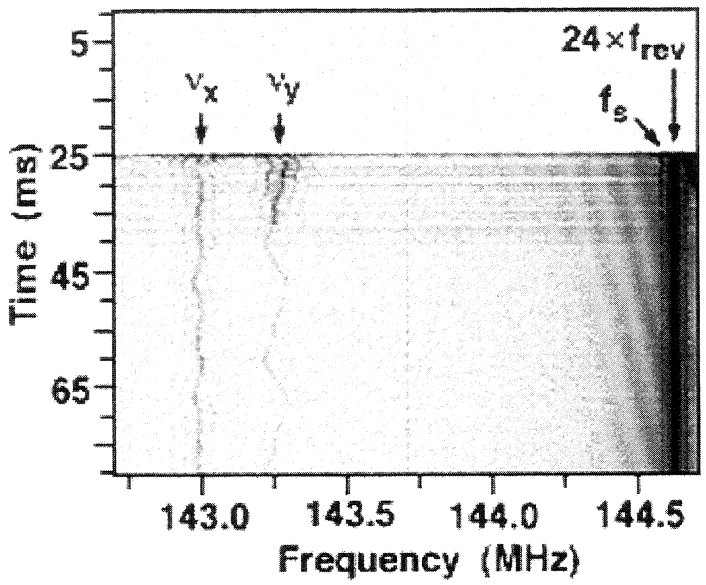

Fig.3. Tune fluctuation in a storage mode at the injection energy of 200 MeV. Betatron oscillations were excited by an external RF white noise at a frequency range of 1 ~2 MHz.

2.3 Tune shift in energy ramping

At the present, we have employed a simple pattern for excitation of the magnetic fields in the energy ramping. All magnet currents are linearly increased, but the excitation slope of the quadrupoles are bit steeper than that of the dipoles because the beam loss occurred just after the ramping started when the quadrupoles were excited with same slope as the dipoles, which was probably caused by touching integer resonance. Figure 4 shows the tune shift in an early stage of the energy ramping

Large tune shift is still seen after the ramping started. In addition it was found out that crossing of the tunes was also occurred. Specific feature is that the vertical tune is increased immediately and then decreased, meanwhile the horizontal one is getting decreased. Accordingly the tunes are crossing

each other after a couple of ms. We have noticed a considerable beam loss occurred at 2～3 ms after the ramping started. This is certainly due to the difference resonance, in which the large horizontal betatron amplitude brought by the beam injection moves to the vertical betatron motion. An average horizontal betatron amplitude produced the beam injection is expected to be $J = 7.2$ mm mrad and the damping time is much longer (～2 sec). The vertical displacement at the location of QD would reach ～20 mm that is equivalent to the vacuum chamber height, if the horizontal amplitude is fully converted to the vertical one. A half of the beam intensity is possibly lost due to the difference resonance.

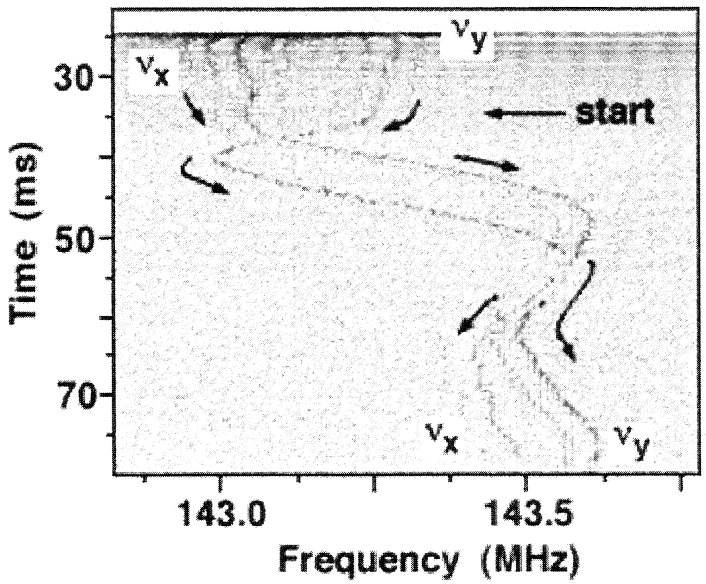

Fig.4. Tune shift in early stage of the energy ramping. The ramping is started at 10 ms after the beam injection.

As showing in Fig.5, the coupled motion at the difference resonance can be clearly seen. From the minimum distance of the tunes, the coupling coefficient is deduced to be 0.005, which is rather small value. We presume this is due to small number of the quadrupoles and no sextupoles.

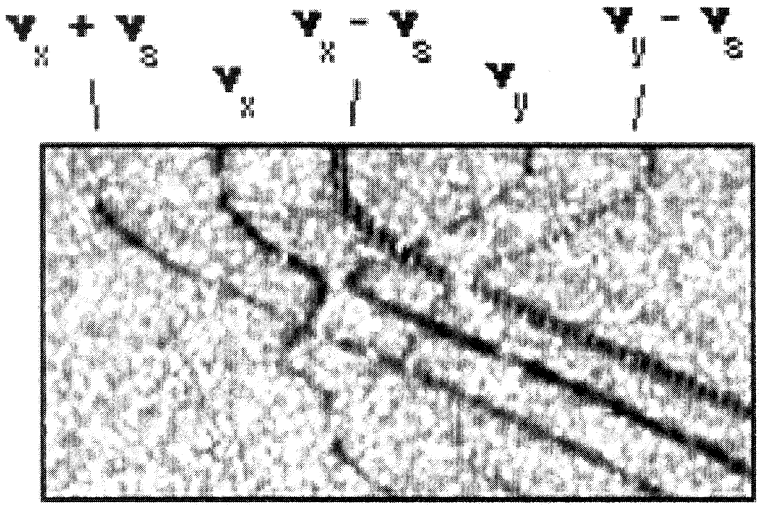

Fig.5. Observed coupled motion of the horizontal and the vertical betatron oscillations at $\nu_x - \nu_y = 2$.

§ 3. Summary

The STB ring is still commissioning stage. However characteristics of the ring has gradually become clear. Along with improvement of the stability of the power supplies, investigation of the tune shift in the energy ramping may be crucial for progress of the machine performance. Study of variation of actual magnetic field including effect of Eddy current in the ramping is under way.

References

[1] F. Hinode, *et. al.* : "*Beam Commissioning of Stretcher-Booster Ring in Tohoku University*", *Proc. 12th Symp. on Accelerator Science and Technology, RIKEN, Wako, Japan, September 1999*, p177-179.

STBリングの再レベル測量

高橋重伸

東北大学大学院理学研究科附属原子核理学研究施設
〒982-0826 宮城県仙台市太白区三神峯1-2-1

Re-surveying of Level in the STB Ring

Shigenobu Takahashi

Laboratory of Nuclear Science, Tohoku University,
Mikamine 1-2-1, Taihaku-ku, Sendai 982-0826

The level of dipole and quadrupole magnets in the STB ring has been re-surveyed several times throughout three years, starting at three years after the minute alignment in 1996. The purpose of the inspection is to investigate whether the installation of heavy apparatuses near the ring dislocates the position of the magnets. A considerable movement with a period of one year has been observed.

§1. 概　　要

STBリング（以下，リングと呼ぶ）は電子ライナックからの200MeVのパルスビームをDC化し，連続ビームによる原子核実験を行うためのストレッチャー機能と，入射ビームをＲＦ捕獲し1.2GeVまで加速させるブースタ機能，及び加速ビームを長時間保持する蓄積リングとしての機能の3つの運転モードがある〔1〕。

ライナックより入射された電子ビームは600万回/sec程度周回するので，ビームが設計CODの範囲内に入るように電磁石を設置する必要がある。1996年９月から10月初旬に精密アラインメントが行われ（以下，精密アラインメント時と呼ぶ），測量の容易性などを考慮して，リングの偏向電磁石（BM）及びQ電磁石（QC，QD，QFがあり，総称してQMと呼ぶ。）合計28台が設計許容設置精度0.1mmの範囲で設置された〔1〕。

その後，リング内には各種の電源，制御盤及び放射線シールド用コンクリートブロック（重量約350トン以上）が設置された。また，1999年７月には第２実験室北側に重量約30トンのTAG-X電磁石が搬入設置されることになったため，この電磁石搬入前の1999年６月（精密アラインメント時から３年経過），再レベル測量を行った。その後，現在まで３年間にわたり年２回程度，リングのレベル測量を行ってきたのでその測量方法，状況，データの考察，今後の課題などについて述べる。

§2. 測量機材

KEKより管理移管されたアラインメント用測量ポール（以下，測量ポールと呼ぶ）を改造して第１図のような視準高2200mmのポールを製作し，第２図のようにリング内外12箇所にわたり設置した。このポールの上部にはライカ社製レベル測量器（WILD－AN２）を固定し，且つ平行平板マイクロメーターGPM3をマウントしてある。このGPM３は上下±5mmの可動視野があり，目盛り間隔は0.1mmであるが目感でその1/10

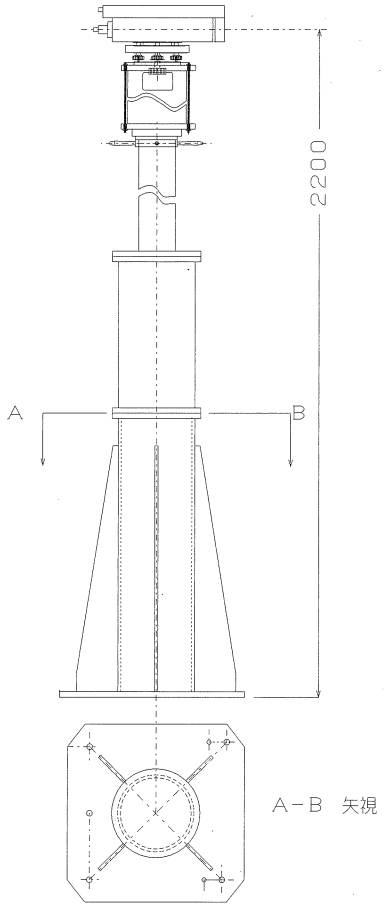

第１図　レベル測量器をマウントした測量ポール。基本部分はKEKから管理移管されたもので，2200mmの高さを視準できるように改造してある。この高さになると空調や電源送風機の風により上部が振動する。高さの割に底辺が小さいので安定性に難点がある。

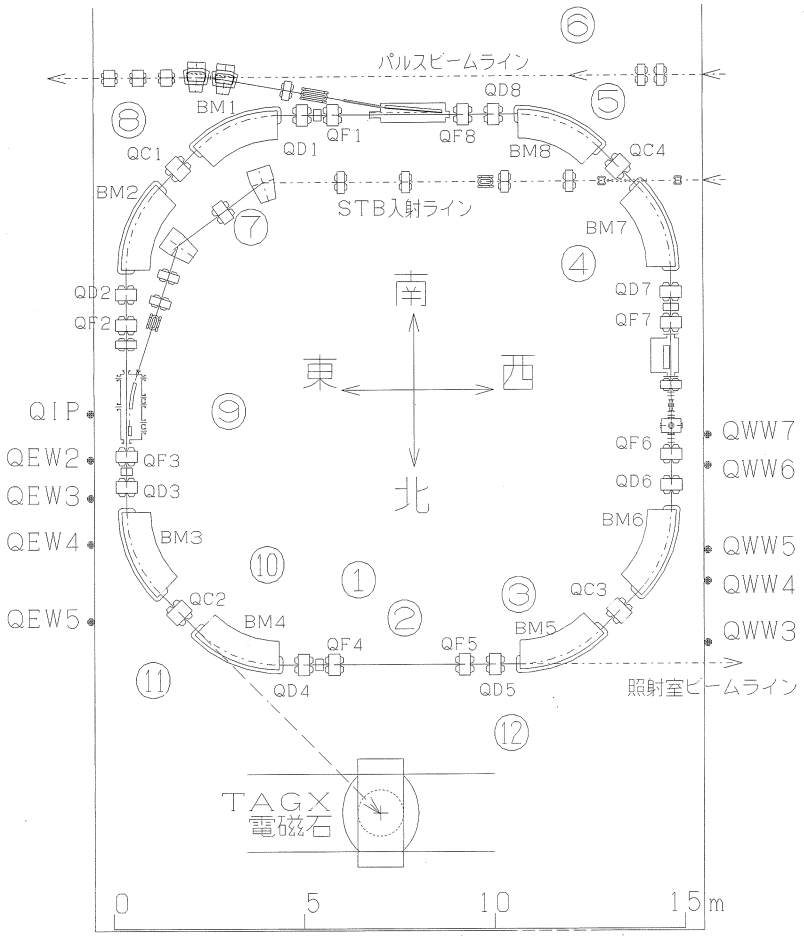

第２図　リング内外の①～⑫の位置に測量ポールを設置した。東西壁面の高さ2200mm上に貼り付けたQIP，QEW，QWWの各マーキング点の概略位置を示す。TAG－X電磁石のスケールは実際とは異なる。

（10μmオーダー）まで読み取ることができる。整準は鉛直軸自動補償装置があり，円形気泡管を表示管内の円内に合わせれば自動的に0.3秒の整準範囲に設定される構造になっている[1]。望遠鏡倍率は32倍であったが視認効率を上げるため現在は40倍にしてある。

BMの上部には３箇所，QMでは２箇所アラインメント用の整準面及び穴（径40mm）が設計ビーム中心軌道上にあけてあり，その基準穴に球面ターゲット台座を置き，その上にTaylor hobson社製の球面ターゲットを載せてレベル測量器で計測する。このターゲット台座及び球面ターゲット工作精度は10μm以下である〔1〕。

§ ３．測量方法及び状況

建設時のレベル測量基準点は東西壁に床面から約1600mmのビームライン上でマーキングしてあるが，リング内は高さが2000mm以下は各測量ポイントを見通すことができない。そのために，BMに球面ターゲットをマウントした高さ2200mmを視準高として，各測量点を複数回測量し，データを繋いで行った。

QMはBMより磁場中心- 整準面間が約166mm低いため，測量器の可動視野範囲内に両方の電磁石の測量点

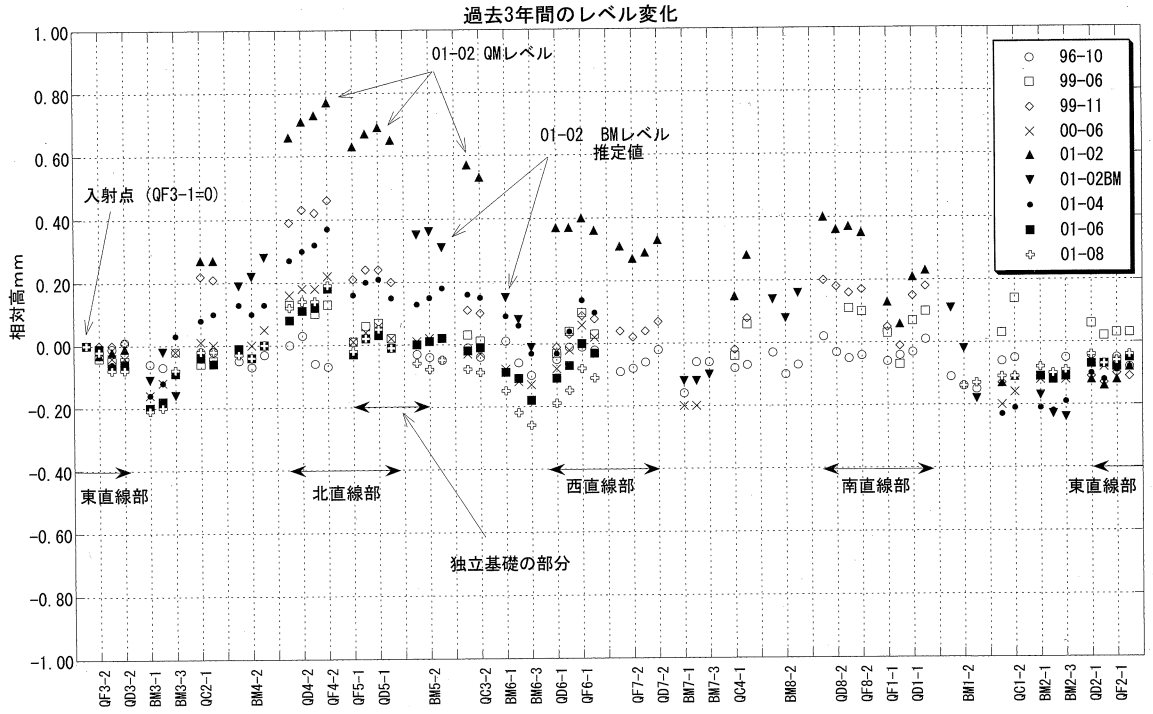

第３図　QF3-1（入射点）を原点として表したリング各電磁石のレベル変化。2001年２月期（図中，凡例の01-2参照）は最大の高低差となった。

が入るよう，円柱状の鉄製の補正棒をアラインメント用穴に差込み，この鉄棒の266mmの所にターゲットシール（以下，マーキングシールと呼ぶ）を貼ってBMと一括して測量できるようにしてある。（2000年６月期の測量からこの方法を採用した。）測量データから補正棒の長さ，ターゲットの高さ及び磁場中心―台座高間の補正値を考慮して電磁石の磁場中心を計算している。レベル測量器から最短ポイントを基準点として，各電磁石の相対高さを求めた。これまでの測量状況を以下に述べる。測量ポールの設置場所は第２図に，レベルデータは第３図に示してある。ＳＴＢ冷却水ポンプは24時間運転されており，水温は常時一定温度20±２℃に保たれている。空調温度は平日は25±１℃であるが土日，休日は運転を停止している。

1999年６月：TAG-X電磁石の搬入前にリング北側のみを測定した。測量ポールを①の場所だけに固定し，ＢＭとＱＭは高さが異なるので別々に測った。QMの変位差はほぼ±0.1mmの範囲に入っていた。建設時から３年間経過している割には変化が小さいと思った。

1999年11月：ポールの場所は①，⑥，⑧の３箇所で，これもＢＭとＱＭは別個に測量した。⑥，⑧の位置はリングの外側になるが，当時，リング内に測量ポールを設置する場所を見つけられなかったためである。QM，ＢＭどちらもそれぞれ約0.6mm程度と変位が大きくなってきていて，特にリング東側ＢＭの傾きが大きく，その時点では重量物の設置によって床面が歪んだものと考えていた。11月初旬ごろの測量データである。

2000年６月：測量日数が取れなかったため，設置場所は①の１個所だけである。ＢＭとＱＭを同時に測量した。東側の変位が非常に小さくなっている。予想に反して，リング全体のレベル変化も小さくなってきている。測量誤差によるものか，季節変動なのか，重量物搬入による影響なのかまだ判らなかった。

2001年２月：外気温による影響を調べるために気温の一番低下する時期を選び，１月下旬から２月中旬にわたってリング全周の測量を行った。気温は－1.5～７℃であった。ポール設置点は全測量点が視認出来る場所を選定し，最多の８個所となった。QMの測量時の誤差を少なくするために補正棒の使用を止め，直接台座に球面ターゲットを載せて測ったので，ＢＭとＱＭの関係がわからなくなってしまった。そこで第３図では，

2001年４月期のQD3とBM3の変位差と同じ値を２月期のBMデータ（凡例で01-02B）にセットして表示してある。実際のBM全体のレベルはもっと低下しているものと推測する。リングのレベル測量を始めてからは最大のレベル変化を示し，ＱＭの高低差だけを見ても0.8mm程度になっていた。

2001年４月：前回２月期の変位差があまりにも大きいので，電磁石の架台の変動なのか，床面の変動なのかを調査するために，東西壁にマーキングシール（壁上マーキング）を貼り付けて，BM，QMレベルとの関係を調べた。TAG-X電磁石周辺の壁面上にも貼り付けた。主に，リングの北側を中心とした測量で，この測量から以降は測量ポールの高さを変えないでBM, QMを同時測量するようなった。しかし西側壁のリング直線部の中間の位置から南の部分には，2200mmの高さ付近に口径200mmの冷却配管が７ mにわたって敷設されており，壁上マーキングを貼ることができなかった。測定ポールの設置場所は①，③，⑩の３箇所で，９回の測量を行った。気温は前回とは違い暖かで12～22℃程度であった。

2001年６月：2001年４月に貼り付けた壁上マーキングとその付近にある各電磁石とのデータ収集のために前回と同じ①，③，⑩の位置から５回の測量を行った。測量時外気温は22～28℃であった。

2001年８月：測量器の設置場所は②，③，⑨，⑩で，測量時外気温は24～31℃であった。南東壁にマーキングシールを３箇所貼り付けた。

§ ４．測定データの考察

第３図のグラフは最近３年間のレベル変動を表しているが，各年測量期の変位は1999年６月は0.2mm，同年11月には0.6mmと拡大，しかし翌2000年６月には0.2mmの変化に戻り，2001年２月期の測量では１mm程度変化し，同年４月，６月，８月では変化が次第に小さくなっている。毎年同じようなレベル変位パターンすなわち，外気温度の高い時期はレベル変位が小さくなり，低くなる冬期には大きくなる傾向があり，それもTAG-X電磁石に近いリング北側直進部周辺（BM4からBM5にかけて）に顕著にこの現象が現れている

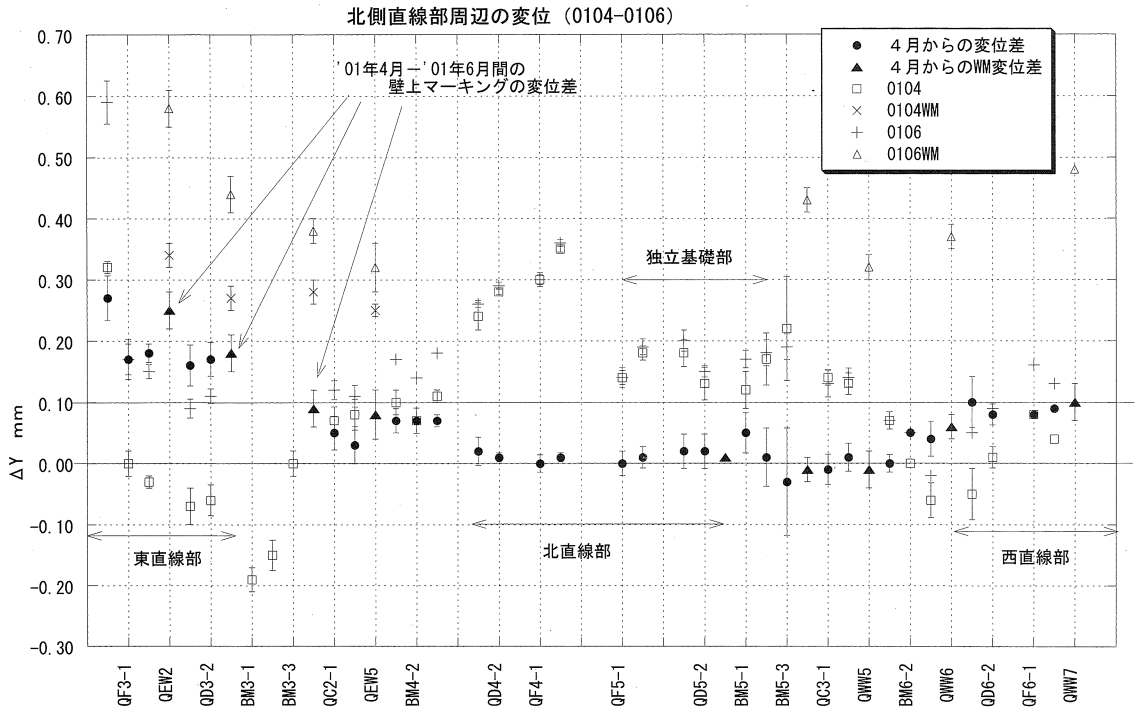

第４図　2001年４月－６月間のリング北側周辺のレベル変化。北直線部よりも東西壁周辺の変位差が大きく，特に東側が顕著で，外気温の上昇と共にレベルも高くなる。凡例のWMは壁上マーキングの意味である。

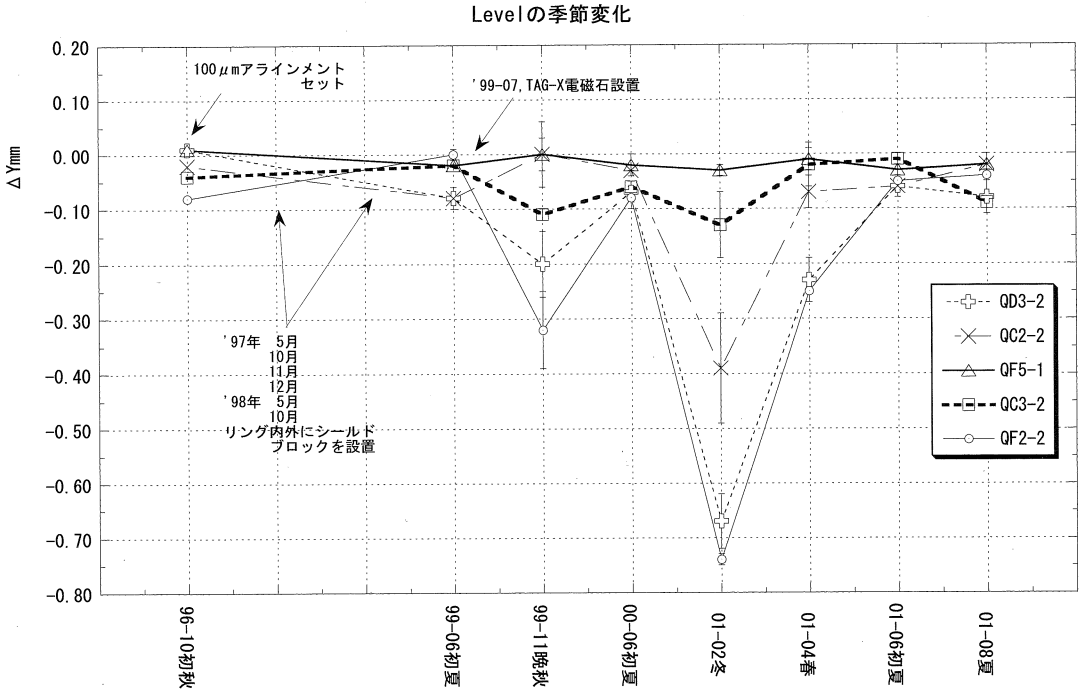

第５図　Ｑ電磁石のレベルの季節変化。夏期と冬期のレベル変位の繰り返しが毎年行われている。なお，この図は1996年10月時の入射点をゼロ(QF3-1=0)として，QF5，QD5のレベルパターンに重ね合わせた時の各Ｑ電磁石のデータである。

ように見える。しかしこのグラフはビーム入射点を基準（ここではQF3の上流側の測量点を零，QF3-1=0）として表したもので，各測量時期における電磁石のレベル変化の関連は実際とは異なる。第３図では年を追って変位が拡大しているようにも見えるが，この変位は季節変動による可能性もある。

第４図は2001年４月期と６月期のデータで，ポール設置場所は殆ど同一地点（前記測量状況参照）である。これら２つのデータは電磁石と東西壁面との関係性を調べようとしたものであるが，北側直線部にあるQD4，QF4，QF5，QD5，BM5，QC3の各電磁石及びその間のレベルを観察するとその包絡線パターンはあまり変化していないように見える。また同グラフには４月期を基準とした時の６月期のレベル変化量も示してある。ただし，測量器からの距離が近い点のレベル差が小さくなるように高さの基準を決めてある。この４月６月間の変位差は比較可能な測量点39点のうち，約８割にあたる31点が0.1mmの範囲内にあり，半数の20点が0.05mm内に入っていて，QD4からBM6に至る北西部分は，その付近の壁上マーキングも含めて変化が少ない。これに対し，QF3，QD3周辺は0.15mm以上と変化が大きくなっている。東側測量時には北東側円弧部の中心近くに測量ポールを設置した。ここからそれぞれの電磁石測量ポイントまでの距離の差は１ｍ以内であり，距離による視認誤差としてはQD3，QF3とQD4，QF4は同程度である。リング北西側のQD6，QF6の変位も多少大きくなっているが東側ほどではない。これらのデータは，実験室床面，壁及び周辺の電磁石が同期して変動していることを示していて，気候が暖かくなるにつれてリング東側，西側が上昇していく事がわかる。

第５図はＱ電磁石のレベル変化を季節毎に表した典型的な図である。精密アラインメント時データの入射点近傍の測量点を基準にして（QF3-1=0），東側から北西部分にかけての代表的な数点の変化の様子をプロットした。夏の変位は全体に小さく，４月期，11月期の過渡期を経て，２月期に東側部分の変位が非常に大きくなることがわかる。－２℃～15℃辺りまでがレベル大きく変化する気温で，次第に６月期のレベル値に戻っていく。図中には殆ど季節変動をしないQF5-1やQC3-2も表してある。１台のQMには測量点が2ヶ所あるが，

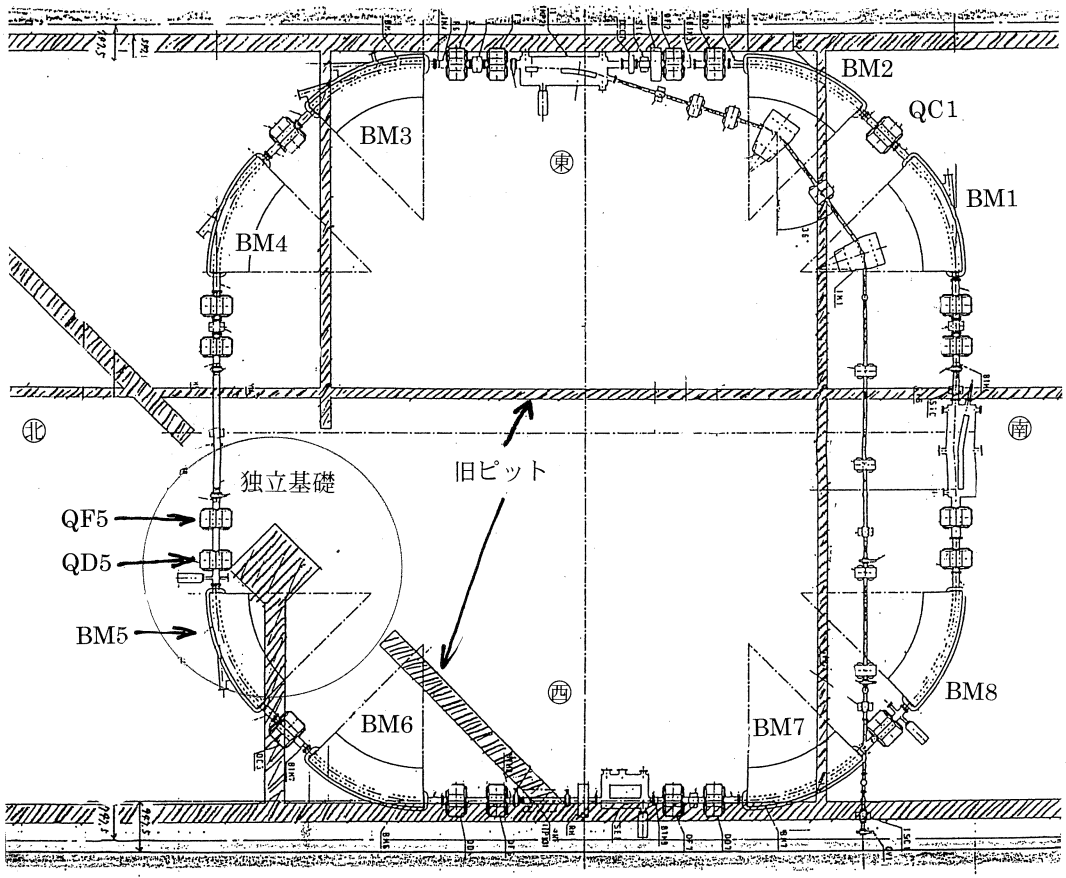

第６図　QFQD5付近の独立基礎（円内）及び旧排水ピット跡（斜線部分）。現在各ピットはコンクリートで埋められてその上にリングの各電磁石が設置されている。

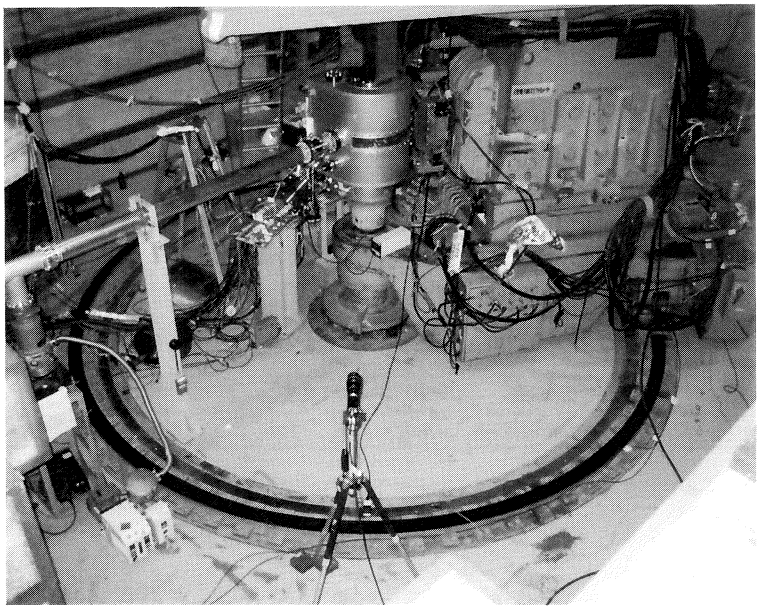

第７図　現在のLDM周辺。この基礎は半径2.6mで100トン/㎡の荷重に耐えられ，かつ実験室建屋から分離独立していて建屋からの歪の影響を受けにくい構造である[2]。当時としては厳しい設置基準で設計されている。ちなみに，LDMの重量は100トンである。

両方とも同じような変化を示す。ここで，第３図，第４図，第５図を見るとQF5，QD5のレベル値がどの測量期を見ても，10μm以内の変位差であり，レベルパターンはセット時から変化していないことが分かる。

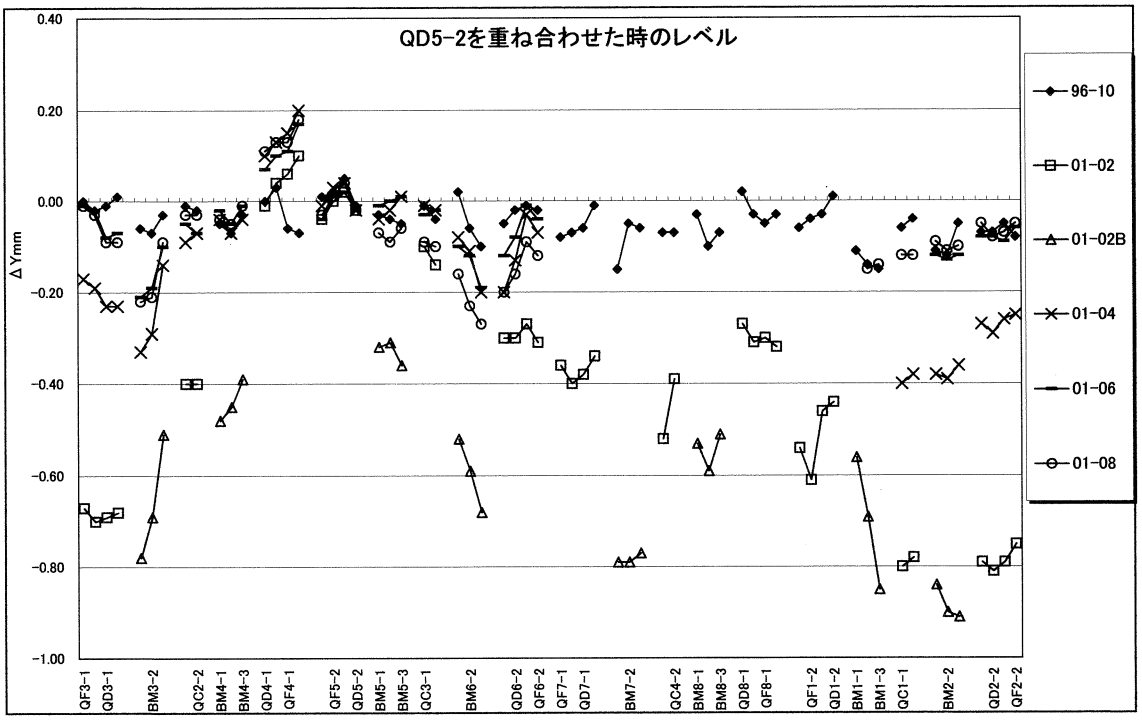

第８図　QF5，QD5を重ね合わせた時の2001年各測量期のデータ。凡例で01-02B（２月期のBMデータ）はQMとの関係がわからないため，2001年４月期のQD3-2とBM3-1間のレベル差を代入して表示してある。推定では，BMデータはもっと沈下していると思う。

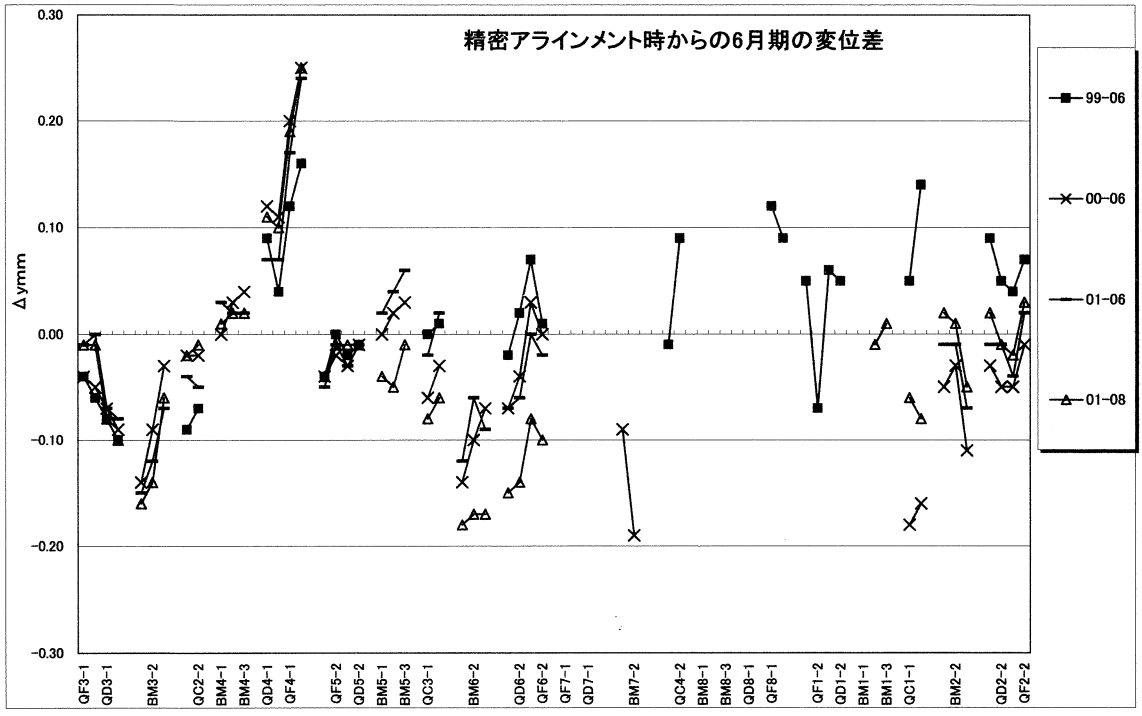

第９図　1996年10月時の精密アラインメントデータを基準として，1999年，2000年，2001年の６月期および８月期の変位差。３年間に亘り変化は現れていない。冬期の変動があっても夏期には図の位置に戻る。南西円弧部，南直線部のデータはない。QF4の盛り上がりが顕著である。Y軸スケールは±0.3mmである。

調査の結果，その原因がこれらQM床面の基礎にあることが解った。

第６図は第２実験室の旧排水ピットとSTBリングを重ねた図であるが，QF5，QD5周辺は旧中性子散乱用

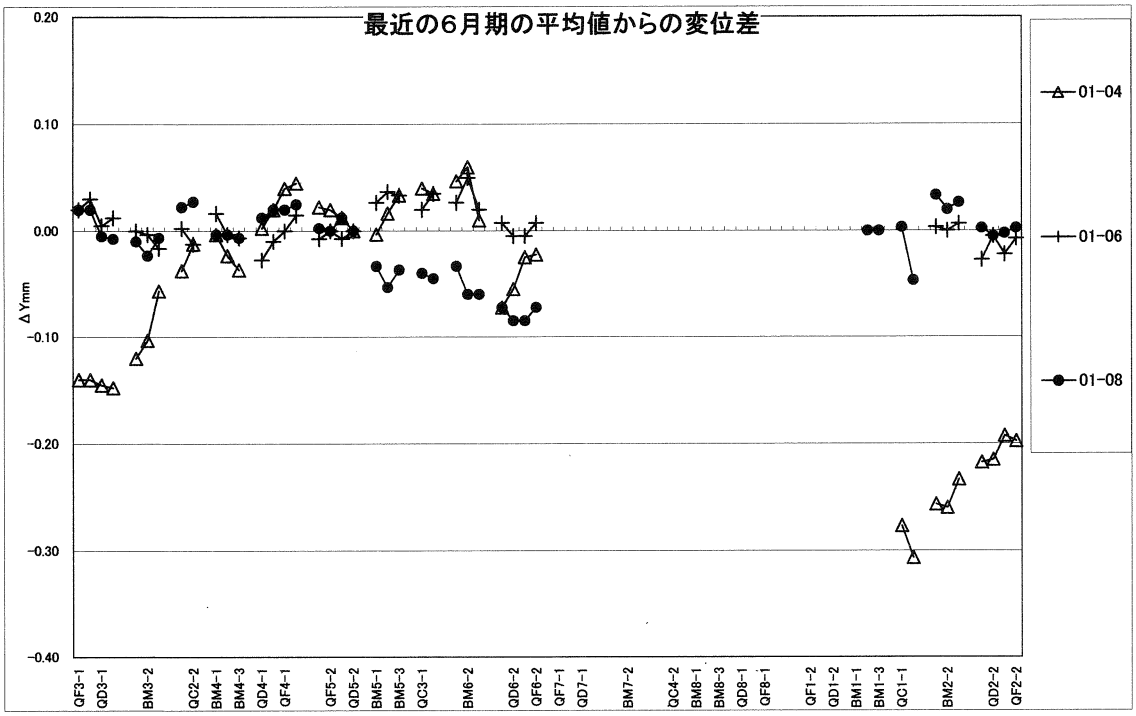

第10図　最近の６月期の平均値からの2001年４月期，６月期，８月期の変位差。４月期は東直線部から円弧部にかけて戻りの過渡期にあるが，QC2からQF6については，01.mmの範囲で元に戻っている。８月期については６月期と殆ど変わらない。

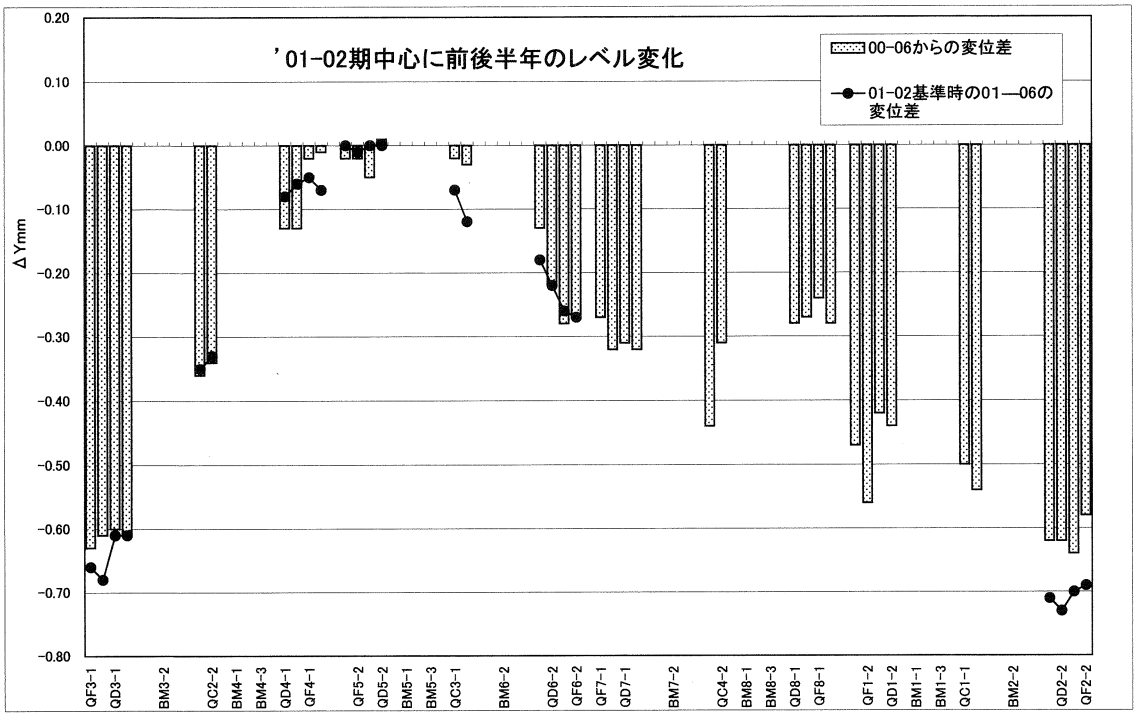

第11図　2001年２月期を中心として，６ヶ月前後におけるレベル変化。すべてのリング沈下の力が南東の方向に集まっていく様子がわかる。気温15℃以上になると，引っ張られたゴムが戻されるようにまた水平レベルに復元していく。

（ND）コンクリートトーチカの中心部があった場所で，半径2.6m内は実験室建屋から独立分離している構造で，100トン/㎡の耐荷重があることが判明した〔2〕。この部分の基礎は，LDMスペクトロメータ部分の基礎と同じである。現在のLDM周辺を第７図に示す。

以下に，精密アラインメント時のQD5-2のレベルを基準として，各測量期のデータを重ね合わせて示す。第８図に2001年２月期から８月期測量までのレベルデータを示してある。２月期のBM自身が大きく傾いているのはBM3，６，１で，中でも，BM3とBM1のレベルの傾きが約0.3mmと他のBMよりも大きい。そして，気温が上昇するにしたがって各ＢＭ間の相対レベル及びBM自身の傾きは次第に小さくなり，且つ上昇していく。他のBMの傾きは0.1mm以内に留まっている。

第９図は夏期のレベル変化に焦点を当てたもので，精密アラインメン時からの変位差を表していて，ここから1999年，2000年，2001年の６月期，８月期のデータのみを取り出し表示してある。Y軸スケールは±0.3mmである。この３年間の季節変動があっても６月期のデータのみをとって見れば，殆どの測量点が50μmのレベルエンベロープ範囲内に入ってしまう。冬期間にいくら変形しようとも夏期には元の位置に戻ることが解る。QF4が精密アラインメント時より0.25mm上昇している原因は，東床面の急峻な低下や上昇が繰り返し行われ，QF5，QD5付近の堅固に補強された独立基礎にぶつかって，そのストレスの圧力により生じたものであると考えられる。南西円弧部から南側直線部にかけては測量日程が取れなかったので比較するデータはない。各測量期のポール設置場所が異なるが，第3図の①の場所（QF4の近くでリング内の位置）からの測定は，どの期でも行っているのでその部分を中心に比較していただきたい。QF5，QD5の床面の安定性がわかる。

第10図は最近の６月期の平均値からの2001年４月，６月，８月期測量データの変位差を表している。これによると，４月期にはQC2からQF6は６月期の平均値の状態にほぼ戻り，８月期には全ての電磁石が平均値から0.1mmの範囲内に入ってる。第11図は2001年２月期を中心に，前後半年のデータを比較したもので変位の戻りはほぼ同じ量である。リングを沈下させている力の源がBM2付近にあることが解る。

§ ５．建て屋及び地盤からの考察

第２実験室は硬い凝灰岩の岩盤を削り取って安定した地盤の上に建設され，LDMとQF5，QD5付近の基礎部分を除き，耐荷重は10トン/㎡で設計されている〔2〕。第２実験室断面図を第12図に示す。実験室は半地階構造で，約３分の２が地下にあり，地上部側面は掘削した残土で土盛りされている〔2〕。天井（屋上）のみ直射日光があたるが，外気からの影響を受けにくい構造である。しかし，東側にはリングビームラインと同

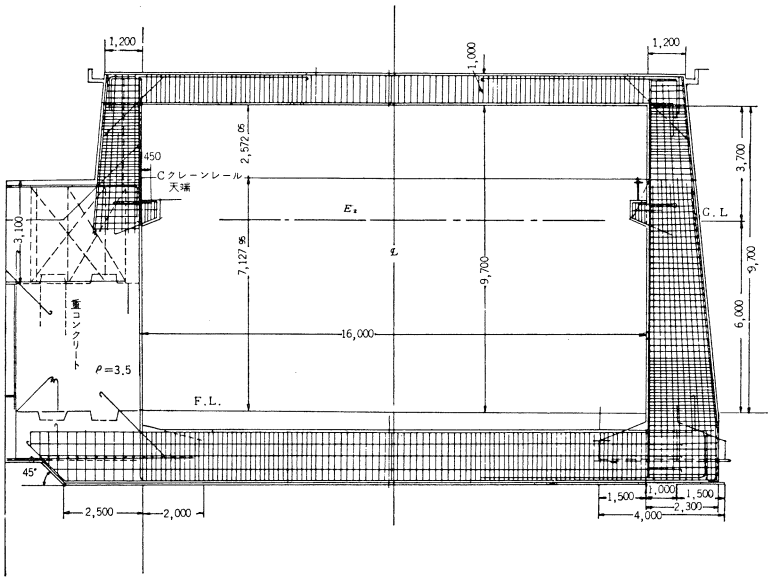

第12図　第２実験室の躯体構造の断面図。設計耐荷重は10トン/㎡。

一レベルにビーム輸送系を確保するため，実験室と連結して地下にビーム偏向室並びに偏向室搬入口がリングと同時期に建設されている。この偏向室は旧TOFトンネル及び副標的室を拡張したもので，基礎は岩盤まで掘り下げてはいないし，また，第２実験室のようなきびしい耐荷重設計もしてはいない。東側地盤については，亜炭採掘跡が南北に走っており，断層が偏向室付近にある〔2〕。当時の報告では，湧水の影響はなかったとある〔2〕。第２実験室北側にもSTB電源棟が作られたが地上階であり搬入口がその間にあり影響は少ない，また西側の地下部分は３m近い重コンクリートで隔てられて第２電磁石室と繋がっている。リング用冷却水配管を敷設したが実験室地上部の土盛り部分のみを工事したにすぎず，南側は分岐階段及び第２空調室へ繋がっていて何ら変更はしていない。

ビーム偏向室，偏向室搬入口，廃棄物倉庫に至る通路及び５系ビーム輸送系（旧TOFトンネル）は２実験室から枝のように東側に突き出て繋がっており，偏向室搬入口は扉で仕切られているが屋根は密閉してはいない。偏向室の温度，湿度はそれぞれ2001年２月は16～18℃，40％，2001年７月８月は24℃，80％で，急激に変化するような事はなく，1℃/日程度の温湿度変化である。また，この通路及び5系ビーム輸送系には排気口が何箇所か設置されていたが，現在，第２実験室側は蓋が付けられていて空気の出入りはない。第２実験室の許容耐荷重量は床面積から約5000トンである。LDM重量が100トンあり，シールド用コンクリートブロックやTAG-Xおよびペア電磁石などの重量物が400トン，STBリングは電源を含めて少なく見積もっても200トンとなり，合計700トンとなる。本報告の最大の懸念事項である重量物設置による顕著な影響については，現在表れていない。その理由として，毎年６月期にはレベルが元の位置に戻ることと，TAG-XおよびペアQF4電磁石に一番近い場所にあるが逆に盛り上がっていることが あげられる。第２実験室を沈下上昇させている原因の一つに気温の変化があることは前述したとおりであるが，それがどの様なメカニズムで実験室に作用しているのかの根本原因を調べるには，建築や土木工学からの解明が必要になってくるので，本報告ではこれ以上の議論は行わない。

ビーム運転の面から言えば，これまではSTBリングの立ち上げの都度，COD補正を行っており，また長期間に渡って同一のベータトロン動作点で運転していないことから，このレベルの季節変動が周回ビーム軌道に与える影響は明確になっていない。またレベルの変動は取り出しビームのエミッタンスを変化させることが予想されるが，現在のところSTBリングにおいては電源リップルによる電磁石磁場の不安定性や入射ビームの光学パラメータの適合などの問題が支配的であり，直接的なレベル変動の影響を感知していない。しかし，STBリング周回ビームの質の向上や取り出し電流の安定な増加を図るためにも，リアルタイムレベルデータ収集の構築が望まれる。

§ 6．今後の課題及び所感

1）リング全周にわたるポイント（ＢＭ：24点，ＱＭ：40点，その他必要とされる周辺の壁上マーキング）を測量するためには，100kg程度の重い測量用ポールをクレーンで10数箇所移動して固定する必要がある。これは，移動や設置のときに電磁石や真空ダクト等にぶつけないよう注意しながら行う作業で，測量視界確保のため，シールドブロックの移動に加えて，各種制御盤筐体やBM用吊り金具部品の取り外しが必要で，実質の測量時間よりもその準備のための時間のほうが極端に長くなってくる。測量時間や日数が長くなると疲労による視認誤差，測量ポールやレベル機器の整準変動，被測量物の温度変化による誤差等が入ってくる。現在，安価で短時間に且つリング運転時でもリアルタイムにレベル測量ができる方法を検討中である。

2）レベル最短合焦点距離が1.6mなので設置場所が限定される時には至近距離の測量ポイントが見えない。

3）測量データのには，測定時間帯（外気温度の変化），測量場所，室温（空調の有無），天井クレーン使用の有無など，様々な測定条件が異なっていることに起因する誤差が存在するので，出来るだけ測定条件を一定に保たなければならないが，日程が取れないときには上記条件を無視して測量することもあった。

4）前述の測量機材で短時間に，且つ誤差を小さくするためには，ビーム軌道レベルからあまり離れない位置に，リング設計時から再測量用の空間を設け，例えばリング中心を基準点として，そこから放射状に，測量ポイントまで空間を空けて置き，その場所には物を置かないよう物理的に確保しておく措置をしておけば，測量機器から各電磁石の測量ポイントまで殆ど同一距離にあるので作業効率は上がり，信頼性の高いデータを得る事が出来る。ただ，測量基準点の条件としては地盤を強固にするなど，周辺環境から影響を受けにくい構造にする必要がある。

5）レベルデータは長期にわたる観測をしていかないと変化が現れてこないので，定期的なレベル測量を行い，ビームに与える影響を調査していきたいと考えている。

謝　辞

本報告は玉江忠明氏，日出富士雄氏，七尾晶士氏，院生の田中拓海氏，ならびにKEK　ATFアラインメントグループの方々のご協力，ご助言によるもので深く感謝いたします。

参　考　文　献

[1]　井上　隆：修士論文「ストレッチャーブースタリングの精密アラインメント」。

[2]　三菱電機技報　Vol. 42. 1968。

Prebunched Free Electron Laser Based on Coherent Transition Radiation

S. Sasaki[1],Y. Shibata[1], K. Ishi[1], T. Tsutaya[1], T. Ohsaka[1],
F. Hinode[2], T. Matsuyama[2], M. Oyamada[2] and Y. Kondo[3]

[1]*Research Institute for Scientific Measurements, Tohoku University, Katahira, Sendai 980-8577*
[2]*Laboratory of Nuclear Science, Tohoku University, Mikamine, Sendai 982-0826*
[3]*Graduate School of Engineering, Tohoku University, Aramaki-aoba, Sendai 980-8579*

In an open resonator, the wave packets of coherent transition radiation (TR) emitted from a short-bunch beam of electrons of a linear accelerator have been superposed on the subsequent bunches to stimulate coherent TR. The main mode in the resonator has been assigned as TEM_{01}. The output of the resonator has been confirmed to be amplified due to the stimulated emission, compared with the coherent spontaneous TR generated within the resonator.

§ 1. Introduction

The free electron laser (FEL) is an intense and monochromatic source of radiation. Until now many types of tunable FEL's have been developed by using the undulator [1]. The intense radiation of the FEL is due to the coherent radiation emitted from modulated electrons of the order of wavelength in the electron distribution caused from interaction of the electromagnetic wave and the electrons in the undulator [2].

In the long wavelength region, high-power waveguide FEL or FEM has been developed using short-bunch beams of electrons of linear accelerator [3-7]. The advantage of the utilization of the prebunched beam has been discussed from the point to make short the time duration for lasing to growing up to saturation. However, the role of the prebunched beam is not limited to the shortening of the growing up time. The prebunched electrons contribute to the amplification of radiation in the resonator.

Using a short-bunch beam of electrons of a linear accelerator, the coherent radiation from the bunch is also emitted in the region where the wavelength is near to or longer than the size of the bunch [8-11].

In several experiments on the prebunched FEL the coherent radiation was stored in a resonator [12-16]. The wavepackets of coherent radiation go back and forth in the resonator, and superpose on the subsequent bunches to stimulate the coherent radiation. From the linear accelerator, the bunches are successively ejected at the interval of the radio frequency (RF) of acceleration. The wavepackets generated from the successive bunches interfere coherently with each other [17, 18]. Consequently the output radiation has a quasi-continuous broad-band spectrum composed of a series of line spectra whose frequencies are higher harmonics of the RF of the accelerator.

In the prebunched FEL, as described above the amplification of the radiation is caused from the following two process. One is the usual process in FEL, namely bunching process. The interaction of

radiation and electrons in the resonator makes modulation in the electron distribution. The role of the initial short-bunch is the seed of the modulation which forwards the growth of the modulation in a bunch. The other is the following process, which will be called superposing process in this paper. The electric fields of the radiation from successive bunches are superposed coherently in the resonator. In consequence of the superposition, the output radiation is amplified, since the intensity is given by square of the total electric field.

The weight of the two processes on the amplification depends on the ratio of the wavelength to the longitudinal bunch length. In case of a relatively long bunch, for example, the bunching process is important. The waveguide FEL has been studied experimentally [3-7, 19, 20] and theoretically [21-25] from this view point.

On the other hand, in case of the ideally short-bunch beam where the bunch is much less than the wavelength in size, the bunching process has no importance but the superposing process will be effective and amplify the output radiation. However, the experiment on the superposing process was few and the theory is limited to the ideal case [26]. When the electrons are well bunched, the spontaneous coherent radiation itself emitted from the bunch is coherent and drastically enhanced compared with the ordinary incoherent radiation [9-11]. The amplification of radiation due to the superposing process hence will be not so drastic as that of the bunching process.

The purpose of this work is to show the amplification due to the superposing process. When the optical axis of an open resonator is placed along the trajectory of the electron beam, the beam passes through the upstream mirror to emit forward TR and through the downstream mirror to emit backward TR in the resonator. The electric vectors of the forward TR and the backward TR are axially symmetric with respect to the trajectory of the electron beam. Since the velocity of the electrons has no transverse component, the product term of the velocity of the electrons and the electric field of the radiation in the resonator has no importance and results in that the bunching process is negligibly small. Therefore if the amplification of the TR is observed in the resonator, the amplification shows direct evidence of the superposing process in the prebunched FEL.

Previously, similar trial has been reported by Lihn *et al.* [27]. However, they did not show clear evidence of the stimulated emission of the TR.

§ 2. Simple theory of Prebunched FEL : Superposing process

2.1 one dimensional model

Here, we consider a simplified case that the bunch train of the electron beam passes through normally the resonator composed of the two plane parallel mirrors with infinite size. The amplitude reflectivity of the one mirror of the resonator is assumed to be 100% and that of the another mirror is γ ; the transmittance of the mirror is $\sqrt{1-\gamma^2}$. Let the trajectory of the beam be z-axis, and we assume that the wavepacket of the coherent TR emitted from the bunch is well approximated by the electric impulse $a_0(t)$ whose temporal structure is similar to the density distribution of electrons in the bunch. Then the train of the wavepackets emitted from N_b bunches is given by a function of time,

$$a(t) = \sum_{i=0}^{N_b-1} a_0(t - \Delta t), \tag{1}$$

where Δt stands for time interval between successive bunches, and written as $\Delta t \mid = 1/\nu_{RF} = 2\pi/\omega_{RF}$, using the radio frequency (ν_{RF}) of the linac. The output of the resonator is given by the following series,

$$a(t) = \sqrt{1-r^2} \sum_{i=0}^{N_b-1} \sum_{n=0}^{\infty} r^n a_0[t - (i\Delta t + nT_0)], \tag{2}$$

where T_0 is the time interval for the wavepacket to trip around the resonator.

The spectral Intensity of the output radiation $W(\omega)$ is given by Fourier transform of Eq. (2).

$$\begin{aligned} W(\omega) &= \left| \frac{1}{2\pi} \int_{-\infty}^{\infty} a(t) \exp(-i\omega t) dt \right|^2 \\ &= \left| a_0(\omega) \frac{\sqrt{1-r^2}}{1 - r\exp(-i\omega T_0)} \frac{1 - \exp(-i\omega N_b \Delta t)}{1 - \exp(-i\omega \Delta t)} \right|^2 \\ &= W_0(\omega) \frac{1-r^2}{1 - 2r\cos(\omega T_0) + r^2} \frac{\sin^2(N_b \omega \Delta t/2)}{\sin^2(\omega \Delta t/2)}, \end{aligned} \tag{3}$$

where $W_0(\omega) = \mid a_0(\omega) \mid^2$ is the intensity of the radiation emitted from the single bunch. The second factor shows effect of open resonator, and the third factor stands for the effect of the bunch train. As a function of ω the third factor oscillates rapidly with increase of N_b. When we measure spectrum with a high resolution spectrometer, the third factor reduces to delta function, under the condition that $N_b \gg 1$.

$$\frac{\sin^2(N_b \omega \Delta t/2)}{\sin^2(\omega \Delta t/2)} = \sum_{j=1}^{\infty} N_b \omega_{RF} \, \delta(\omega - j\,\omega_{RF}), \tag{4}$$

This shows that only the higher harmonics of the radio frequency of the accelerator is stored in the resonator. Hereafter we replace the third factor by Eq. (4), even though the resolution of our measuring system was insufficient to resolve the higher harmonics of the accelerator frequency.

The second factor of Eq. (3) also oscillates as functions of ω and the length of the resonator L, and becomes maximum at the resonance condition; $\omega T_0 = 2K\pi$ for integer K. In the plane parallel resonator with the infinite mirror size, $T_0 = 2L/c$ where c is the light velocity in vacuum. Therefore, when the length of the resonator is so adjusted to satisfy the condition that the ratio $T_0/\Delta t$ is integer, Eq. (3) becomes maximum and the output intensity is written by,

$$W(\omega) = W_0(\omega) \frac{1+r}{1-r} \sum_{j=1}^{\infty} N_b \omega_{RF} \, \delta(\omega - j\,\omega_{RF}). \tag{5}$$

Without the resonator, if the train of the wavepackets of Eq. (1) is detected coherently, the radiation intensity is also calculated from Fourier transform of Eq. (1) and is written by,

$$W(\omega)|_{train} = W_0(\omega) \sum_{m=1}^{\infty} N_b \omega_{RF}\, \delta(\omega - m\omega_{RF}). \tag{6}$$

The comparison of Eq. (6) with Eq. (5) shows that the output radiation of the resonator is enhanced by the factor $(1+\gamma)/(1-\gamma)$. This shows the essence of the amplification due to the superposing process. If we introduce a train of light pulse, which is generated outside of the resonator, into the open resonator, it is impossible to amplify the radiation; no energy is generated in the resonator. In the prebunched FEL, on the other hand, the electric impulse of the coherent radiation is generated in the resonator and the electron bunches can produce the energy corresponding to stimulated emission of the radiation.

2.2 Semi-confocal resonator

In the above section, we assumed the plane-parallel resonator of the infinite mirror size. However, in experiment the size of the mirrors is limited, and the time interval which trips around the resonator depends on the cavity modes allowed in the resonator.

In this work, we prepared a semi-confocal type resonator, in which the cavity modes have been well studied. When the train of the wavepackets is generated in the resonator, the output intensity is given by

$$W(\omega) = W_0(\omega) G(m,n) \sum_{j=1}^{\infty} N_b \omega_{RF}\, \delta(\omega - j\,\omega_{RF}), \tag{7}$$

$$G(m,n) = \sum_{mode} G_{mn} = \sum_{mode} \frac{1 - r_{mn}^2}{1 - 2r_{mn}\cos(4\pi L/\lambda - \Delta\varphi_{mn}) - r_{mn}^2}, \tag{8}$$

where r_{mn} and $\Delta\phi_{mn}$ are the reflectivity and the phase of the TEM_{mn} mode, respectively. Both r_{mn} and $\Delta\phi_{mn}$ were obtained from the solution of the eigen value problem derived from the Fresnel-Kirchhoff diffraction integral.

When the resonant condition, $\cos(4\pi L/\lambda - \Delta\phi_{mn}) = 1$, is fulfilled, the factor of Eq. (8) takes the maximum value, $G_{mn} = (1+r_{mn})/(1-r_{mn})$. Since every modes have their own eigenvalues $\Delta\phi_{mn}$, the cavity length which satisfies the resonant condition is different from mode to mode.

§ 3. Experiment

The experiment was carried out using the S-band linear accelerator of the Laboratory of Nuclear Science, Tohoku University. The experimental setup is schematically shown in Fig.1. A short-bunch beam of electrons of 150 MeV passed through an open resonator of the semi-confocal type composed of three mirrors M1, M2 and M3 as shown in Fig.1.

The aluminum evaporated mirror M1 of glass was a round concave mirror of ϕ 100 mm in diameter with the focal length 440 mm. The mirror M2 was an aluminum-evaporated plane mirror of 12 μm-thick Mylar sheet with ϕ 130 mm in diameter and M3 was also a plane mirror of fused quartz with 130 mm $\times$ 1 mm in diameter and thickness. The central part of 25 mm in diameter of the mirror M3 was

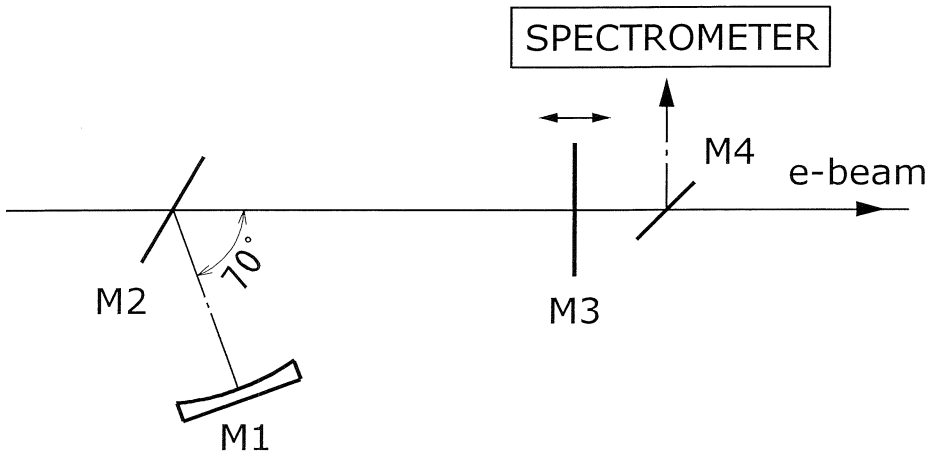

Fig.1. Schematic layout of the experiment. M1: concave mirror; M2-M4 : plane mirrors. The semi-confocal resonator was composed of the mirrors M1 and M3. The output of the resonator was extracted from a semi transparent window of M3. The trajectory of the electron beam is shown by the straight line.

semi-transparent, and the radiation out of the resonator was extracted through the semi-transparent window.

In this experiment, as the mirror M3 we prepared two mirrors, M3 (0.85R) and M3 (0.21R), whose reflectivity of the semi-transparent window is different with each other; the power reflectivity and transmittance of the semi-transparent window of M3 (0.85R) were measured with a far-infrared interferometer to be 0.85 and 0.016 at $\lambda = 1$ mm, respectively, and those of the mirror M3 (0.21R) were measured to be 0.21 and 0.79. The window of M3 (0.21R) was not coated and had no absorption. On the other hand, the window of M3 (0.85R) was coated with thin gold layer and showed absorption.

The length of the resonator between M1 and M3 was set to 420 mm, 4 times of the inter-bunch distance, and was controlled with a stepping motor to change in length. The distance between M1 and M2 was 80 mm, and the electron beam passed through the centers of M2 and M3.

The radiation out of the resonator was reflected by the plane mirror M4 of an aluminum-coated fused quartz to a far-infrared spectrometer of grating type, and the acceptance angle of the measuring system was 70 mrad. The radiation was detected with a liquid-helium-cooled Si bolometer.

The conditions of the electron beam were as follows. The RF was 2856 MHz, and the energy and its spread were 150 MeV and 2 %. The duration of a macropulse was 1.5 μs and its repetition was 16.67 Hz. The average beam current was typically 1.5 μA. Hence the one macropulse was composed of about 4280 bunches, and the average number of electrons in the bunch was 1.3×10^8. The transverse cross section of the beam was nearly circular and was about 5 mm in diameter at the position 50 cm upstream from M2.

Previously, from the analysis of the spectrum of coherent radiation, we derived several times the longitudinal bunch length of the electron beam of the linac. The results showed the bunch length was about 0.3 mm or 1 ps [10, 11, 28]. The operational conditions of the electron beam of the present work was the same as those of the previous experiments. Therefore the bunch length of the present work is considered to be about 1 ps and sufficiently shorter than the wavelength observed.

The output intensity of the resonator frequently showed fluctuation caused from the fluctuation

in the electron beam. The fluctuation was corrected as follows. At about 1.2 m downstream from M4, we placed a 15 μm thick aluminum foil mirror to emit coherent TR to the direction perpendicular to the beam. The TR was detected with another Si bolometer and the fluctuation of the intensity was used to correct the fluctuation in the resonator output.

§ 4. Results

4.1 Detuning curve

We observed the detuning curve, i.e. the variation of the output intensity of the resonator as a function of the cavity length L at λ = 0.8, 1.25, 1.6 and 2.5 mm, using the mirror M3 (0.85R). The results are shown in Fig.2.

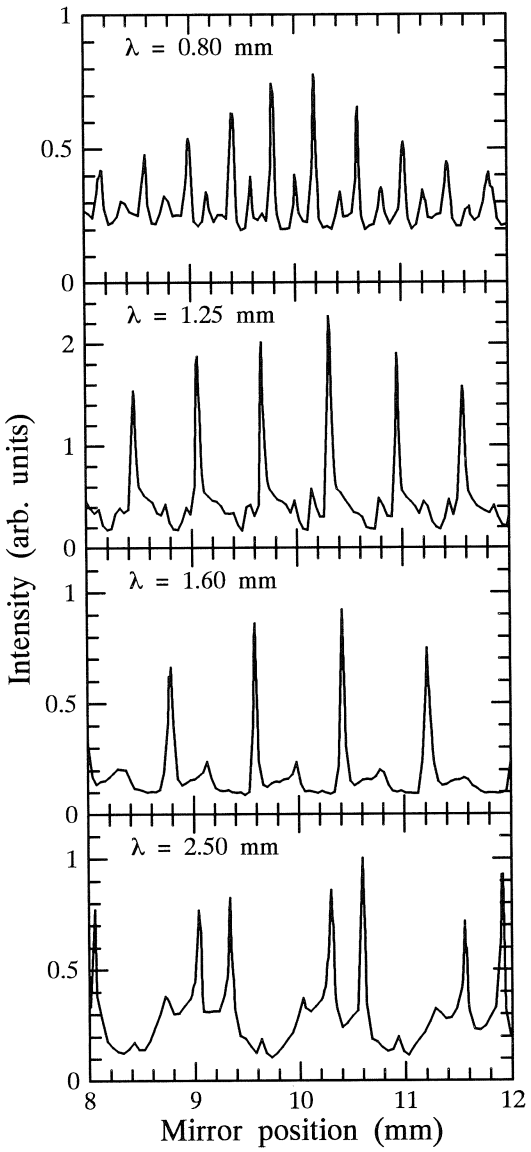

Fig.2. Detuning curve observed as a function of the cavity length at the wavelength of λ = 0.8, 1.25, 1.6 and 2.5 mm (from top to bottom) for the resonator with M3 (0.85R).

The detuning curve shows a periodic structure with the period of $\lambda/2$. The periodic structure is in accordance with Eq. (8). Each structure has a main peak and a few sub-peaks. The main peak has the

maximum value where the resonant condition, $\cos(4\pi L/\lambda - \Delta\phi_{mn}) = 1$, is satisfied.

Since the cavity length L corresponding to the maximum peak is known from the position of M3, we can derive $\Delta\phi_{mn}$ for the wavelength observed. The results are as follows, $\Delta\phi_{mn} = 180^\circ$, 181°, 189° and 173° for $\lambda = 0.8$, 1.25, 1.6 and 2.5 mm, respectively.

We assigned the main mode as TEM_{01} mode. The reason is that, in the case of the semi-confocal resonator, TEM_{01} mode has the phase $\Delta\phi_{01}$ of 180°. In addition the radiation field of TR is axially symmetric with respect to the trajectory of the electron beam and is null on the trajectory. The radiation pattern of TR is hence consistent with the TEM_{01} mode.

The phase factor $\Delta\phi_{mn}$ increases with the numbers m and n. At $\lambda = 2.5$ mm the secondary peak is shown at the resonator length about $\lambda/8$ shorter than the main peak. The secondary peak is hence assigned as TEM_{00} mode.

The quality factor Q_{mn} of the main mode was obtained from the width of the maximum peak. Since FWHM (full width at the half maximum) Δx is related to the reflectivity r_{mn} from Eq. (8)

$$Q_{mn} = -\frac{2\pi}{\ln r_{mn}}, \tag{9}$$

$$r_{mn} = 2 - \cos(2\pi\Delta x/\lambda) - \{[2 - \cos(2\pi\Delta x/\lambda)]^2 - 1\}^{1/2}. \tag{10}$$

The quality factor of the main mode TEM_{01} was derived from the detuning curve as, $Q_{01} = 23$, 35, 51, and 48 or $r_{01} = 0.758$, 0.837, 0.884, and 0.877 for $\lambda = 0.8$, 1.25, 1.6, and 2.5 mm, respectively. The quality factor decreases as the wavelength decreases. This may be caused from the output window. Since the radiation field of the TEM_{01} mode is expanded over the window with the increase of wavelength, the fraction of the radiation passing through the window decreases with the increase of the wavelength. This will result in the increase of Q_{01} with the wavelength.

In the experimental setup of Fig.1, the electron beam passed through the mirrors M3 and M4, and the forward TR emitted from M3 and the backward TR from M4 were also guided to the measuring system. Both the output of the resonator and the coherent TR emitted downstream of the resonator were observed together. The detuning curve in Fig.2 shows that the observed intensity is composed of modulated intensity due to variation in the cavity length and radiation intensity without the modulation. The latter is mainly caused from the coherent TR downstream of the resonator.

In the experiment we replaced the mirror M3 (0.85) with M3 (0.21), and observed detuning curve. The results at $\lambda = 0.8$, 1.25, and 1.6 mm are shown in Fig.3. The main mode is also TEM_{01} mode. In comparison with the case of M3 (0.85), however, the peak width is relatively wide. The quality factor has been derived as, $Q_{01} = 26$ and 25 for $\lambda = 1.25$ and 1.6 mm respectively. The value of the quality factor is smaller than those of M3 (0.85). This is caused from the low quality of the resonator. At $\lambda = 0.8$ mm, the main peak and the secondary peak merge into a broad peak.

The base line of the detuning curve in Fig.3 is higher than that in Fig.2. This is partly caused from the low reflectivity of the output window of M3 ; relatively high fraction of the forward TR emitted from M2 directly passed through the window without intensity modulation due to the variation in the cavity length.

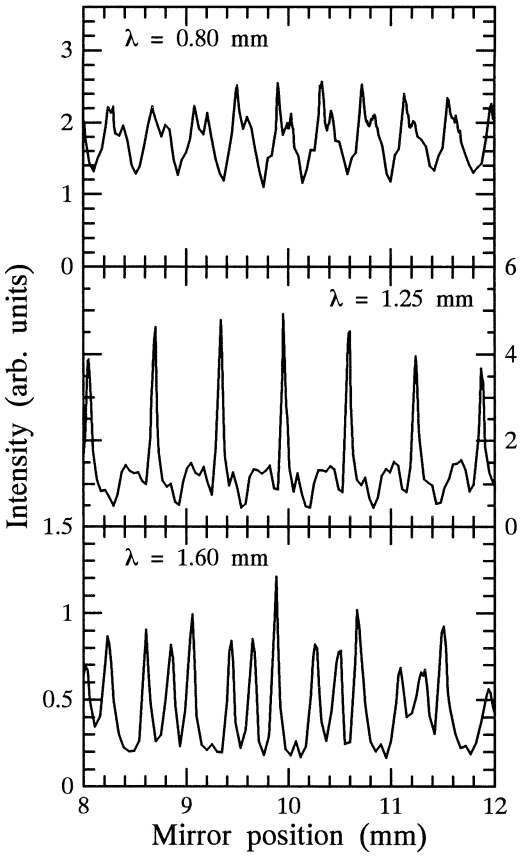

Fig.3. Detuning curve observed as a function of the cavity length at the wavelength of λ = 0.8, 1.25, and 1.6 mm (from top to bottom) for the resonator with M3 (0.21R).

4.2 Dependence of the output on beam current

At the maximum peak of the detuning curve in Fig.2, we measured the dependence of the radiation intensity on the beam current. The Tohoku linac has equipped with a current-control slit in the beam transport system between the linac and the experimental room. By controlling the slit width, we can alter the beam current without change in the operational condition of the electron beam.

The open circles in Fig.4 show the result observed at λ = 2.5 mm. The straight line was determined by the least-squares method to fit all the data, and it has the slope of 2.05. The output intensity of the resonator was proportional to the square of the beam current. The observed intensities are well expressed by the line over a wide range of the beam current above 100 nA. The intensities observed below the current 100 nA were weak and near to the detecting limit.

4.3 Spectrum

Fixing the resonator at the maximum peak of the detuning curve at λ of 1.25 mm in Fig.2, we observed the output spectrum, using the mirror M3 (0.85). The result is shown by the solid curve in Fig.5. The spectrum is composed of continuous spectrum and a few peaks: the main peak at λ = 1.25 mm, and small peaks at λ = 2.5 and 0.64 mm.

The phase factor $\Delta\phi_{mn}$ is slowly varying function of frequency. The resonator condition of Eq. (8) therefore shows that the resonator condition is fulfilled not only at the wavelength of 1.25 mm, but with the wavelengths near to the higher harmonics 1.25 mm/J for integer J. The wavelength of 1.25 mm corresponds to the 84th harmonics of the RF of the accelerator; the harmonic number is even number.

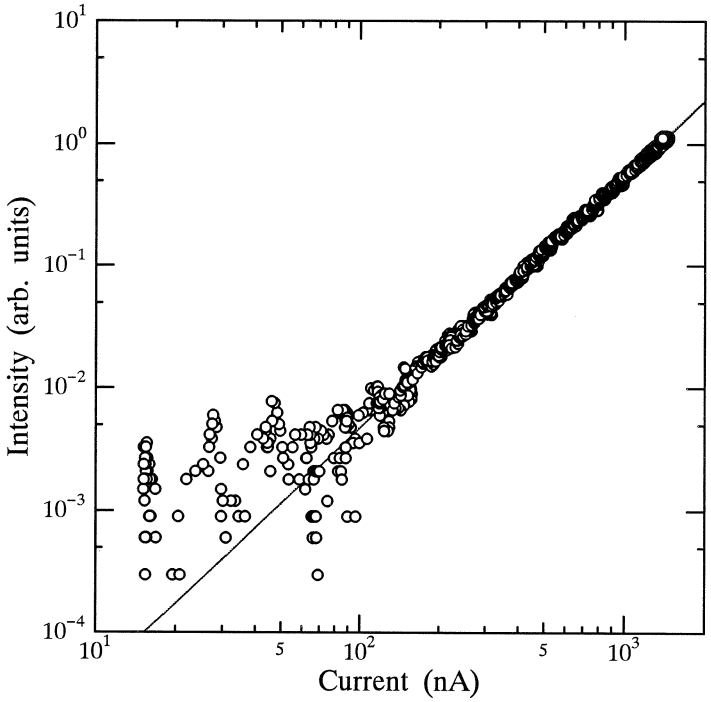

Fig.4. Dependence of the radiation intensity on beam current observed at $\lambda = 2.5$ mm with mirror M3 (0.85R).

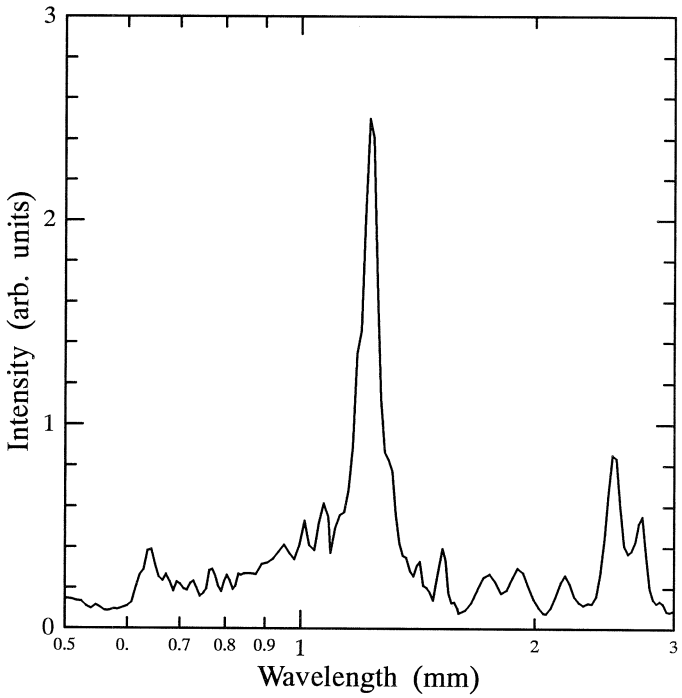

Fig.5. Output spectrum of the resonator with M3 (0.85R).

Hence the wavelength 2.5 mm also satisfies the resonator condition.

The spectral band width FWHM (full width at the half maximum), $2\Delta\lambda_{mn}$ of the peak of the mode (m, n) is written from Eq. (8), under the assumption that $\Delta\phi_{mn}/\lambda_{p,mn} \ll 1$, as

$$\cos(\Delta\varphi_{mn}\frac{\Delta\lambda_{mn}}{\lambda_{p,mn}}) = 1 - \frac{(1-r_{mn})^2}{2r_{mn}}, \tag{11}$$

where $\lambda_{p,mn}$ is the peak wavelength of the mode. The observed relative band width is $2\Delta\lambda_{01}/\lambda_{01} = 0.05$. The relative band width calculated with the reflectivity r_{01} of 0.837 is 0.11 and about twice of the experimental value. The reason of the discrepancy was not clear at present.

Replacing the mirror M3(0.85) by M3 (0.21), we also observed spectrum at the maximum peak of the wavelength of 1.25 mm in Fig.3. The results are shown by a solid curve in Fig.6. The spectrum is composed of continuous spectrum superposed with a few peaks: the main peak at $\lambda = 1.2$ and subpeaks at 1.1, and 0.89 mm. The broken curve shows theoretical distribution of the factor G (0, 1) of Eq. (8) fitted to the observed spectrum. In this case, the experimental bandwidth of the main peak is in agreement with the theory.

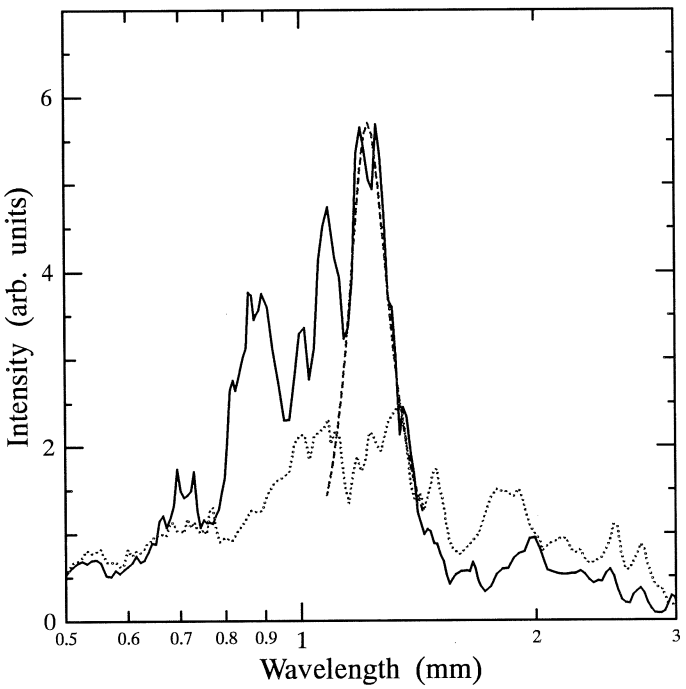

Fig.6. Observed spectra. The solid curve shows the output of the resonator with M3(0.21R) and the dotted one is the spectrum of TR. The broken one shows G (0, 1) fitted to the observation.

4.4 Amplification of radiation in resonator

To confirm the amplification of the coherent TR in the resonator, we compared the output of the resonator with the so-called spontaneous TR emitted within the resonator. To make the comparison, we measured the spectral intensity of the spontaneous coherent TR without the resonator, taking away the mirrors M1 and M3 from the setup in Fig.1. The observed intensity was superposition of the forward TR emitted from M2 and the backward TR from M4. The result is shown by the dotted curve in Fig.6.

In the experiment the energy of the electron was 150 MeV, and the formation zone of the TR is much longer than the distance between the mirrors M2 and M3 for the submillimeter and millimeter wavelength region. In such a case, the intensity of the superposition of the forward TR and the backward TR is proportional to the square of the emission length, i.e. the distance between the two mirrors [11]. The distance between the mirrors M2 and M4 was longer than that of M2 and M3. The

observed intensity shown by the dotted curve hence should be more intense than that of the coherent TR within the resonator.

Compared with the spectrum of the coherent TR, the output spectrum of the resonator with the mirror M3 (0.21) is amplified over a wide wavelength range from 0.8 mm to 1.3 mm. At the maximum peak, the intensity is amplified at least by a factor of 2.7. The result shows that we have observed stimulated emission of coherent TR.

Using the value of $r_{01} = 0.788$ determined from the detuning curve, however, the amplification factor, $(1+r_{01}) / (1-r_{01})$, was calculated to be 8.4 and was larger than the observed value. The reason for the difference is not clear at present.

In summary, using the mirror M3 (0.21R), we have confirmed that the output of the resonator was amplified, compared with TR generated within the resonator. In the prebunched FEL, the superposing process causes the amplification of the radiation due to stimulated emission.

We thank the staff of LNS, Tohoku University for their technical support and assistance during the experiment.

References

[1] for example, "*Free Electron Laser*" by C. A. Brau, Advance in Electronics and Electron Physics, Suppl. 22 (Academic Press, Boston 1990).

[2] H. Motz : J. Appl. Phys. **22** (1951) 527.

[3] F. Ciocci, R. Bartolini, A. Doria, G. P. Gallerano, E. Giovenale, M. F. Kimmitt, G. Messina, and A. Renieri : Phys. Rev. Lett. **70** (1993) 928.

[4] D. A. Jaroszynski, R. J. Bakker, A. F. G.van der Meer, D. Oepts, and P. W. van Amersfoort : Phys. Rev. Lett. **71** (1993) 3798.

[5] G. P. Gallerano, A. Doria, E. Giovenale, and G. Messina : Nucl. Instr. and Meth. **A358** (1995) 78.

[6] M. Asakawa, N. Sakamoto, N. Inoue, T. Yamamoto, K. Mima, S. Nakai, J. Chen, M. Fujita, K. Imasaki, C. Yamanaka, T. Agari, T. Asakuma, N. Ohigashi, and Y. Tsunawaki : Appl. Phys. Lett. **64** (1994) 1601.

[7] M. Cohen, A. Eichenbaum, H. Kleinman, D. Chairman, and A. Gover : Phys. Rev. **E54** (1996) 4178.

[8] J. S. Nodvick and D. S. Saxon : Phys. Rev. **96** (1954) 180.

[9] T. Nakazato, M. Oyamada, N. Niimura, S. Urasawa, O. Konno, A. Kagaya, R. Kato, T. Kamiyama, Y. Torizuka, T. Nanba, Y. Kondo, Y. Shibata, K. Ishi, T. Ohsaka, and M. Ikezawa : Phys. Rev. Lett. **63** (1989) 1245.

[10] K. Ishi, Y. Shibata, T. Takahashi, H. Mishiro, T. Ohsaka, M. Ikezawa, Y. Kondo, T. Nakazato, S. Urasawa, N. Niimura, R. Kato, Y. Shibasaki, and M. Oyamada : Phys. Rev. **43** (1991) 5597.

[11] Y. Shibata, K. Ishi, T. Takahashi, T. Kanai, F. Arai, S. Kimura, T. Ohsaka, M. Ikezawa, Y. Kondo, R. Kato, S. Urasawa, T. Nakazato, S. Niwano, M. Yoshioka, and M. Oyamada : Phys. Rev. **E 49** (1994) 785.

[12] Y. Shibata, K. Ishi, S. Ono, Y. Inoue, S. Sasaki, M. Ikezawa, T. Takahashi, T. Matsuyama, K.

Kobayashi, Y. Fujita, and E. G. Bessonov : Phys. Rev. Lett. **78** (1997) 2740.

[13] Y. Shibata, K. Ishi, S. Ono, Y. Inoue, S. Sasaki, M. Ikezawa, T. Takahashi, T. Matsuyama, K. Kobayashi, Y. Fujita, and E. G. Bessonov : Nucl. Instr. and Meth. **B282** (1998) 49.

[14] V. I. Alexeev, E. V. Alieva, K. A. Belovintsev, E. G. Bessonov, A. V. Serov, and P. A. Cherenkov : Nucl. Instr. and Meth. **A282** (1989) 436.

[15] A. Serov : Nucl. Instr. and Meth. **A308** (1991) 144.

[16] A. Serov : Nucl. Instr. and Meth. **A359** (1995) 70.

[17] Y. Shibata, T. Takahashi, K. Ishi, F. Arai, H. Mishiro, T. Ohsaka, M. Ikezawa, Y. Kondo, S. Urasawa, T. Nakazato, R. Kato, S. Niwano, and M. Oyamada : Phys. Rev. **A44** (1991) R3445.

[18] T. Takahashi, Y. Shibata, F. Arai, K. Ishi, T. Ohsaka, M. Ikezawa, Y. Kondo, T. Nakazato, S. Urasawa, R. Kato, S. Niwano, and M. Oyamada : Phys. Rev. **E48** (1993) 4674.

[19] G. Deardon, S. E. Mayhew, J. Lucas, and R. A. Stuart : Nucl. Instr. and Meth. **A375** (1996) 179.

[20] G.Deardon, S. E. Mayhew, J. Lucas, R. A.Stuart, J. R. Hartley, A. Shaw, and A. Al-Shamma'a : Nucl. Instr. and Meth. **A375** (1996) 183.

[21] A. Doria, R. Bartolini, J. Feinstein, G. P. Gallerano, and R. H. Pantell : IEEE J. Quant. Electr. **29** (1993) 1428.

[22] G. Dattoli, L. Giannessi, P. L. Ottaviani, and A. Torre : Phys. Rev. **E49** (1994) 5668.

[23] Y. Pinhasi and A. Gover : Nucl. Instr. and Meth. **A393** (1997) 343.

[24] S. Kuruma, K . Mima, M. Goto, and C. Yamanaka : Nucl. Instr. and Meth. **A407** (1998) 50.

[25] E. L. Saldin, E. A. Schneidmiller and M. V. Yurkov : Nucl. Instr. Meth. **A429** (1999) 41.

[26] V. A. Alexeev, E. G. Bessonov and A. V. Serov : Nucl. Instr. and Meth. **A282** (1989) 439.

[27] H. Lihn, P. Kung, C. Settakorn, H. Wiedemann, D. Bocek, and M. Hernandez : Phys. Rev. Lett. **76** (1996) 4163.

[28] Y. Shibata, S. Hasebe, K. Ishi, T. Takahashi, T. Ohsaka, M. Ikezawa, T. Nakazato, M. Oyamada, S. Urasawa, T. Yamakawa, and Y. Kondo : Phys. Rev. **E52** (1995) 6787.

Development of Hydrophones for Detecting High-Energy Reactions in Water

T. Matsuyama[1], S. Goto[6], N. Hasebe[2], M. Higuchi[3], F. Hinode[1], M. Ishiwata[4]
R. Kikuchi[5], O.Konno[7], T. Masumura[2], A. Misaki[2], T. Miyachi[2], I. Nakamura[4],
M. Oyamada[1] M. Sato[6], Y. Tazawa[5] and C. Tezuka[4]

[1]*Laboratory of Nuclear Science, Tohoku University, Mikamine, Taihaku, Sendai, 982-0826*
[2]*Advanced Institute for Science and Engineering, Waseda University, Shinjuku-ku, Tokyo, 169-8555*
[3]*Department of Applied Physics, Faculty of Engineering, Tohoku Gakuin University, Miyagi, 985-0873*
[4]*Department of Physics, Faculty of Science, Saitama University, Saitama, 338-8570*
[5]*Graduate School of Science, Kyoto University, Kyoto, 606-8502*
[6]*Honda-Electronics Co., LTD, Aichi, 441-3193*
[7]*Ichinoseki National College of Technology, Iwate, 021-8511*

Acoustic detectors were developed using a piezo ceramic compound PZT. A shape of the PZT detector was essential to obtain a high sensitivity. A detector of a spherically shaped shell structure, whose size was 50 mm in diameter and 2 mm thick, was fabricated. Its sensitivity was calibrated to be about 40 mV/Pa at 54 kHz. Using the hydrophone, acoustic signals generated by an electron-induced cascade shower in water were detected. Experimental results were compared with simulation data and confirmed a consistency in between.

§ 1. Introduction

As proposed by Sulak *et al.*[1], a sonic signal produced by charged particles while traversing or stopping in a medium has a potential to realize beam monitors, heavy ion detectors, calorimeters and cosmic neutrino/muon detectors. In addition to the above scope, use of an acoustic signal is promising to realize a real-time detector to macroscopic tiny particles, e.g., the space dust. In spite of its bright prospects, we have been available few works on such radiation detectors. Thus it has been motivated in developing the hydrophone for the acoustic signal produced by the high energy radiation and dust. This report concerns an experimental study on the acoustic radiation detector using the hydraulic pressure caused by an electron induced cascade shower in water.

§ 2. Hydrophones

In this report, we deal with the case of PZT ceramic detectors with a spherically shaped shell. It was pointed out in the previous papers[2-6] that the shape of the PZT detector was essential from a point of view of achieving a high sensitivity. We have developed the hydrophone made from low-Q PZT material. In order to discuss an effect of detector shape, we made two types of them; one was the disk-shaped (DS) and the other was the spherical shaped (SS) as shown in Fig.1. The former was 2 mm thick and 20 mm in diameter, and the later 2 mm thick and 50 mm in diameter.

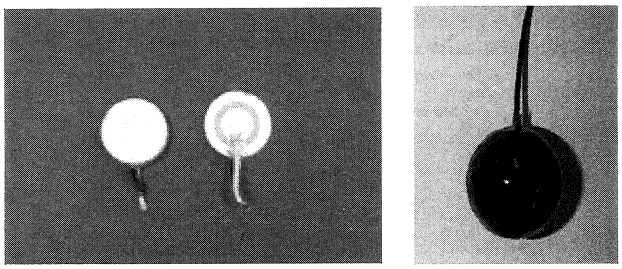

Fig.1. Detector forms. Disk-shaped (DS:left) and spherical shaped (SS:right).

Each was calibrated by using a standard element. At present, however, it is difficult to determine an absolute sensitivity precisely. The characteristic of DS and SS is as follows. The resonance peak of the DS is approx.100 kHz, and DS is approx. 50 kHz. A sensitivity for the DS and SS is from 1mV/Pa to 10mV/Pa.The frequency characteristics was used in a stage of data analysis.

§ 3. Experiment

3.1. Experimental Methods

Generation and propagation of a sound signal in water have been studied extensively[7]. By assuming uniform heating within a cylinder of a diameter d and length L, a signal pressure amplitude P and a signal frequency f are given by the following expressions:

$$P = \frac{k}{C_p} \frac{E}{\sqrt{Lr}} \frac{c^2}{8d^2} \frac{\sin x}{x}, \tag{1}$$

$$f = \frac{v}{2d}, \tag{2}$$

$$x = \left(\frac{\pi L}{\lambda}\right) \sin\theta \tag{3}$$

where v is the sound velocity, E the total energy deposit, k the volume coefficient of expansion of water, C_p the heat capacity of water, λ the wavelength, θ the direction of radiation with respect to the normal of the heat cylinder, and r is a distance between a volume element and the point at which the pressure is observed. The detectors were placed in the tank filled with water.

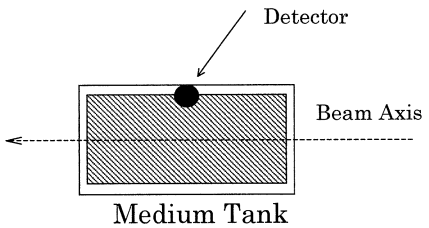

Fig.2. Experimental arrangement placed in the beam line.

An experimental arrangement is shown in Fig.2. A water tank was placed in a beam line of the 300 MeV electron linac at Tohoku University. The size of tank is H200mm×W200mm×L300mm, and it was

filled with water. The water tank can be controlled in the range from 0 ℃ to 50 ℃. Some detectors were attached at a folder of the tank and one detector was mounted on a translator moving in a two-dimensional way, back-and-forth, and up-and-down. The present data were taken in the energy range from 150 to 230 MeV.

The beam intensity was measured by a non-destructive current integrator [8]. The beam was passed through a ferrite core, then an induced current was picked up with a coil. The output amplitude was calibrated to be linear over 0.1 to 100 nC.

A beam diameter was estimated by observing a beam profile on a MgO_2 screen. Fluorescence light intensity was viewed by a camera, then analyzed by least squares fits to a Gaussian form within 10% accuracy.

The acoustic signal was measured by a digital oscilloscope and numerical data were transferred to a personal computer (PC). Readings for beam intensity, beam profile and water temperature were stored into the PC.

3.2 Detector Characteristics

The pressure signal as shown in Fig.3 was reduced to the pressure amplitude by applying

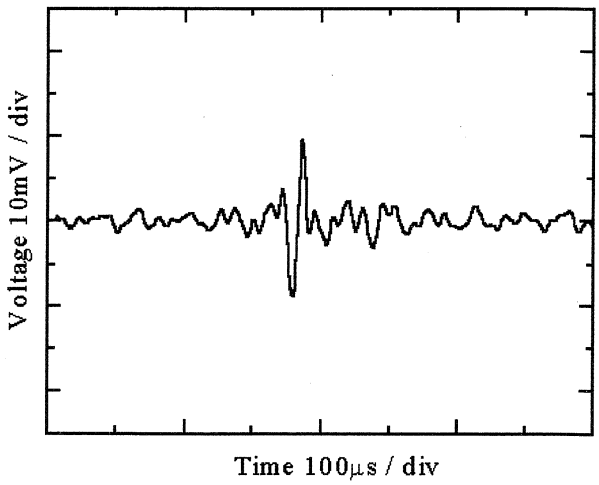

Fig.3. Bipolar signal obtained after corrections.
(Beam Parameters; energy 200 MeV, 10^9 electrons, spill time approx. 1.5 μs Detector: SS)

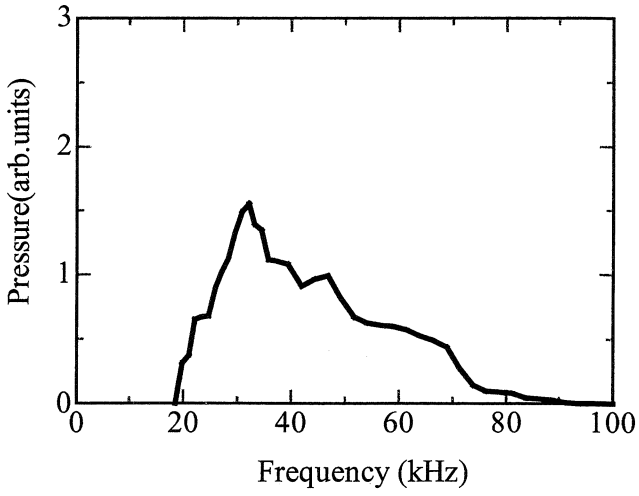

Fig.4. Frequency distribution of the signal.

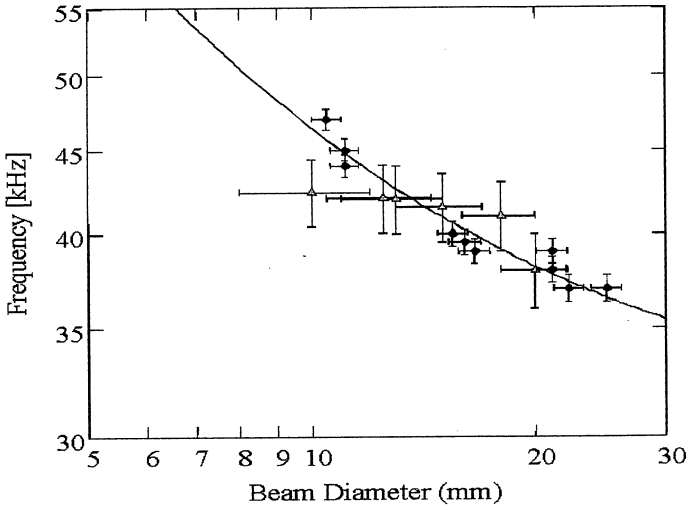

Fig.5. Beam diameter vs. acoustic frequency.
(Beam Parameters; energy 200 MeV, 10^9 electrons, spill time approx. 1.0 μs Detector: SS)

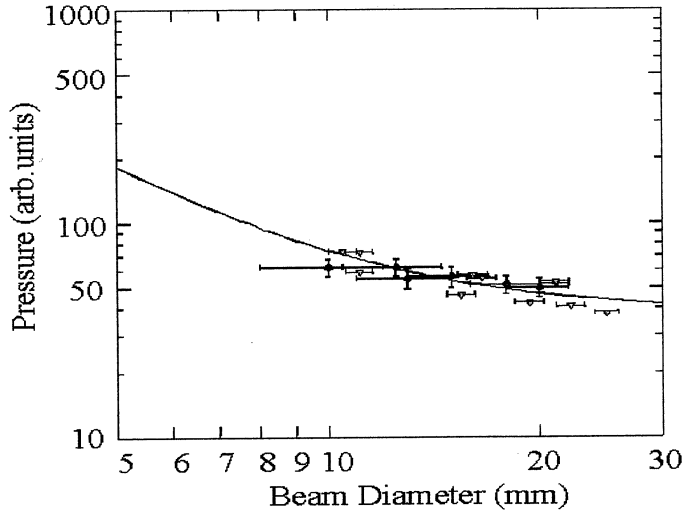

Fig.6. Beam diameter vs. signal amplitude.
(Beam Parameters; energy 200 MeV, 10^9 electrons, spill time approx. 1.0 μs Detector: SS)

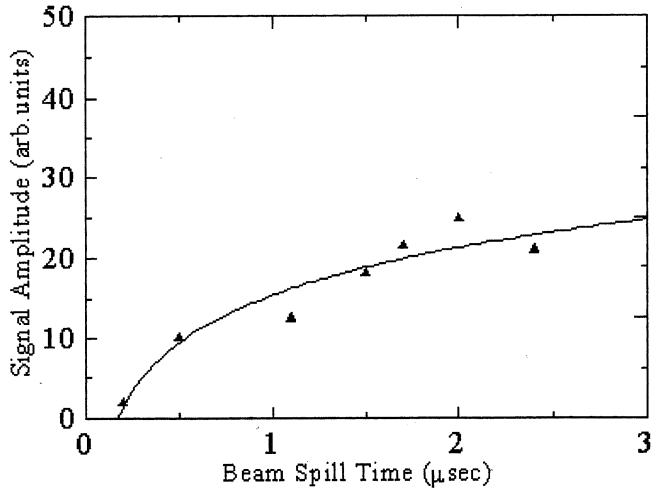

Fig.7. Dependence of signal amplitude on beam spill time.
(Beam Parameters; energy 200 MeV, 10^9 electrons, Detector: SS)

corrections for the frequency response characteristics and frequency cuts. In Figs.3 and 4, the pressure signal and frequency spectrum are shown, respectively. From Fig.3, it is shown that the pressure signal is bipolar in time. In the following, the signal amplitude is regarded as a peak-to-peak of the bipolar signal.

The frequency response shows a broad distribution located less than 100 kHz and a maximum at ~ 35 kHz. The frequency of the acoustic signal is as the maximum point of the frequency spectrum.

3.3 Experimental Results

(1) Beam diameter dependence

The beam diameter d is related to two quantities; pressure P and frequency f. The observed diameter d_B is not always equal to d. We regard d_B as d. In Figs.5 and 6, f vs. d^{-1} and P vs. d^{-2} are plotted respectively. Solid curves are drawn based on the respective functional dependences. From the both figures, the beam size effect is consistent with eq. (1).

(2) Spill time dependence

The signal amplitude is also dependent of a beam spill time as shown in Fig.7. This behavior suggests a possible existence of a saturation effect. It is still open to understand this quantitatively.

(3) Temperature Dependence

Since a pressure of acoustic signal was sensitive to temperature of water[1], we measured a correlation between the pressure and temperature. One of results measured in pure water is shown in Fig.4. We confirmed a significant change of the pressure at the detector position. This behavior is consistent with those by Sulak *et al.*[1], within the experimental error. Besides pure water, the pressure dependence on temperature was done using natural seawater. We have obtained substantially same as in pure water.

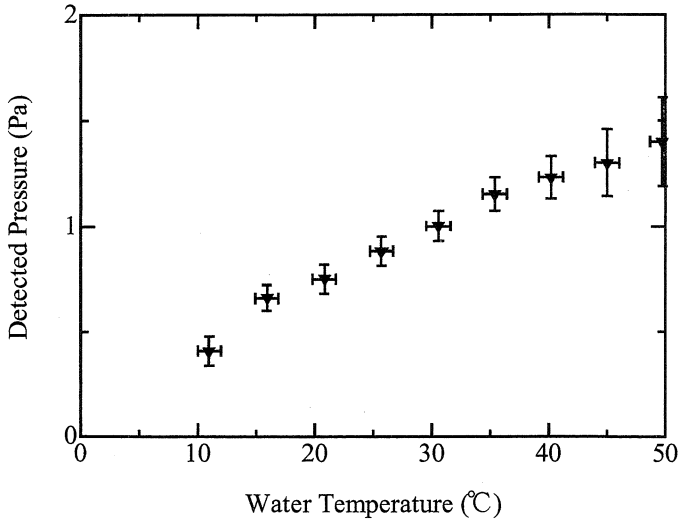

Fig.8. Temperature Dependence found in pure water.
(Beam Parameters; energy 150 MeV, 10^9 electrons, spill time approx. 1.0 μs Detector: SS)

Besides pure water, temperature dependence was measured using natural seawater. A similar temperature dependence as pure water was obtained.

(4) Direct irradiation response

The response wave form for a direct beam irradiation to the detector (DD) is shown in Fig.9.

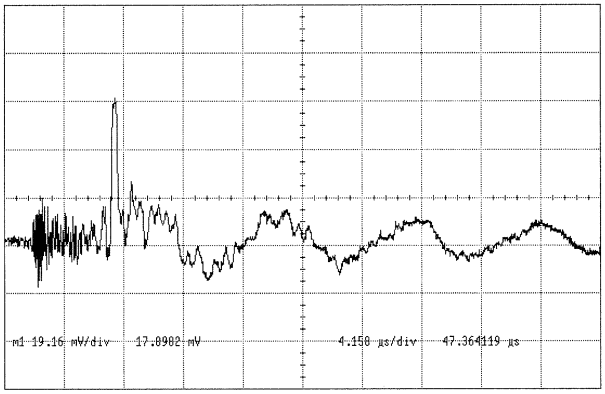

Fig.9. Direct irradiation response wave form.
(Beam Parameters; energy 200 MeV, 10^9 electrons, spill time approx. 1.5 μs Detector: DS)

§ 4. Conclusion

The acoustic detectors, which are made from spherically shaped PZT ceramic, are studied. The sensitivity is around 40 mV/Pa at 54 kHz. Using the detectors, the acoustic signal produced by the cascade shower in water was measured.

It is confirmed that pressure amplitude is dipole in time. The amplitude is proportional to the total deposit energy. The amplitude and the frequency depend on the beam size. There exists a possible effect due to spill time. The beam diameter affects the pressure amplitude. The irradiation response signal was confirmed on the experiment energy. The correction about the temperature dependence is difficult by a characteristic of PZT, and it is being analyzed at present.

It is required further investigations for not only improving detectors but also calibration method.

References

[1] L. Sulak *et al.* : Nucl. Instr. and Meth. **161** (1979) 203.

[2] L. G. Dedenko *et al.* : Izv. RAN(ser.fiz.) **58** (1994) 146.

[3] G. A. Askariyan and B. A. Dolgoshein : Preprint. No.160, Lebedev Physical Institute of the USSR Academy of Sciences, MOSCOW (1976).

[4] J. Learned : Phys. Rev. **D19** (1979) 3293.

[5] T. Bowen : "DUMAND 76",. *Proc. 15th Int. Cosmic Ray Conf., Sophia, Bulgaria* (1977). p.523.

[6] T. Matsuyama *et al.* : Research Report of Nuclear Science, Tohoku Univ. **32** (1999) 94.

[7] T. Miyachi *et al.* : *Prc. PACON 99* (Moscow,June1999) 543.

[8] T. Nakazato : private communication.

[9] T. Miyachi *et al.* : *Prc. IEEE NSS 2000.*

Ⅳ. 2000 Status Report on the Accelerator

Status Report of LNS Accelerator Complex in 2000

H. Hama, F. Hinode, A. Kurihara, M. Mutoh, M. Nanao, M. Oyamada,
Y. Shibasaki, K. Shinto and S. Takahashi

Laboratory of Nuclear Science, Tohoku University, 1-2-1 Mikamine, Taihaku-ku, Sendai 982-0826

The accelerator complex at the Laboratory of Nuclear Science, Tohoku University consists of a 300 MeV electron linac that has been operational for 34 years and a stretcher-booster synchrotron (STB ring) constructed for multipurpose use whose operation was started in 1997. In this report, major tasks of those accelerators are introduced, and operation experiences in the fiscal year 2000 are presented. In addition, improvement and replacement of devices are described.

§ 1. Accelerator complex

The S-band linac is composed of 20 accelerating structures which are driven by five klystrons, and has been presently operated for three different major purposes such as radioisotope production for nuclear chemistry, fundamental studies of coherent synchrotron radiation and being used as an injector of the STB ring. For radioisotope production, an intense long-pulse beam accelerated in the low energy section (below 60 MeV) is provided with a high repetition rate of 300 Hz. A 150 MeV pulsed beam with lower repetition rates is normally used for the coherent radiation experiment.

The STB ring has become to be routinely operated as a booster (up to 1.2 GeV) for nuclear experiments in which an internal target wire is used as a radiator of bremsstrahlung gamma rays. Another function of the STB ring is a pulse-beam stretcher to provide quasi cw-beam for nuclear experiments employing the 3rd order resonance slow extraction. In the booster mode operation, a linac beam energy of 200 MeV is normally employed for the injection. The beam burst is triggered so as to synchronize with the sequence of the energy ramping, which is governed by a programmable timing controller. Although the beam storage time at the top energy can be arbitrarily extended, the ramping speed is restricted to be 1 GeV / 1.1 s by performance of the power supplies. Meanwhile the injector linac is operated at the 300 Hz repetition rate for the stretcher mode to earn the highest duty factor. Typical energy range of the stretcher mode is from 150 MeV to 200 MeV. Stable operation of the stretcher mode has not been established yet because of complicate beam dynamics in a resonance extraction without rf beam capture, accordingly both experimental and theoretical machine studies are under way.

§ 2. Troubles

As a result of which many old devices in the linac have been deteriorated, we have experienced a lot of troubles and difficulties. For instance mechanical troubles happened on phase shifters, transverse apertures, and slits in energy-analyzer sections, and electric failures happened on a power supply for

klystron focusing coils and on a diode array in a DC power supply for a klystron modulator. Furthermore many high voltage cables for ion pumps of the linac were damaged by the radiation and had to be replaced. Those troubles were mostly fixed during maintenance terms between scheduled machine times for users.

In addition to those fated troubles, a klystron that was a relatively younger one was in malfunction during an injector operation for the booster mode of the STB ring in the end of '00. Since there was no spare one at that time, we decided to reduce the injection energy down to 150 MeV from 200 MeV so as to be driven by remaining four klystrons. The trouble was due to cut off of a heater circuit in the klystron, which seemed to be an unusual trouble. Fortunately we had previously ordered a new one and it was delivered just after the booster machine time (February, '01).

On the other hand, there were various troubles on the STB ring. Because of insufficient machine study so far, devices of the ring had suffered serious radiation damage due to beam losses at the injection and the storage. Particularly controllers for the ion pumps and the pump itself were frequently broken. One of the ion pumps was replaced with one manufactured by another company, which is expected to be tough against radiation. Radiation damage had spread over many devices. However as the machine study was getting progressed, those trouble have become to scarcely occurred.

An unexpected trouble was found out in a vacuum chamber of a bending section in the ring. The chamber modified to install a tagging detector array for production of the bremsstrahlung gamma ray was mounted in '99. Since we noticed that the beam was not able to circulate on the central orbit in the dispersive sections of the ring, we have investigated spatial region of the orbit where the beam can circulate by making bump orbits in the dispersive sections using respective additional windings of dipole magnets. As a consequence, we were convinced of which an obstacle might be in a vacuum chamber. Finally it was discovered that a stay to support the chamber was put on just the central orbit by mistake. This incredible happening was fixed during a summer shut-off term.

§ 3. Improvements

That was a great news that a budget for replacing a old water cooling tower for the linac was approved. The cooling tower was working for more than 30 years, and it already became to be deteriorated and was very hard to be maintained. During a long shut-off term specially scheduled in the summer, the tower was replaced with a new one which has a cooling capacity of 400 tons (old one is 320 tons) equips various functions such as a guard system for water electric conductivity and automatic heater system to protect water freeze. At the same time to install the new cooling tower, main round-trip header pipes were cleaned up and old plumbing for the klystron modulators were replaced.

Another important project to replace old systems was started. That is construction of new control system for the linac using a network management system COACK (Component ware Oriented Accelerator Control Kernel) for Windows machines developed at KEK. Because of recent great progress of computer technology, there would be many software and hardware tools based on personal computers, which allows us to control devices easily with small budget. To use those resources efficiently, and taking extensibility into account, an architecture consists of COACK and personal

computers was chosen. Because many devices have been controlled by peculiar interfaces and communication protocols, it had been difficult to maintain. At the moment the new system connects with those old controllers, so that the project will be extended to replace with standard ones such as PLC.

On the STB ring operation, the betatron tune measurement has been progressed by installing a strip-line type electrodes. The strip-line excites the betatron oscillation by applying an external rf dipole field, and the beam signals is analyzed in the frequency domain by a real time spectrum analyzer. We have observed tune shifts during the energy ramping, which will be valuable for further improvement of the ramping sequence. Furthermore the tune just after the beam injection was also observed. It is a very important information for understanding of the beam dynamics at the injection and for fine tuning of the stretcher operated near the 3rd order resonance.

Acknowledgment

Professor M. Oyamada was retired in March, '01. He had been working at LNS as a leader of the accelerator group since the facility was founded. We greatly appreciate him and hope him to get a new success in his coming job at Siam photon source, Thailand.

V. List of Publication

List of Publication（論文リスト）（2000.1～2000.12）

Papers Published in Refereed Journals

1. Observation of S_{11} Resonance in Nuclear Medium via the $^{12}C(\gamma, \eta)$ Reaction.
   T. Yorita, H. Yamazaki, T. Kinoshita, T. Okuda, H. Matsui, J. Kasagi, T. Suda, K. Itoh, T. Miyakawa, H. Okuno, H. Shimizu, H.Y. Yoshida, T. Kinashi and T. Maruyama
   Phys. Lett. **B476** (2000) 226-232.
2. Study of S_{11} Resonance in Nuclei through (γ, η) Reactions.
   H. Yamazaki, T. Yorita, T. Kinoshita, T. Okuda, H. Matsui, T. Maruyama, J. Kasagi, T. Suda, K. Itoh, T. Miyakawa, H. Okuno, H. Shimizu, H.Y. Yoshida and T. Kinashi Nucl. Phys. **A670** (2000) 202c-205c.
3. Probing the ΔNN Component of ^{3}He.
   G. M. Huber, G. J. Lolos, E. J. Brash, S. Dumalski, F. Farzanpay, M. Iurescu, Z. Papandreou, A. Shinozaki, A. Weinerman, T. Emura, H. Hirosawa, K. Niwa, H. Yamashita, K. Maeda, T. Terasawa, H. Yamazaki, S. Endo, K. Miyamoto, Y. Sumi, G. Garino, K. Maruyama, A. Leone, R. Perrino, T. Maki, A. Sasaki and Y. Wada (The TAGX Collaboration).
   Phys. Rev. **C62** (2000) 044001(1)-044001(8).
4. G_{Ep}/G_{Mp} Ratio by Polarization Transfer in ep → ep.
   M.K. Jones, K.A. Aniol, F.T. Baker, J. Berthot, T. Saito *et al.*
   Phys. Rev. Lett. **84** (2000) 1398-1402.
5. Dynamical Relativistic Effects Observed in Quasielastic 1p-Shell Proton Knockout from ^{16}O.
   J .Gao, B. D. Anderson, T. Terasawa *et al.*
   Phys. Rev. Lett. **84** (2000) 3265-3269.
6. Reply to Comment on Bremsstrahlung in α Decay of ^{210}Po.
   J. Kasagi, H. Yamazaki, N. Kasajima, T. Ohtsuki and H. Yuki
   Phys. Rev. Lett. **85** (2000) 3061.
7. Systematic Study of Foreign-atom-doped Fullerenes by Using Nuclear Recoil Method and Their MD Simulation.
   T. Ohtsuki, K. Ohno, K. Shiga, Y. Kawazoe, Y. Maruyama, K. Masutomo
   J. Chemical Physics. **112** (2000) 2834-2842.
8. Activation Analysis of Several Species of Marine Invertebrates as Indicators of Environmental Conditions.
   M.Fukushima, H. Tamate, Y. Nakano
   J. Radioanal. Nucl. Chem., **244** (2000) 55-59.
9. How Effectively is the Photon Activation Analysis Applied to Meteorite Samples?
   M.Ebihara, Y.Oura, T.Ishii, M.Setoguchi, H.Nakahara and T.Ohtsuki
   J.Radioanal.Nucl.Chem. **244** (2000) 491-496.

10. Temporal Stability of the UVSOR-FEL Micropulse.
    M. Hosaka, S. Koda, J. Yamazaki and H. Hama
    Nucl. Instr. and Meth. **A445** (2000) 208-213.
11. A New Scheme of Direct Beam Chopping in a Negative Hydrogen Ion Source.
    K. Shinto, A. Takagi, K. Ikegami and Y. Mori
    Rev. Sci. Instrum. **71** (2000) 696-697.
12. Energy Analysis of Negative Hydrogen Ions using Detached Electrons.
    M. Takahashi, M. Yoshimoto, K. Shinto, A. Takagi, K. Ikegami and Y. Mori
    Rev. Sci. Instrum. **71** (2000) 1101-1103.

Papers Published in International Conference Proceedings

1. Nuclear Physics Experiments with 1.2-GeV STB Ring at LNS-Tohoku.
    J. Kasagi
    Proceedings of the 2nd KEK-Tanashi International Symposium on Hadron and Nuclear Physics with Electromagnetic Probes, ed. K. Mauyama and H. Okuno (Elsevier Science B. V., 2000) p. 265 - 269.
2. S_{11}(1535) Resonance in Nuclei.
    H. Yamazaki, T. Yorita, T. Kinoshita, T. Okuda, H. Matsui, T. Maruyama, J. Kasagi, T. Suda, K. Itoh, T. Miyakawa, H. Okuno, H. Shimizu, H.Y. Yoshida and T. Kinashi
    Proceedings of the 2nd KEK-Tanashi International Symposium on Hadron and Nuclear Physics with Electromagnetic Probes, ed. K. Mauyama and H. Okuno (Elsevier Science B. V., 2000), p 61 - 66.
3. Photon Activation Analysis of Trace Elements in Livers, Kidneys, and Spleens of Pig Fetuses.
    M.Fukushima, K.Kajiwara, M. Oizumi
    Isotope Production and Applications in the 21th Centry, Proceedings of the 3rd International Conference on Isotopes (2000) 117-120.
4. Current Status of a 1.2 GeV Booster Electron Synchrotron and Implementation for Nuclear Study at Tohoku University.
    H. Hama, F. Hinode, O. Konno, A. Hurihara, A. Miyamoto, M. Mutoh, M. Nanao, M. Oyamada, Y. Shibasaki, K. Shinto, S. Takahashi
    Proc. 18th International Conf. On High Energy Accelerators (HEACC2001), (2001).

Review

1. Low Energy Nuclear Reactions in Solids.
    J. Kasagi
    原子核研究、**45** (2000) 15 -24.
2. The Study of Endohedral Fullerenes and Heterofullerenes by Nuclear Recoil and MD Simulation.
    T.Ohtsuki, K. Ohno
    Book: Nuclear and Radiochemical Approaches to Fullerene Sciences, Edited by T. Braun,

Kluwer Academic Publisher (2000) 136-157.

3. Fullerenes Radiolabelled on the Carbon Cage.

K. Masutomo T.Ohtsuki, K. Shikano

Book: Nuclear and Radiochemical Approaches to Fullerene Sciences, Edited by T. Braun, Kluwer Academic Publisher (2000) 158-173.

VI. Approved Experiments

平成12年度前期採択課題一覧表

課題番号	課題名	申込責任者	採択シフト数
原子核関連分野			
2371	原子核内 $S_{11}(1535)$ 状態の研究	笠木治郎太	28
2372	(e,e′x) 反応による ^{9}Be の共鳴状態の研究	玉江　忠明	6
2373	^{24}Mg (e,e′ α)^{20}Ne 反応の研究	坪田　博明	8
2374	閾値エネルギー以下での π^0 生成機構の探索のテスト実験	広田　克也	4
2375	Quasi-Free Photoproduction of Neutral Kaons on ^{12}C near Threshold Region	橋本　治	24
放射光関連分野			
2376	コヒーレント回折放射を用いたバンチ計測の研究（3）	小山田正幸	6
2377	コヒーレント放射によるオンラインバンチ計測の研究	柴田　行男	8
2378	マイクロバンチ FEL の基礎研究	伊師　君弘	6
加速器・測定器関連分野			
2379	粒子音響検出器の開発研究（2）	樋口　正人	3
放射化学・物性関連分野			
2380	ファイバアンプ用ガラス中の炭素の光量子放射化分析	鹿野　弘二	1
2381	軽元素の光量子放射化分析のための迅速化学分離法の開発	桝本　和義	2
2382	マグネシウムおよび SiC における拡散	藤川辰一郎	1
2383	ネプツニウム精製システム開発を目的としたイオン交換クロマトグラフィーの過負荷状態の解析	山村　朝雄	2
2384	Th-229m の製造とその崩壊特性	三頭　聰明	1
2385	沈澱法にもとづく核分裂生成物およびアクチニド元素の系統的分離法の研究	原田　雅幸	1
2386	バイオポリマーを用いた抽出剤のマイクロカプセル化と核種分離	秋葉　健一	1
2387	光量子放射化分析法による隕石試料中のハロゲン元素の定量	海老原　充	2
2388	標識化による金属内包フラーレン及びヘテロフラーレンの研究（継続）	大槻　勤	3
2389	^{230}Th (γ,n) 反応で生成する $^{229m,229}Th$ の反跳捕集	中西　孝	1
2390	長寿命放射性核種の環境中移行における基礎化学反応研究	関根　勉	2

平成12年度後期採択課題一覧表

課題番号	課題名	申込責任者	採択シフト数
原子核関連分野			
2391	SPring 8-GDH 実験用ガンマ線検出器の性能評価	岩田　高広	2
2392	BL-V Tagger 整備およびγ線ビームプロファイルモニター開発	前田　和茂	4
2393	(γ,xn)　反応による中性子多重度測定法のテスト	原田　秀郎	4
2394	焦点面 SSD の放射線損傷耐性テスト	高橋　俊行	6
2396	(e,e′n) 反応による^{28}Si 核のアイソベクトル型単極子, 四重極子巨大共鳴の研究Ⅱ	木野　幸一	19
2397	原子核内 S_{11}(1535) 状態の研究	笠木治郎太	20
放射光関連分野			
2398	マイクロバンチ FEL の基礎研究	柴田　行男	8
加速器・測定器関連分野			
2400	粒子音響検出器の開発研究（2）	樋口　正人	6
2401	電子ビームを用いた X 線増感紙の較正	小林　　正	1
放射化学・物性関連分野			
2402	マグネシウムにおける拡散	藤川辰一郎	1
2403	長寿命放射性核種の環境中移行における基礎化学反応研究	関根　　勉	3
2404	フライアッシュのゼオライト化および核種の分離固定	秋葉　健一	1
2405	ファイバアンプ用ガラス中の炭素の光量子放射化分析	鹿野　弘二	1
2406	Th-229m の製造とその崩壊特性	三頭　聰明	1
2407	Cs トレーサーの製造精製法の開発	山村　朝雄	1
2408	^{230}Th (γ,n) 反応で生成する ^{229m}Th の反跳捕集と ^{146}Sm の製造	中西　　孝	1
2409	標識化による金属内包フラーレン及びヘテロフラーレンの研究及びその応用	大槻　　勤	3
2411	海洋環境における動植物の多元素同時放射化分析	福島美智子	1
2412	光量子放射化分析法による隕石試料中のハロゲン元素の定量	海老原　充	2

核理研研究報告　第34巻

2001年11月発行

発行所　東北大学大学院理学研究科
附属原子核理学研究施設
仙台市太白区三神峯1-2-1（郵便番号982－0826）
電話　022－743－3400

印刷所　株式会社　東北プリント
仙台市青葉区立町24番24号
TEL　022（263）1166㈹

RESEARCH REPORT OF
LABORATORY OF NUCLEAR SCIENCE
TOHOKU UNIVERSITY

Volume 34 November 2001

Laboratory of Nuclear Science, Tohoku University,
1-2-1, Mikamine, Taihaku, Sendai 982-0826, Japan

東北大学大学院理学研究科

原子核理学研究施設